ACCSCIENCE PUBLISHING

International Journal of Bioprinting

ACCEPTED PAPER · MAIN TEXT

Intelligent process control and stimulus-responsive 4D transformation in extrusion-based 3D food printing: A critical review

Paper version: Accepted Paper

Accepted Papers are manuscripts accepted for publication, encompassing all changes made following the peer review process, along with a standard cover page indicating the paper version and an "Accepted Paper" watermark, but excluding any other editing, typesetting or other changes made by AccScience Publishing and/or authors post-acceptance.

Article ID: IJB026200182

Citation: Jeon S, Go A, Kim D, Moon SK, Park SJ. Intelligent process control and stimulus-responsive 4D transformation in extrusion-based 3D food printing: A critical review. *Int J Bioprint*. 2026. doi: 10.36922/IJB026200182

Copyright: © 2026 Author(s). This is an Open Access article distributed under the terms of the Creative Commons Attribution License, permitting distribution, and reproduction in any medium, provided the original work is properly cited.

Publisher's Note: AccScience Publishing remains neutral with regard to jurisdictional claims in published maps and institutional affiliations.

AccScience Publishing
REVIEW ARTICLE
Volume X Issue X (2026)
doi: 10.36922/IJB026200182

Intelligent process control and stimulus-responsive 4D transformation in extrusion-based 3 D food printing: A critical review

Running title: Intelligent control and 4D food printing

Sangjun Jeon[1†], Ara Go[2†], Donghui Kim[1,3], Seung Ki Moon[1,3]*, and Seong Je Park[4]*

[1] School of Mechanical and Aerospace Engineering, Nanyang Technological University, Singapore, 639798, Singapore
[2] Department of Future Convergence Engineering, Kongju National University, Cheonan, 31080, Republic of Korea
[3] Singapore Centre for 3D Printing, School of Mechanical and Aerospace Engineering, Nanyang Technological University, Singapore, 639798, Singapore
[4] School of Mechanical Engineering, Gyeongsang National University, 501 Jinju-daero, Jinju-si, 52828, Gyeongsangnam-do, Republic of Korea

(This article belongs to the *Special Issue: 3D Food Printing: Materials, Processes and Applications*)

[†]*These authors contributed equally to this work.*

*** Corresponding authors:**
Seung Ki Moon (skmoon@ntu.edu.sg)
Seong Je Park (seongje.park@gnu.ac.kr)

Citation: Jeon S, Go A, Kim D, Moon SK, Park SJ. Intelligent process control and stimulus-responsive 4D transformation in extrusion-based 3D food printing: A critical review. *Int J Bioprint.* 2026. doi: 10.36922/IJB026200182

Received: May 12, 2026
Revised: June 9, 2026
Accepted: June 16, 2026
Published online: June 16, 2026

ACCEPTED PAPER

Copyright: © 2026 Author(s). This is an Open-Access article distributed under the terms of the Creative Commons Attribution License, permitting distribution, and reproduction in any medium, provided the original work is properly cited.

Publisher's Note: AccScience Publishing remains neutral with regard to jurisdictional claims in published maps and institutional affiliations.

ACCEPTED PAPER

Abstract

Three-dimensional food printing (3DFP) presents unparalleled opportunities for personalised nutrition, clinical dysphagia management, decentralised on-demand production, and space-mission food provision. However, industrial translation remains constrained by inconsistent rheological characterisation, limited cross-material generalisation of process-control models, and the absence of integrated quality-control frameworks for post-processed and stimulus-responsive constructs. Although extrusion-based 3DFP offers the broadest substrate compatibility among additive manufacturing routes, prior reviews have treated ink formulation, process control, post-processing, and 4D transformation as separate domains. In this work, extrusion-based 3DFP is reviewed in an integrated manner. Rheological foundations and substrate-specific ink design are examined across hydrocolloid, protein, starch, fruit/vegetable, dairy, meat, and bioactive-loaded systems. Intelligent process control is then discussed through three integrated axes: computational fluid dynamics modelling, data-driven low-field NMR with machine-learning prediction, and real-time computer-vision feedback. Pre- and post-processing engineering is examined alongside an integrated quality-control framework, and recent stimulus-responsive 4D studies are organised by trigger and response. Synergistic integration of these domains demonstrates clinical and personalised-nutrition potential beyond that of any single-domain approach. This article systematically reviews the ink design, intelligent process control, post-processing engineering, and stimulus-responsive 4D transformation of extrusion-based 3DFP, aiming to provide valuable insights for the development of intelligent food-printing systems.

Keywords: 3D food printing; Material extrusion; Intelligent process control; 4D stimulus-responsive transformation; Machine learning

ACCEPTED PAPER

1. Introduction

1.1 Background

Global food systems are under mounting pressure from climate-driven supply variability, demographic shifts toward an aging population, and the rising demand for clinically tailored nutrition. In this context, additive manufacturing has emerged as a candidate technology for decentralised, customisable food production [1]. As defined by the International Organization for Standardization and American Society for Testing and Materials (ISO/ASTM 52900) [2], additive manufacturing comprises seven standardised process categories — material extrusion (MEX), powder bed fusion (PBF), binder jetting (BJ), material jetting (MJT), vat photopolymerization (VPP), sheet lamination, and directed energy deposition — distinguished by the physical principle through which the build material is consolidated. Within food applications, four of these categories have been reported in the peer-reviewed literature [3–6], while VPP, sheet lamination, and directed energy deposition are not yet practical for food applications owing to material-safety, regulatory, and substrate-compatibility considerations. Over the past decade, three-dimensional food printing (3DFP) has matured well beyond its origins: once confined to confectionery prototyping, it now enables the direct fabrication of structurally engineered, nutritionally tailored food products [3,7,8]. It has since drawn sustained interest across clinical nutrition — for dysphagia and elderly-care diet engineering — as well as personalised macro- and micronutrient delivery, decentralised on-demand production, and longer-horizon space-mission and military food provisioning [9–12].

The design freedoms of 3DFP arise directly from its additive, layer-by-layer construction, which conventional moulding, extrusion, and casting cannot reproduce simultaneously. Geometric customisation permits the construction of intricate visual and sensory geometries — lattice-textured snacks, internally compartmentalized confectionery, organ- or character-shaped meat analogues — that no mould, extruder, or casting line can produce [3,7,8,13]. On-demand nutritional personalisation allows the macro- and micronutrient composition of the deposited construct to be tailored to individual dietary requirements at the design stage rather than at the formulation stage [11,12,14]. Multi-material co-deposition through coaxial and multi-nozzle configurations encodes functional gradients — flavour encapsulation, bioactive compartmentalisation, texture stratification, and ingredient layering — within a single printed object [13–15]. Stimulus-responsive 4D programming, achieved by spatially distributing components of with differing physicochemical responsiveness within the deposited matrix, allows the construct to evolve in shape, colour, flavour, or nutritional state after deposition under defined external triggers [9,16–18]. Furthermore, because its workflow is largely digital, 3DFP can be reconfigured recipe-by-recipe at the point of need. This supports individualised, low-volume production that lessens reliance on centralised food-processing infrastructure and shortens the design-to-product cycle for clinical nutrition, decentralised provision, and emergency food supply [8,10,11,13].

Critically, however, no single category delivers all of these capabilities equally: the choice of additive manufacturing category constrains which classes of food substrate can be printed, the resolution and throughput that are achievable, and the compatibility of the deposited construct with subsequent post-processing and stimulus-responsive transformation. Within this categorical landscape, material extrusion presently provides the broadest substrate envelope and the deposition geometry most readily compatible with multi-material and stimulus-responsive constructs, motivating its selection as the scope of the present review. The operational rationale for this selection is developed in the following section by direct comparison against the alternative ISO/ASTM categories.

1.2 Material Extrusion in Food Applications

Material extrusion is the most widely adopted additive-manufacturing principle across both engineering and food domains, having been applied to polymers, metals, ceramics, and recycled-fibre composites as well as to food substrates [19–21]. Its prevalence in food 3D printing specifically reflects three engineering features that, taken together, accommodate the diversity of food substrates and the multifunctional design freedoms outlined above. First,

ACCEPTED PAPER

the substrate compatibility of MEX spans the full range of food-relevant viscoelastic regimes — animal and plant proteins, starches and other carbohydrates, fruit and vegetable purées, dairy systems, meat pastes, and functional bioactive-loaded gels — within a single hardware platform that requires only nozzle and pressure-profile adaptation [7,8,13]; chocolate-based foods exemplify the small subset of food substrates whose phase-change behaviour places them at the fused deposition modelling (FDM) end of MEX rather than within the ambient-hydrogel category, providing the foundational case studies on which much early food AM literature was built [22–26]. The other ISO/ASTM categories are, by contrast, each suited to substrate classes defined by their respective deposition physics (sinterable powders, bondable particulate beds, or low-viscosity inks), and the photopolymer-based VPP route remains constrained by the present unavailability of food-grade GRAS photoinitiators. Second, the ambient- or near-ambient processing window of MEX preserves thermolabile bioactives and protein structure that may otherwise be degraded under the laser fusion of PBF, or the melt-recrystallization step of phase-change MEX such as FDM of chocolate [11,22–28]. Third, multi-nozzle and coaxial co-extrusion configurations enable heterogeneous inks to be co-deposited within a single printed construct, establishing the asymmetric compositional distribution that serves as the prerequisite for stimulus-responsive 4D transformation [9,14–16]. The convergence of these features supports the simultaneous development of MEX along the ink-formulation, intelligent process control, post-processing, and 4D evolution domains examined in this review. Accordingly, the scope of the present review is bounded to MEX of viscoelastic hydrocolloid, protein, starch, fruit/vegetable, dairy, meat, and functional-bioactive-loaded substrates. Explicitly outside this scope are phase-change MEX, powder-based PBF and BJ , surface-decoration MJT (inkjet), bioprinting, cultured-meat scaffolding, and pharmaceutical 3D printing. In practice, however, this potential remains difficult to realise. Across these substrate classes, printability is governed by narrow, material-specific rheological windows; deposition is still largely executed under open-loop control without real-time correction; and the post-deposition and stimulus-responsive behaviours that distinguish 3DFP from conventional processing remain only partially characterised. Addressing these interlocking challenges calls for a review that examines ink design, intelligent process control, post-processing, and stimulus-responsive 4D evolution together rather than in isolation — an integrative perspective that, as the following section discusses, remains only partially developed in the existing literature.

1.3 Differentiation and Structure

Extrusion-based 3DFP has already been surveyed from several perspectives [9,12,14,17,29–37]; the existing reviews, however, share recurring scope limitations that the present review is intended to close, as summarised in Table 1. Earlier reviews (2019–2022), such as those by Teng et al. [12] and Hussain et al. [30], mapped the foundational material-class, printability, and personalised-food landscape, while providing limited treatment of intelligent process control or stimulus-responsive 4D evolution. Reviews from 2023 then deepened specific axes — Kadival et al. [31] and Outrequin et al. [35] formalised printability-assessment and biopolymer-rheology frameworks, and Shen et al. [9] surveyed physical-field pre-treatments — yet each remained bounded to a single axis. Furthermore, more recent reviews (2024), such as Shen et al. [9] and Teng et al. [12], introduced physical-field, modelling, and personalised-food perspectives, yet none integrates the full pipeline from computational modelling through data-driven prediction to real-time vision feedback. Similarly, the most recent multi-modality reviews (2025–2026) by Raut et al. [36] abd Chauhan et al. [37] consolidate emerging technologies and personalised-nutrition applications across multiple food-printing categories; however, their breadth precludes the extrusion-specific depth required for a unified treatment of intelligent process control and stimulus-responsive 4D evolution. Across this body of work, and to the authors' knowledge, no prior review organises 4D studies along an explicit trigger × response mechanism matrix, and none treats intelligent process control as a single closed-loop paradigm integrating offline modelling, data-driven prediction, and real-time vision feedback [38].

In contrast, the present review offers an integrated and critical synthesis of extrusion-based 3DFP, following the pipeline from ink formulation through intelligent process control, post-processing, and stimulus-responsive 4D transformation. It addresses the research gaps identified above by integrating cross-material ink-design strategies,

ACCEPTED PAPER

machine-learning-assisted printability prediction, real-time computer-vision feedback, and trigger × response classification of stimulus-responsive 4D studies within a single coherent framework. It further surveys state-of-the-art 4D transformation methods and frames extrusion-based food printing as a route towards intelligent, self-adaptive food-manufacturing systems. In doing so, it consolidates what earlier reviews treated in isolation and sets out a research agenda for the field.

The remainder of the review is organised to build a coherent picture of of intelligent, data-driven, and stimulus-responsive extrusion-based 3DFP. Fig. 1 visually outlines the operational scope and the section-by-section progression of the review. Section 2 lays the rheological foundations on which a successful extrusion process depends, with the engineering flow and the corresponding rheological characterisation at each stage summarised in Fig. 2. Building upon this, Section 3 surveys ink-design strategies across the principal food-substrate categories. Section 4 advances the discussion by examining the three-axis intelligent process control framework, which integrates offline computational modelling, data-driven artificial intelligence / machine learning (AI/ML) prediction, and real-time computer-vision feedback. Section 5 treats pre- and post-processing engineering, including the quality-control and regulatory considerations relevant to printed food products. Section 6 develops the stimulus-responsive 4D paradigm, classifying recent studies by trigger and response mechanism. Section 7 reviews application domains spanning clinical nutrition, decentralised food provision, and emergency food-supply scenarios. The review concludes with Section 8, which summarises the key findings and proposes a short- to long-term research roadmap. By integrating these distinct yet interconnected aspects, this review seeks to stimulate further research in the field, guiding the development of intelligent extrusion-based food-printing systems for clinical, personalised, and decentralised food production.

ACCEPTED PAPER

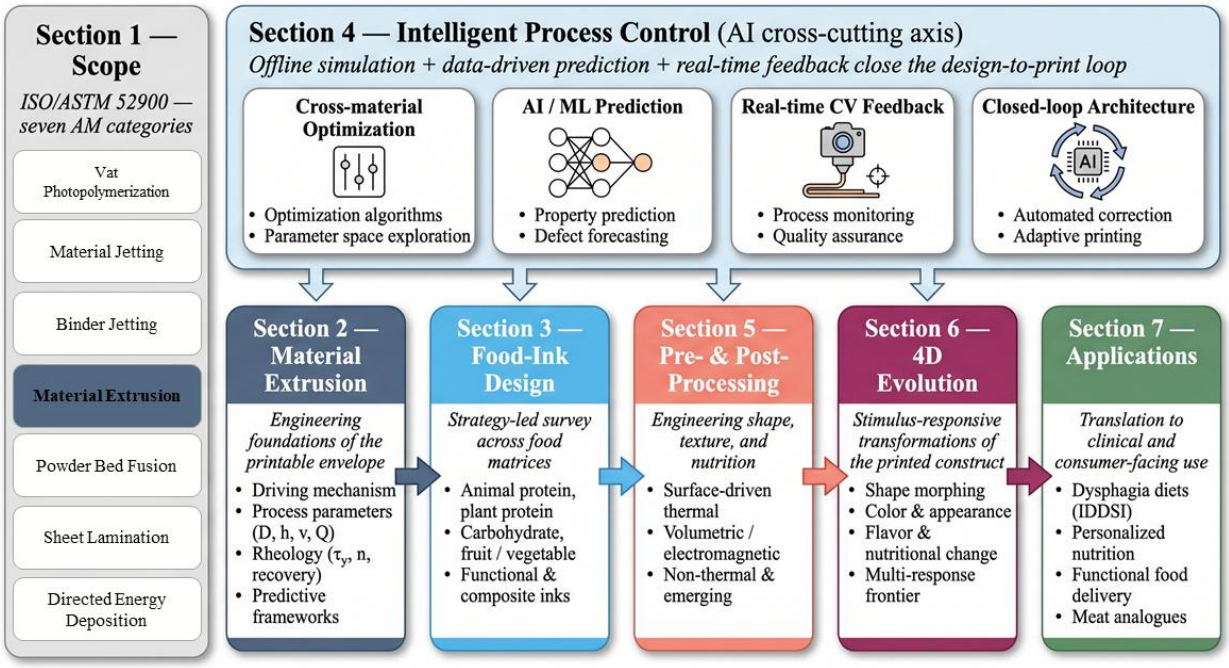


Fig. 1. Overview of this review on intelligent process control and stimulus-responsive 4D transformation in extrusion-based 3D food printing.

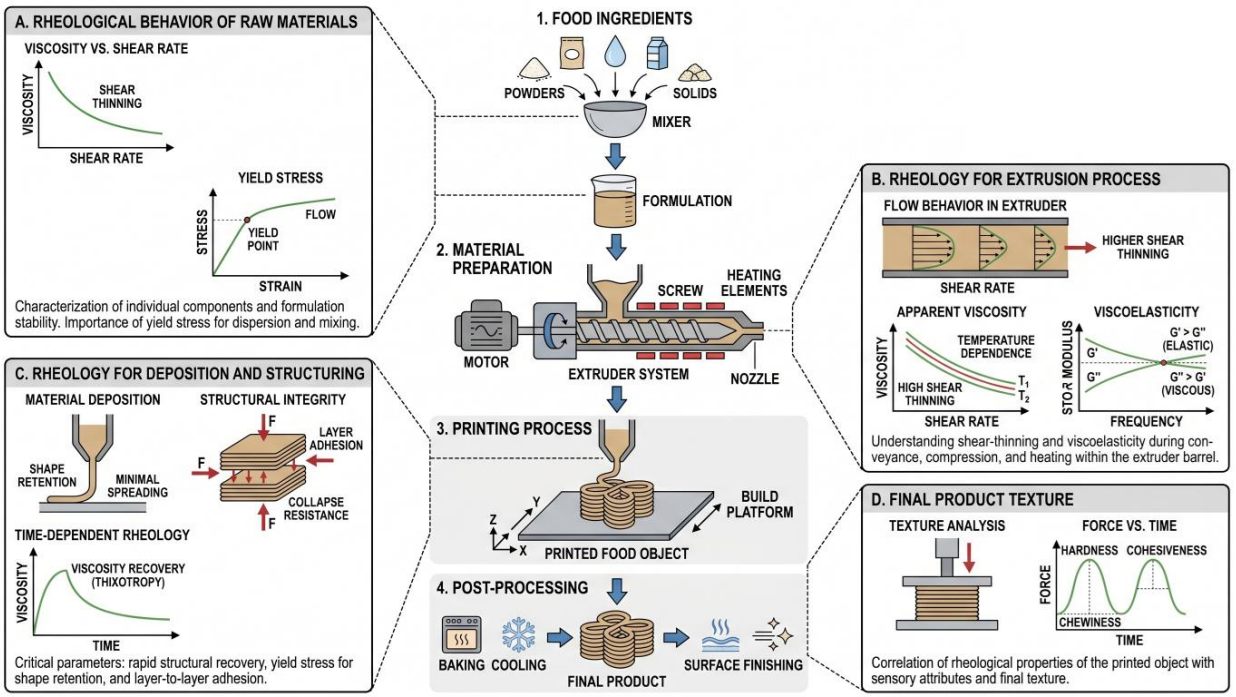


Fig. 2. Schematic of extrusion-based 3D food printing and its rheological foundations.

Table 1. Previous review papers on extrusion-based 3D food printing, ordered chronologically: scope, key contributions, and gaps addressed by the present review.

Year	Reference	Key contributions	Limitations
2026	[36]	• Surveyed advances across all four food-printing modalities. • Attempted cross-modality benchmarking.	• Multi-modality scope dilutes extrusion-specific depth. • AI/ML closed-loop pipeline not detailed.
2025	[37]	• Linked 3D and 4D printing to personalised nutrition. • Outlined stimulus-responsive food platforms.	• Multi-modality scope; extrusion-specific mechanism not developed. • Process-control axis and LF-NMR/ML integration absent.
2024	[32]	• Surveyed food extrusion across hot-melt, reactive, and 3D-printing contexts. • Reviewed material formulation, screw/die design, and process control.	• Conventional food-extrusion focus; MEX sub-modes not differentiated and printability not framed.
2023	[31]	• Consolidated qualitative and quantitative printability-assessment methods. • Linked rheometric and post-print metrics.	• Evaluated printability along a single axis; non-destructive LF-NMR and ML not integrated. • Real-time vision feedback not addressed.
2023	[35]	• Established a biopolymer rheological framework for printability. • Linked formulation variables to extrusion behaviour.	• Bounded to biopolymer inks. • Process-control and post-processing axes not covered.
2023	[9]	• Reviewed physical fields (microwave, RF, ultrasound, PEF) for ink pre-treatment. • Surveyed field–matrix interaction mechanisms.	• Confined to the physical-field perspective. • Post-print 4D evolution and AI feedback not integrated.
2023	[17]	• Compared mechanical, computational, data-driven, ML, and fuzzy-logic modelling approaches. • Assessed model classes for printability prediction.	• Addressed modelling only; rheology, LF-NMR, and real-time vision not integrated. • Proposed no closure of the experimental loop.
2022	[14]	• Surveyed plant-substrate inks across chocolate, dough, cereal, fruit/vegetable, and hydrogel systems. • Mapped hardware platforms and process variables. • Outlined defects, applications, and food-design potential.	• Broad-substrate survey; phase-change FDM not separated from ambient-hydrogel MEX. • Proposed no unified QC framework or AI/ML integration.

ACCEPTED PAPER

2022	[34]	• Synthesised rheological and mechanical behaviour across pre-, during-, and post-print stages. • Resolved material behaviour by processing stage.	• Confined to rheology and mechanics. • Volumetric and electromagnetic post-processing and AI feedback not covered.
2022	[29]	• Reviewed plant- and animal-protein inks. • Identified protein-specific printability factors.	• Bounded to protein substrates; carbohydrate and lipid systems out of frame. • Proposed no cross-material optimisation strategy.
2022	[30]	• Characterised cereal, starch, protein-gel, and dairy inks. • Summarised printability material by material.	• Proceeded material by material without cross-axis synthesis. • AI/ML and LF-NMR axes not covered.
2022	[12]	• Reviewed personalised foods spanning dysphagia, special-shape, and 4D–6D outlooks. • Surveyed consumer translation and clinical drivers.	• Application-focused; MEX-internal rheological mechanism less developed. • Ambient MEX not separated from phase-change MEX.
2019	[33]	• Pseudoplastic behaviour of carbohydrate, protein, lipid inks.• Rheology–printability link and personalised-nutrition outlook.	• Perspective overview only. • No quantitative QC framework or process-control closure.

2. Fundamentals of Extrusion-Based 3D Food Printing

This section examines the engineering foundations of material extrusion–based 3DFP — the hardware, operating parameters, ink rheology, and predictive frameworks that together determine whether a deposited construct retains its intended geometry. The discussion begins in Section 2.1 with the three extruder configurations commonly used in food MEX (syringe-pump, pneumatic extrusion, and screw-driven extrusion) and the rheological regimes for which each is most suitable (Fig. 3). Section 2.2 then reviews the principal process parameters — nozzle diameter, layer height, printing speed, and extrusion flow rate — and their coupling to deposition fidelity. Section 2.3 turns to the rheological conditions an ink must satisfy for both extrudability and shape retention, formulated as three coupled requirements on yield stress, shear-thinning behaviour, and recovery kinetics. Lastly, Section 2.4 surveys the predictive frameworks that have been applied in food MEX to anticipate printability prior to experimental trials, spanning physics-based CFD/FEA, low-field NMR characterisation, and machine-learning classification. Together, these four subsections frame the design space that subsequent sections traverse — substrate-specific ink formulation in Section 3, intelligent process control in Section 4, and post-processing and 4D engineering in Sections 5 and 6.

ACCEPTED PAPER

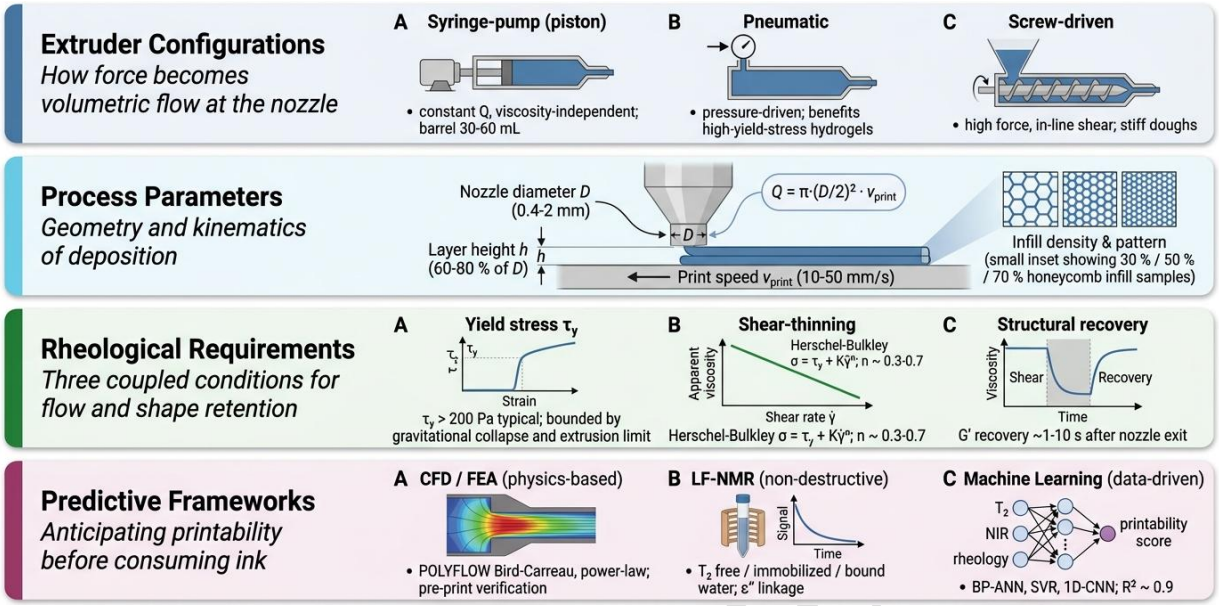


Fig. 3. Key aspects of extrusion-based 3D food printing: driving mechanism, process parameters, rheological requirements, and predictive frameworks for printability.

2.1 Extrusion Configurations

The extrusion driving mechanism converts the force applied at the print head into the volumetric flow rate at the nozzle, and three configurations are commonly used in food MEX — syringe-pump (piston-driven), pneumatic, and screw-driven extruders — distinguished by how this conversion is accomplished [30,31]. In the syringe-pump and screw-driven configurations the flow is produced by mechanical displacement — a piston or a rotating Archimedean screw advancing a defined volume — so that the delivery rate is set primarily by the kinematic input (piston speed or screw rotation) and is relatively insensitive to ink viscosity within the operating window. In the pneumatic configuration the ink is instead driven by a regulated applied pressure, so that the flow rate depends jointly on the pressure and the ink's apparent viscosity. Each is suited to a different rheological regime and imposes different constraints on ink formulation, throughput, and sanitation.

Syringe-pump extruders: Adapted from biomedical bioprinting and laboratory dispensing systems, syringe-pump extrusion has been among the most widely deployed driving mechanisms in food MEX since the early 2010s, owing to its mechanical simplicity and direct compatibility with small-batch food-ink research [39,40]. As illustrated in the top row of Fig. 4, the mechanism operates on the principle of positive volumetric displacement: a stepper-motor-driven piston advances at a controlled linear velocity v_p through a vertical barrel containing the pre-loaded ink, with the volumetric flow rate at the nozzle given by $Q = v_p \cdot A_{barrel}$, where A_{barrel} is the barrel cross-sectional area. Print operation begins with loading the pre-mixed ink into a disposable or reusable cartridge, engaging the piston, and advancing it continuously to displace the ink through the nozzle onto the build platform. The piston velocity is the primary process parameter, with nozzle diameter and barrel volume defining the secondary operating envelope.

The principal advantage of syringe-pump extrusion is the decoupling of flow rate from ink rheology within the operating window: Q is set by the kinematic input v_p alone and is largely independent of the ink's apparent viscosity, provided the rheology lies within the displacement-pump regime. This decoupling supports reproducible deposition across formulation batches, simplifies process-parameter mapping, and matches well to inks of moderate yield stress such as purées, soft gels, and surimi pastes — for which fish surimi gel has been systematically evaluated as a model viscoelastic food material for 3D printing [41]. The reusable cartridge geometry additionally permits straightforward

ACCEPTED

cleaning and sanitation between print runs — a non-trivial advantage in food-grade applications where cross-contamination must be controlled.

However, syringe-pump extrusion has the following limitations: (1) the bounded barrel volume restricts continuous production runs and necessitates frequent reloading, which is acceptable in research but constrains scale-up; (2) the maximum extrusion force is limited by the piston actuator's mechanical capacity, restricting the upper bound of ink yield stress that can be reliably extruded — stiff doughs and high-fibre cereal pastes typically exceed this bound; and (3) the pre-loaded ink can undergo storage-induced changes — rheological recovery, free-surface dehydration, microbial growth in unrefrigerated cartridges — that introduce batch-to-batch variability if the loading-to-print interval is not controlled.

Pneumatic extruders: Pneumatic extrusion was developed as an alternative driving route in which the mechanical piston is replaced by regulated compressed air acting on the free surface of the ink reservoir [39]. As illustrated in the middle row of Fig. 4, a regulated air pressure P_{air} is applied to the upper surface of the ink contained in a sealed cartridge, displacing the ink through the nozzle by pressure-driven flow rather than by positive volumetric displacement. The volumetric flow rate at the nozzle is consequently determined by the applied pressure and the ink's apparent viscosity at the nozzle shear rate, $Q = f(P_{air}, \eta(\dot{\gamma}))$, rather than by a kinematic input alone. Applied pressure, nozzle diameter, and print speed constitute the primary process parameters, with high-speed deposition studies identifying non-printing-movement effects and minimum-acceleration limits at the upper end of this range [42], with the pressure regulator providing fine control over the deposition rate.

The principal advantages of pneumatic extrusion are its high accessible extrusion force at modest hardware cost and its compliant flow response with respect to ink rheology variations. The applied pressure can be raised well beyond the practical limit of piston actuation, supporting the extrusion of high-yield-stress hydrogels (yield stress $\tau_y > 1000$ Pa) and gelled plant proteins for which syringe-pump force is insufficient. Cartridge exchange between print runs is rapid, since no mechanical engagement of the piston is required, supporting workflows that involve multiple ink formulations or multi-material deposition in a single session.

However, pneumatic extrusion has the following limitations: (1) the volumetric flow rate is rheology-dependent through the apparent viscosity, so batch-to-batch variation in ink composition propagates directly into deposition-rate variation, particularly for strongly shear-thinning systems where the apparent viscosity at the nozzle is hard to predict; (2) the start–stop response is slower than for piston-driven systems because the compressed-air volume must equilibrate within the reservoir, producing transient under- or over-extrusion at the beginning and end of each filament; and (3) high-yield-stress inks can develop pressure-induced channelling in the reservoir when the applied air pressure preferentially evacuates a low-viscosity domain, leaving behind a high-viscosity residual that is inaccessible to further extrusion.

Screw-driven extruders: Adapted from industrial food-extrusion processing, screw-driven extruders introduce a rotating Archimedean screw inside a heated or unheated barrel to mechanically convey, mix, and advance the ink toward the nozzle [40]. Although the screw pressurises the ink, its delivery rate is set primarily by the drag flow of screw speed and geometry, placing it — with the syringe pump — among the displacement-type configurations rather than the pressure-driven pneumatic route. As illustrated in the bottom row of Fig. 4, the screw rotates at a controlled angular velocity (typically 10–60 rpm) and conveys the ink through three sequential zones — conveying, mixing, and pressurisation — before delivery to the nozzle. The volumetric flow rate at the nozzle scales with both the screw rotation speed and the screw geometry, with in-barrel shear rates that can reach 10^2–10^3 s^{-1} — substantially higher than those experienced in either syringe-pump or pneumatic mechanisms. A hopper feeds granular or dough-like substrate continuously into the conveying zone, supporting continuous-resupply operation rather than batch loading.

ACCEPTED PAPER

The principal advantages of screw-driven extrusion are its higher accessible extrusion force, its capacity for continuous-resupply operation, and its in-line shear-induced viscosity reduction. The screw mechanism generates pressures and torques that exceed both syringe-pump and pneumatic systems, supporting the extrusion of stiff doughs (cereal-based, high-fibre, high-protein), oleogels, and composite matrices for which the other two mechanisms cannot generate adequate flow. The continuous hopper feed eliminates the barrel-volume constraint that limits syringe-pump runtime, supporting longer production runs. In addition, the in-barrel shear flattens the apparent-viscosity profile of strongly shear-thinning inks, effectively performing an in-line homogenisation that improves downstream extrusion stability — a function not available in piston- or pressure-driven systems.

However, screw-driven extrusion has the following limitations: (1) higher capital cost relative to syringe-pump and pneumatic systems, since screw geometry, drive motor, and barrel must be matched to the substrate class — laboratory-scale screw extruders are typically 5–10× the cost of comparable syringe systems; (2) demanding cleaning and sanitation requirements, since the screw and barrel are difficult-to-disassemble surfaces on which food residue can accumulate, raising hygiene concerns for food-grade applications; and (3) the in-barrel shear can mechanically damage shear-sensitive components such as encapsulated bioactives, probiotic cells, and temperature-sensitive flavour compounds, restricting its use for the encapsulated-payload constructs reviewed in Section 6.3.

Comparative analysis of the three mechanisms: The three configurations exhibit different operational dynamics, as summarised in Fig. 4. Syringe-pump systems typically operate at piston velocities of 0.1–10 mm/s within a bounded 30–60 mL barrel, delivering a viscosity-independent volumetric flow rate that is well suited to high-precision, small-batch deposition. Pneumatic systems operate at 0.05–0.6 MPa applied pressure with an unbounded reservoir, producing a flow response that scales with the ink's apparent viscosity at the nozzle shear rate. Screw-driven systems, with typical rotation speeds of 10–60 rpm, generate substantially higher extrusion forces and are uniquely capable of in-line shear-induced viscosity reduction at the cost of higher capital expense and more demanding cleaning protocols. These differences in flow generation directly affect the rheological window each mechanism can accommodate, leading to different ink-formulation strategies and process-monitoring requirements.

The choice among mechanisms is also reflected in the substrate classes for which each is best suited. Syringe-pump systems are matched to inks with moderate yield stress ($\tau_y \approx$ 200–1000 Pa) and moderate apparent viscosity (10^2–10^3 Pa·s), covering most purées, gels, and surimi-based inks reported in Section 3.1. Pneumatic systems extend the operating envelope to high-yield-stress hydrogels ($\tau_y >$ 1000 Pa) where positive displacement at acceptable piston force becomes impractical, but introduce flow-rate variability for strongly shear-thinning systems. Screw-driven systems remain the practical choice for stiff doughs and high-fibre cereal inks (Section 3.3), where neither piston force nor pneumatic pressure can drive adequate flow through the nozzle. These mechanism–substrate correspondences, together with the rheological conditions of Section 2.3, define the operational envelope within which the substrate-specific formulation strategies of Section 3 are examined.

This displacement/pressure distinction also frames a scale-up tension that the three configurations do not resolve equally. Piston (syringe) systems impose the gentlest mechanical environment — low shear, no in-barrel heating — and therefore best preserve shear- and heat-sensitive payloads such as probiotics, encapsulated bioactives, and stimulus-responsive microcapsules (Sections 3.5, 6), yet their bounded barrel volume locks them out of continuous production. Screw systems remove the volume constraint and provide the throughput required for commercial operation, but the same in-barrel shear (10^2–10^3 s^{-1}) and localised heating that homogenise stiff doughs can degrade the very payloads that distinguish functional and 4D constructs. Scale-up is therefore not a simple hardware substitution but a change in the mechanical and thermal history experienced by the ink, and the appropriate configuration has to be considered against the shear- and heat-sensitivity of each payload — together with the mitigation strategies (e.g., screw-geometry and thermal management, post-extrusion stabilisation) examined in Sections 3.5 and 6 — rather than assumed to transfer directly from laboratory-scale syringe deposition.

ACCEPTED PAPER

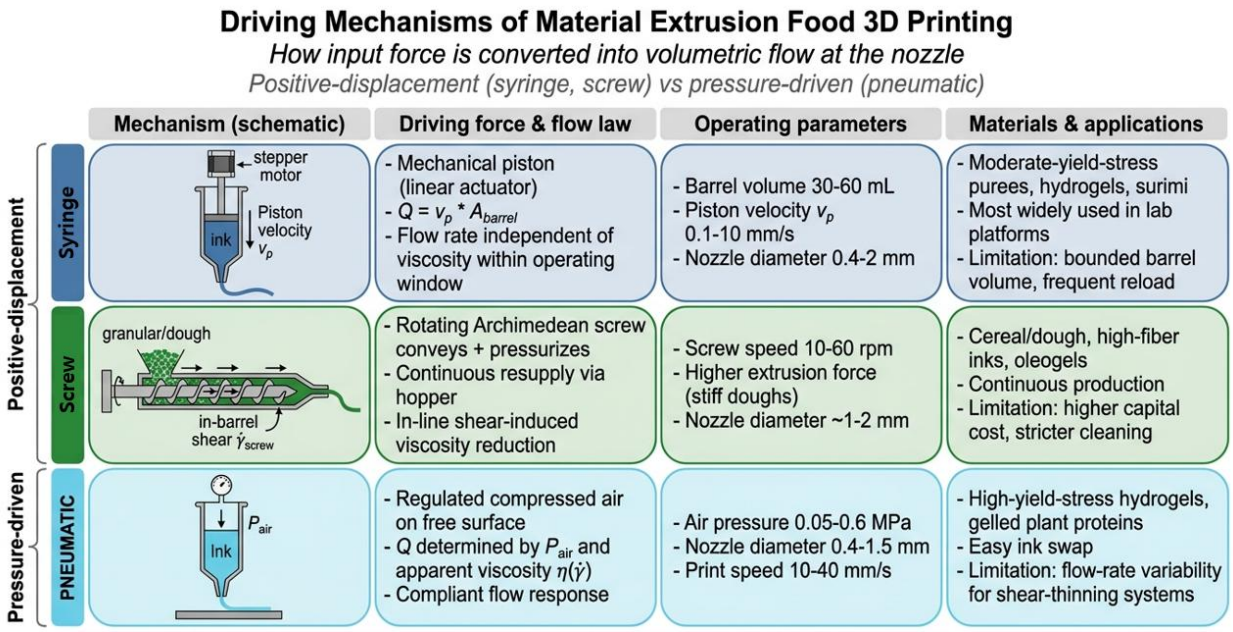


Fig. 4. Comparison of the three driving mechanisms used in extrusion-based 3D food printing: syringe-pump, pneumatic, and screw-driven.

2.2 Process Parameters

The geometric fidelity of the deposited construct is determined at the printing stage by four primary process parameters that operate jointly with the ink rheology [34,43]. Three of these parameters — nozzle diameter, layer height, and printing speed — are set on the printer hardware before deposition begins, while the fourth — extrusion pressure or volumetric flow rate — is co-optimised with the printing speed through a volumetric-balance condition. Together with infill density and pattern, they bound a process-parameter space within which any food ink must satisfy the rheological conditions reviewed in Section 2.3.

Nozzle diameter sets the minimum feature width and the shear rate experienced by the ink at the nozzle outlet, with shear rate scaling inversely with the cube of the diameter under Hagen–Poiseuille flow [44]. For a fixed volumetric flow rate Q, the apparent wall shear rate at the nozzle is $\dot{\gamma}w = 4Q/(\pi R^3)$, where R is the nozzle radius; halving the diameter raises $\dot{\gamma}w$ by a factor of eight, potentially exceeding the ink's recoverable shear range and producing post-deposition relaxation defects. The operating range observed across substrate categories converges around 0.8–1.5 mm: a Box–Behnken response-surface optimisation of a rice-flour–jaggery system identified 1.5 mm nozzle diameter as the optimal value within its tested range [39], and similar 1.0–1.5 mm optima have been reported for surimi–starch systems [45] and pea-protein gels [46,47]. Sub-millimetre nozzles (≤ 0.6 mm) are reserved for high-resolution constructs at the cost of throughput and an elevated risk of clogging in particulate-laden substrates.

Layer height, typically set to 60–80 % of the nozzle diameter, sets the contact area between deposited and underlying layers and therefore the interlaminar adhesion [45,48]. Smaller layer heights enhance interlaminar bonding by maximising the contact-area-to-volume ratio of the deposited filament, but increase total print time linearly with the inverse of layer height. The rice-flour–jaggery Box–Behnken study [39] reported an optimum below this typical

ACCEPTED

window; the 60–80 % range adopted in most surimi and starch substrates [45,48] reflects the trade-off between interlaminar adhesion and print throughput.

Printing speed (typically 10–50 mm/s in food MEX) determines the residence time of the ink at each deposition point, with low speeds producing over-deposition (filament piling, loss of dimensional fidelity) and high speeds producing under-deposition (filament thinning, discontinuity) [48,49]. The optimum speed is substrate- and ink-rheology-specific: 20 mm/s for rice-flour–jaggery [39], 20–30 mm/s for surimi–starch [45], and 10–20 mm/s for low-yield-stress pea-protein gels [46,47]. Derossi et al. [42] systematically extended the upper bound by examining material deposition behaviour at speeds above 50 mm/s; the resulting accuracy degradation defines the practical upper edge of the printing-speed window for biopolymer inks. The dependence of dimensional fidelity on residence-time-modulated viscosity recovery is the kinematic origin of the cross-coupling between printing speed and ink rheology examined from the material-side in Section 2.3.

Extrusion pressure (or volumetric flow rate) is matched to the printing speed through the volumetric balance condition $Q = \pi(D/2)^2 \cdot v_{print}$, where Q is the volumetric flow rate, D is the nozzle diameter, and v_{print} is the printing speed; deviation from this balance produces the over- and under-extrusion defects that in-line vision systems are designed to detect (see Section 2.4 and Section 4). The applied extrusion pressure is in turn linearly related to the ink's flow stress and zero-shear viscosity in aqueous food formulations, as Zhu et al. demonstrated for tomato-paste-based ink across multiple formulations [28]; fat-based inks deviate from this linear regime owing to strain-hardening behaviour and require higher extrusion forces. The volumetric-balance condition is the kinematic constraint that ties printer settings to ink rheology, and its violation accounts for the majority of dimensional defects detected by the computer-vision systems reviewed in Section 4.

Beyond these four core parameters, infill density and pattern set the internal lattice geometry of the deposited construct, which in turn propagates into post-processing outcomes — infill density governs post-fry oil uptake [45,50] and dictates microwave puffing trajectory [51]. Common infill densities of 30–50 % balance structural stability against deposition time, with lower infills (≤ 30 %) used for purpose-engineered porosity in dehydration-driven 4D shape morphing (Section 6) and higher infills (≥ 70 %) used where compressive strength matters. The five process parameters reviewed above operate jointly with the ink rheology, which is examined in Section 2.3 as a set of intrinsic material-side constraints. Through this dependence, decisions made at the printing stage propagate into the post-processing and 4D engineering domains examined in Sections 5 and 6: the same nozzle diameter that determines feature width also defines the wall shear rate at which an ink's recovery kinetics must be characterised, and the same printing speed that determines throughput also sets the residence time within which the rheological recovery condition (Section 2.3) must be satisfied. Cross-substrate parameter optimisation across the substrate classes reviewed in Section 3 has converged toward the 1.0–1.5 mm nozzle / 60–80 % layer-height / 10–30 mm/s speed window, bounded by the substrate-specific rheological envelopes summarised in Section 2.3.

Despite the convergence of process-parameter windows across substrate classes, three challenges remain in the cross-material translation of these parameters: (1) substrate-specific optima — 1.5 mm nozzle for rice-flour–jaggery [39] and 1.0–1.5 mm for surimi–starch [45] — transfer poorly across compositionally distant substrates, limiting the development of a single parameter-mapping protocol; (2) the kinematic coupling between printing speed and the rheological recovery time of Section 2.3 has not, to the authors' knowledge, been formalised as a substrate-agnostic predictive relation, leaving printing-speed selection as an empirical rather than a derived process choice; and (3) infill density and pattern influence post-fry oil uptake [45,50] and MW puffing trajectory [51] through couplings whose quantitative form remains substrate-specific. Resolving these challenges would extend process-parameter optimisation from single-substrate case studies toward generalisable design rules.

ACCEPTED PAPER

2.3 Rheological Requirements

The rheological requirements that an ink must satisfy to be successfully extruded and to hold its deposited shape can be expressed as three coupled conditions [27,28,35]: a sufficient yield stress to prevent post-deposition gravitational collapse, a substantial degree of shear thinning to permit smooth flow through the nozzle, and rapid post-extrusion recovery of the storage modulus. The Herschel–Bulkley constitutive model $\sigma = \tau_y + K \cdot \dot{\gamma}^n$ — with τ_y the yield stress, K the consistency index, and n the flow-behaviour index — provides the unifying framework within which all three conditions can be quantified [28,35].

The yield-stress condition (τ_y) requires that the ink possess a finite static yield stress sufficient to resist gravitational collapse of the deposited layer, while remaining low enough to be extrudable at the nozzle pressure available to the printer [44,48]. The yield-stress window is bounded below by gravitational collapse (τ_y > 200 Pa for self-supporting deposited layers in food gels [28,35]) and bounded above by the maximum extrusion pressure that the driving mechanism (Section 2.1) can deliver. Reported τ_y values for printable food inks span approximately 200–2000 Pa across substrate categories: 200–500 Pa for low-yield gels (mashed potato [27], pea-protein–alginate blends [46]), 500–1200 Pa for surimi–starch matrices [45,48], and ≥ 1000 Pa for stiff hydrocolloid–starch composites such as carrageenan–xanthan–starch [52]. The narrowness of this operating window — typically a single decade in τ_y — is one of the central reasons that printability prediction (Section 2.4) requires non-destructive measurement of multiple rheological observables rather than reliance on a single yield-stress threshold.

The shear-thinning condition requires that the ink's apparent viscosity decrease substantially under the shear rate experienced at the nozzle (10–10^3 s^{-1}), permitting smooth flow during deposition, and recover rapidly to its zero-shear value upon ejection from the nozzle [44,48]. In the Herschel–Bulkley framework $\sigma = \tau_y + K \cdot \dot{\gamma}^n$, the flow-behaviour index n quantifies the degree of shear thinning: $n < 1$ corresponds to shear-thinning behaviour, $n = 1$ to Bingham-plastic, and $n > 1$ to shear thickening. Across printable food inks, n is typically observed in the 0.3–0.7 range [28,35,48], with starch-based inks toward the lower end (n = 0.3–0.5) and protein-based inks toward the upper end (n = 0.5–0.7); the consistency index K spans approximately 10–500 Pa·s^n depending on substrate composition. Inks with $n > 0.7$ (insufficient shear thinning) develop excessive pressure drops at the nozzle and exhibit nozzle clogging, while inks with $n < 0.2$ (excessive shear thinning) show insufficient post-extrusion structural recovery.

The recovery condition requires that the ink's storage modulus (G') recover within milliseconds-to-seconds after the high-shear nozzle event so that the deposited filament transitions back to its solid-like state before the next layer is deposited above it [49]. Time-resolved oscillatory measurements have demonstrated that printable food inks typically recover ≥ 80 % of their pre-shear G' within 1–10 s; faster recovery (< 1 s) is observed in strong physical-network gels (carrageenan, gellan), while slower recovery (10–60 s) is observed in particle-stabilised or weak-protein gels and constrains the maximum achievable layer-deposition rate.

Inks that fail any of these three conditions show characteristic defects: low τ_y produces sagging and base spread; insufficient shear thinning produces nozzle clogging and over-pressure events; slow recovery produces interlaminar smearing and resolution loss. Each condition is influenced by a distinct compositional lever — hydrocolloid concentration acting primarily on τ_y and recovery kinetics [44,48], the protein-to-starch ratio on the shear-thinning index [45,49], and salt and crosslinker concentration on recovery kinetics [49]. The independent action of these compositional levers underlies the rationale for multicomponent ink design: in carrageenan–xanthan–starch composite systems, carrageenan supplies the dominant τ_y contribution, xanthan modulates the shear-thinning index, and starch provides the post-extrusion structural recovery, allowing all three rheological conditions to be engineered simultaneously [52]. Hydrocolloid incorporation in pork-paste systems (xanthan + guar gum at total 0.36 % w/w) similarly demonstrates that targeted hydrocolloid blending can shift the rheological envelope from non-printable to printable [44], establishing compositional–rheological coupling as the principal degree of freedom in ink design. The composite picture across substrate categories is that the rheological operating window is narrow but consistent: $\tau_y \approx$

ACCEPTED PAPER

200–2000 Pa, shear-thinning index $n \approx 0.3–0.7$, and G' recovery ≥ 80 % within 1–10 s. Substrates that reside outside this window — fat-rich materials with strain-hardening behaviour [28], purées with $\tau_y \ll 200$ Pa, or particulate suspensions with poor recovery — require either pre-treatment (microwave, ultrasound, hydrocolloid blending) or post-extrusion stabilisation to enter the printable regime, as Section 3 examines for each substrate class. Whether a candidate formulation actually meets these conditions cannot be determined from rheological characterisation alone; pre-print verification through computational simulation, non-destructive measurement, or data-driven prediction is required, and these three predictive framework axes are reviewed in Section 2.4.

Despite the convergence of food-ink rheology toward the $\tau_y \approx 200–2000$ Pa / n ≈ 0.3–0.7 / G′ recovery ≥ 80 % within 1–10 s window, three challenges remain in operationalising this window as a printability criterion: (1) the rheological boundaries reported across substrate classes appear to span a single decade in each observable, and standardised cross-laboratory protocols for declaring an ink "printable" within this window have not yet been consolidated [35]; (2) the G′ recovery measurement protocol — most commonly characterised by time-resolved oscillatory rheology — varies across laboratories in terms of imposed strain, frequency, and recovery-time window, limiting cross-study comparability; and (3) the cross-coupling among the three compositional levers (hydrocolloid concentration, protein-to-starch ratio, salt and crosslinker concentration) has been demonstrated within single substrate families but, to the authors' knowledge, has not been systematically mapped across compositionally distant substrates. These challenges define the empirical scope within which the predictive frameworks of Section 2.4 must operate.

2.4 Predictive Frameworks for Printability

The transition from rheological characterisation to a successfully deposited construct depends on the ability to anticipate printability before the printing trial begins, and three predictive framework axes have been pursued in food MEX.

Computational fluid dynamics (CFD) and finite-element analysis (FEA) provide offline simulation of the ink's shear-rate, pressure, and velocity fields within the nozzle and at the deposition interface. POLYFLOW-based finite element method (FEM) CFD applied to five cereal-grain pastes (buckwheat, brown rice, mung bean, Job's tear, black rice) using the Bird–Carreau viscosity model has reproduced the relative printability of each substrate, with experimental extrusion outcomes consistent with the simulation-based ranking [53]. The same FEM framework was extended to plant-protein–starch composites in rice-starch / peanut-protein-isolate systems, where POLYFLOW non-Newtonian flow simulations resolved both pressure and shear-stress distributions within the nozzle and indicated that these distributions predict not only extrudability but also post-extrusion deformation modes of the deposited construct [54]. Power-law fluid CFD applied across starch-based gels indicated that a low-flow-index, strongly shear-thinning envelope is workable for screw-driven extrusion of starch matrices for screw-driven extrusion of starch matrices [55]. The primary function of CFD in this context is pre-print verification: the simulation indicates whether the proposed nozzle geometry, ink rheology, and printing speed combination is operable before experimental ink is consumed.

Low-field nuclear magnetic resonance (LF-NMR) complements CFD by providing non-destructive measurement of the transverse relaxation time (T_2) distribution of free, immobilised, and bound water within the ink matrix in less than 60 s per sample. T_2 distributions have been correlated with rheology and printability in mashed-potato systems [56] and extended to surimi gels coupled with dielectric loss factor (ε'') measurement [57]. The LF-NMR + ε'' pairing introduces a measurement axis that propagates beyond the printing stage: ε'' is the same parameter that drives microwave dielectric heating in Section 5 and selective microwave (MW) absorption in Section 6, providing a single physical observable that links ink design with the processing and 4D evolution stages.

Machine learning (ML), finally, closes the gap between non-destructive measurement and quantitative printability classification. Back-propagation artificial neural networks (BP-ANN) trained on LF-NMR T_2 inputs reach discrete printability scoring (0/1/2) for five polysaccharide hydrogel systems — gellan, locust bean, xanthan, pectin, and tara

ACCEPTED PAPER

gums — with free-water T_2 identified as the primary discriminating variable [58]. BP-ANN models for surimi–starch [45] and corn-starch ink [59] have generalised this framework across substrate categories, reaching $R^2_{adj} = 0.894$ on gelatinisation-temperature and starch-concentration operating windows. Comparative ML benchmarking across LF-NMR and dielectric input streams supports indirect prediction of polysaccharide-gel rheology and printability across substrate families [57,60].

These three predictive framework axes — physics-based CFD/FEA, non-destructive LF-NMR measurement, and data-driven ML prediction — span a range from offline simulation to data-driven classification, and together complement the rheological framework of Section 2.3 by providing pre-print verification. The complementary in-situ feedback layer (real-time computer vision) operates after deposition has begun and is treated as a separate axis of intelligent process control in Section 4 (see Section 4.2 for cross-material AI/ML treatment, and Section 4.3 for real-time computer-vision feedback).

Despite the complementarity of these three predictive axes, three challenges constrain their integration into a single pre-print verification framework: (1) CFD constitutive parameters (Bird–Carreau, power-law) require accurate rheological inputs that are not always available for compositionally complex multi-component food matrices, limiting predictive accuracy as substrate complexity rises; (2) LF-NMR T_2 measurement protocols appear to remain laboratory-specific in terms of relaxation-time gating and water-state assignment, restricting cross-study transfer of the T_2–printability mapping; and (3) cross-validation among physics-based, non-destructive, and data-driven axes has rarely been reported on a single ink within a single study, leaving the relative accuracy and computational cost of the three axes substrate-specific rather than benchmark-comparable. Resolving these challenges would convert pre-print verification from a substrate-tailored exercise into a generalisable screening tool.

Together, the four engineering layers reviewed in this section — driving mechanism, process parameters, rheological state, and predictive framework — frame the design space within which any food ink must be developed for a printable construct. The following section examines how this design space has been navigated across the major food-substrate categories that constitute current 3D-food-printing practice.

ACCEPTED PAPER

3. Food Materials for Extrusion-Based 3D Food Printing

The four engineering layers reviewed in Section 2 define the design space within which any ink must be developed; this section turns from that generic design space to the substrate-specific formulation strategies that have been pursued across the major food-substrate categories. The selection and formulation of printable food materials is a central determinant of process success in extrusion-based 3DFP, since material properties directly govern both extrusion behaviour and post-deposition structural integrity. As established in Section 2.3, a printable material must simultaneously exhibit sufficient fluidity to flow through a narrow nozzle under applied pressure and sufficient viscoelasticity to maintain its deposited shape without collapsing [30–33] — a balance regulated primarily by apparent viscosity, yield stress, and the storage and loss moduli (G' and G''). Over the past decade, a diverse range of food substrates has been investigated for this purpose, spanning animal proteins, plant proteins, carbohydrates, fruits, vegetables, mushrooms, and composite functional systems. The discussion begins in Section 3.1 with animal protein-based materials, where intrinsic gel-forming capacity provides the starting point for surimi-, meat-, dairy-, and egg-based inks. Section 3.2 then examines plant protein-based materials, focusing on soy and pea protein systems and the reformulation strategies used to compensate for their lower native gel strength. Section 3.3 turns to carbohydrate-based materials, where starch gelatinisation state and hydrocolloid architecture dominate printability. Section 3.4 reviews fruit-, vegetable-, and mushroom-based substrates, which are constrained by high moisture content and low structural biopolymer concentration. Lastly, Section 3.5 considers composite and functional materials, including high-oil systems, by-product streams, and bioactive-loaded inks. Table 2 provides a cross-cutting overview of these categories with their principal printability constraints, research approaches, and primary references.

Table 2. Overview of food substrate categories used in extrusion-based 3D food printing: principal printability constraints and research approaches reported in the literature.

Category	Food Material	Principal Printability Constraints	Research Approaches	Ref.
Animal protein–based	Surimi (shrimp, mackerel, trout, carp, cod)	Low gel strength; protein network disruption on freeze–thaw.	Starch / MTGase reinforcement; coaxial extrusion; ultrasound thawing; LF-NMR prediction.	[15,45,48,49,61–64]
	Cooked meat paste; restructured steak	Reduced viscoelasticity after cooking; no continuous gel matrix.	Hydrocolloids (XG, guar, carrageenan, LBG); starchy binder; coaxial extrusion for marbling.	[44,65–68]
	Egg yolk/white; soft cheese; dairy composites	Weak ambient gelation; printability sensitive to protein–fat ratio and thermal history.	Thermal gelation; protein–carb ratio tuning; starchy filler; print-temperature control.	[69–73]
Plant protein–based	Soy protein isolate (SPI); SPI composites	Globular structure with low solubility; pH / ionic / thermal sensitivity.	NaCl / XG / gelatin; microwave–salt pretreatment; polysaccharide emulsion; post-print 4D stimulation.	[16,74–79]
	Pea protein isolate (PPI);	Low solubility and gel strength; tailing in	Alginate blending + ALM simulation; WHC	[46,47,80,81]

ACCEPTED PAPER

	PPI–alginate; Pickering emulsions	fruit composites; shear-induced volatile loss.	normalisation; Pickering emulsion encapsulation.	
Carbohydrate-based	Rice flour; cereal doughs; brown-rice gel	Weak ambient gelation; bran-induced browning; moisture-dependent printability.	Box–Behnken optimisation; XG–GG blends; microwave/UMCH gelatinisation; HIU pretreatment.	[39,40,82–87]
	Modified starches (potato, wheat, cassava, buckwheat)	Native crystallinity limits gelatinisation; narrow printable window.	RF / PEF / DHT physical modification; Ca^{2+}–MW crosslinking; CFD pre-screening.	[53,88–93]
Fruit, vegetable & mushroom–based	Potato/yam gel; pumpkin; carrot; rose-yam; red ginseng	High moisture; low structural biopolymer; post-processing instability.	Infill / pattern texture design; SIDF fibre addition; MVD vs. FD drying; oleogel structuring.	[18,50,51,94–99]
	Mushroom (button, shiitake, black fungus); vegetables	High moisture and fibrous structure; species-specific hydrocolloid needs.	Substrate-adaptive hydrocolloid selection; IDDSI-compliant formulation.	[100–103]
Composite & functional	High-oil paste; beeswax oleogel + potato starch	Lipid > ~20 % destabilises continuous phase; phase separation under shear.	Cold-induced network strengthening (4 °C, 24 h); oleogel scaffold.	[96,104]
	Spirulina residue; okara	By-products lack intrinsic printable rheology; coarse heterogeneous particles.	Heat + moisture pretreatment; ultrasound + homogenisation; particle reduction < 100 µm.	[105–107]
	Probiotic and antioxidant-fortified systems	Probiotic viability and bioactive losses under extrusion + heat.	Alginate–gelatin encapsulation; SFD + freeze-drying; alginate microbeads.	[108–111]

3.1 Animal Protein-Based Materials

Animal protein-based materials have been studied extensively in extrusion-based 3DFP because of the intrinsic gel-forming capacity and nutritional value of proteins derived from seafood, meat, poultry, dairy, and egg sources [28,29]. Their printability is sensitive to protein concentration, ionic environment, temperature, and additive composition, and accordingly requires precise formulation control.

Among seafood-derived materials, surimi has been studied most extensively due to its strong gel-forming ability and commercial relevance. Starch addition is the most widely adopted strategy for improving surimi printability: 6 % cross-linked starch in shrimp surimi produced the optimal combination of apparent viscosity, G', G'', hardness, and cohesiveness, improving both extrusion smoothness and dimensional accuracy [61]; complementary protein-formulation strategies for restructured meat printability have been reviewed in the broader protein-paste literature

ACCEPTED PAPER

[68]. Enzymatic crosslinking via microbial transglutaminase (MTGase) offers an additive-free alternative; 0.3 % MTGase in mackerel surimi produced the highest gel strength and densest protein network, although cooking loss increased with dosage [48]. Beyond formulation, pre-print handling conditions are equally consequential: ultrasound-assisted thawing of silver-carp surimi at 100 kHz minimised protein structural damage and yielded the highest post-printing shape retention, hardness, and chewiness among the tested frequencies, while reducing thawing time by roughly 14–40 % relative to water immersion [49]. For non-destructive printability screening, LF-NMR relaxometry parameters (T_2(MP) and A_{22}) in surimi–starch systems showed strong correlation with printability-determining rheological properties, supporting polynomial regression models that predicted printing accuracy (R^2 = 0.88) and stability (R^2 = 0.93) [45] (see Section 4.2 for cross-material AI/ML treatment).

Coaxial extrusion has expanded the structural possibilities of surimi-based printing. Insertion of a κ-/ι-carrageenan protein-substitute solution into the surimi core enabled up to 50 % surimi replacement while maintaining printing accuracy and post-processing stability [62], and coating surimi filaments with 12 % potato-starch solution reproduced the fibrous microstructure and shear strength of commercial imitation crab meat [62]. In a multi-material approach, co-extrusion of surimi-based ink and plant-based ink through a single nozzle produced micro-fibrous constructs in which post-steaming cooling induced differential fibre formation, yielding lateral strength exceeding longitudinal strength — an anisotropy characteristic of natural skeletal muscle [15]. The addition of dietary fibre and lipids to fish protein gels introduces complex interactions: in cod-protein composite gels, printability was retained at IN:SDF ratios of 7:3 or 5:5 and flaxseed-oil contents of 10 % or below, whereas excessive inclusion caused network entanglement and reduced free-water mobility [63].

Meat- and poultry-based materials require rheological modification to achieve printability, since cooked meat pastes typically lack the viscoelastic network needed for self-supporting deposition. Hydrocolloids are the primary route: cooked beef paste with xanthan gum (XG), guar gum, carrageenan, or LBG at 0.5–1 % maintained a printable viscosity of 108–350 Pa·s and reached International Dysphagia Diet Standardisation Initiative (IDDSI) levels 5, 6, and 7 [65], while cooked pork paste with XG and guar gum (0.36 %) showed shear-thinning and self-supporting capacity consistent with IDDSI transitional-food classification [44]. Ground chicken required addition of refined wheat flour (2:1 ratio) for printability, with air-drying and frying post-processing yielding customised nuggets at 166.72 kcal/100 g [66]. Multi-material coaxial printing of lean and fat pastes enabled programmable marbling patterns in restructured beef steak, with 10 % fat paste yielding the most favourable post-heat texture [67].

Dairy- and egg-derived materials are distinguished by thermoreversible phase transitions that can be exploited to control extrusion and solidification. In hot-extrusion printing, structural deformation in carrageenan–gelatin blends, processed cheese, and sodium caseinate was attributed to slow cooling and creep under sustained loading; the authors recommended setting the print temperature slightly above the material's gelation temperature [69]. Egg yolk thermally treated at 76 °C for 8 min produced the optimal viscoelastic state for additive-free printing, with G', G'', and viscosity increasing monotonically with heating duration [70]. In dairy matrices, WPI:maltitol = 4:2 in soft cheese produced the best dimensional stability [71], while an SSMP(55):HDMP(5) composite produced the highest yield stress (1211.8 Pa) and G' (7026.4 Pa) among the tested dairy blends [72]. Blending egg yolk or white with rice flour (1:2 w/w) rendered otherwise unprintable egg components suitable for high-resolution printing at 600–800 mm/min [72].

3.2 Plant Protein-Based Materials

Plant protein-based materials have been increasingly studied as alternatives to animal proteins, motivated in part by sustainability considerations [14,28]. Soy protein isolate is the most extensively studied plant protein for 3DFP. SPI gels formulated with XG (0.5 g per 30 g SPI) and NaCl (1 g/100 mL) showed optimal printing precision, with LF-NMR parameters strongly correlating with the rheological properties that determine printability [74]. Temperature modulation provides a practical processing lever: at 35–45 °C, gelatin addition reduced SPI paste viscosity and yield stress for smooth extrusion, while post-print cooling induced a dense protein–gelatin network for structural integrity

ACCEPTED PAPER

[76]. Combining 70 W microwave irradiation with salt addition substantially increased viscosity and elastic modulus in an SPI–strawberry system, yielding the highest shape accuracy without additional ingredients [77]. In emulsion-based systems, guar gum (0.5 %) modification of SPI emulsion gels produced low dimensional error and a smooth surface finish, whereas XG produced higher gel strength at the cost of reduced network flexibility [78]. SPI has also served as a 4D printing platform: a κ-carrageenan (3 %) SPI formulation generated four novel flavour compounds upon microwave heating, including 1-Octen-3-ol and Eugenol [16], and soy protein combined with wheat gluten and thermosensitive cocoa butter produced a fibrous microstructure analogous to skeletal muscle upon cooling — demonstrating feasibility as a plant-based meat analogue [79] (Fig. 5(a,c)).

Pea protein has been investigated as an alternative to soy. Pea-protein–alginate blends (80:20) produced optimal viscosity and print-supporting capacity, with ALM simulation indicating that 0.68 mm deposit thickness minimised residual stress in complex geometries [46]. A systematic macronutrient-composition study showed that protein content is the primary driver of extrusion force, while insoluble fibre reduces it; water-holding-capacity (WHC)-based water normalisation enabled approximately 71 % of tested formulations to print successfully to 50 mm height [47]. Pea-protein–pectin–EGCG Pickering emulsions (PEs) encapsulating cinnamaldehyde maintained cinnamaldehyde loss within roughly 10–11 % across the emulsion types (PEs and high-internal-phase Pickering emulsions, HIPPEs) during extrusion (10.0 % and 11.3 %, respectively) [80], and 15 % pea-protein isolate addition to banana paste suppressed tailing defects by reducing structural recovery rate and elongation at break [81].

3.3 Carbohydrate-Based Materials

Carbohydrate-based materials constitute the most diverse category explored for extrusion-based 3D printing [14,29]. Their printability depends primarily on the starch gelatinisation state, hydrocolloid molecular architecture, and interactions with the aqueous phase. Unlike protein gels, carbohydrate systems rarely show spontaneous gelation at ambient temperature, and thermal processing is consequently the primary rheological tuning lever.

Rice flour-based systems have been characterised extensively as clean-label printable materials. Box–Behnken design optimisation of a rice-flour–jaggery paste identified 1.5 mm nozzle diameter, 29 % layer height, 0.75 mm path width, and 20 mm/s speed as the optimal four-parameter combination [39], while a specific formulation ratio rice-flour : jaggery : water ratio of roughly 2.6 : 1 : 3.5 (86.0 g rice flour, 33.0 g jaggery, 114.9 g water) achieved high printability without hydrocolloid additives [40]. Rice variety also influenced printability through differences in amylose:amylopectin ratio: glutinous rice produced the highest print accuracy but collapsed during steaming, whereas indica and non-glutinous rice maintained structural integrity and higher resistant-starch content [85]. Sodium-alginate addition (0.50 %) further enhanced shear-thinning, viscosity, and mechanical strength across all three varieties, with non-glutinous rice performing best [84]. The same hydrocolloid-modulation strategy has been extended to brown-rice gel systems, in which sodium-alginate, xanthan, and κ-carrageenan addition shifted printability into the operating window otherwise inaccessible to plain brown-rice gel [87].

Physical modification of starches is a productive route to improving printability. Radio-frequency (RF) treatment (20 min) of potato starch reduced amylose content and gelatinisation temperature, facilitating extrusion while maintaining shape retention [93]; complementary structural characterisation of hot-extrusion-induced potato-starch reorganisation has been reported as a foundational rheological study for high-temperature starch-printing systems [90]. Pulsed electric field (PEF) treatment of wheat starch (25 kV/cm, 50 kJ/kg) introduced surface fractures on granules, reduced viscosity, and hardened the gel [91], while dry heat treatment (DHT) of cassava starch (4 h) produced the hardest gel across all gelatinisation temperatures despite reduced peak viscosity [92]. Combined application of $CaCl_2$ (1 %) and microwave irradiation (30 s) to buckwheat-starch–pectin gels induced starch–pectin crosslinking while reducing flow stress, outperforming 30-min steaming in printability [88]. Microwave pretreatment of cookie dough induced partial gelatinisation and moisture redistribution, with LF-NMR parameters predicting rheological properties

ACCEPTED PAPER

at $R^2 > 0.9$ via partial least-squares regression [82], and ultrasound-assisted microwave heating (UMCH) pretreatment (80 W) of wheat starch–papaya maintained ≥ 97 % dimensional accuracy after 20 min [89].

CFD simulation has been applied as a pre-screening tool: Bird–Carreau modelling of five cereal-grain gels reproduced the experimentally observed print-difficulty rankings [53], and power-law fluid simulation indicated that a low-flow-index, strongly shear-thinning envelope is workable for starch-based gel printing [55] (see Section 4.1 for cross-material optimisation treatment). Camera-based morphological analysis additionally quantified over- and under-extrusion and gluten-induced lateral-pull defects in real time [86], illustrating how computer-vision feedback can complement formulation-stage screening (see Section 4.3 for cross-material treatment).

3.4 Fruit, Vegetable, and Mushroom-Based Materials

Fruits, vegetables, and mushrooms are intrinsically challenging for extrusion-based printing because of high moisture content, low structural biopolymer concentration, and limited native yield stress for self-supporting deposition [14]. Research has focused on hydrocolloid addition, processing-condition optimisation, and internal structural design to achieve adequate printability while preserving nutritional and sensory quality.

Potato-based systems have been most thoroughly explored, with the internal structure identified as a key texture-engineering lever: lower infill level increased porosity and reduced hardness and fracturability after air frying, while keeping oil content below 17 % [50]. Microwave-induced over-puffing in potato gel was controlled by soybean insoluble dietary fibre (SIDF), which moderated the moisture-evaporation rate and reinforced the gel network [51]. The post-print drying method also affected quality in rose-yam paste: microwave vacuum drying (MVD) reduced processing time by 84 % compared with freeze-drying while delivering comparable sensory outcomes [95]. Among fruit and vegetable materials, carrot-pulp printability improved markedly with finer particle size, with concomitant increases in apparent viscosity, cohesiveness, and carotenoid bioavailability [97]. Beyond mainstream substrates, novel routes such as plant-callus-based 3D printing — exemplified by carrot-callus tissues as a candidate substrate for low-input innovative food production [98] — and ultrasonic-treatment / homogenisation pre-processing for ink-property tuning [106] illustrate the breadth of substrate possibilities currently being explored within the Section 3.4 category.

Mushroom-based materials offer high nutritional density but generally require hydrocolloid supplementation for printing. Button-mushroom flour (20 %) blended with wheat flour reached 78.13 % dimensional accuracy under optimised conditions [100]. For dysphagia applications, XG (0.9 %) in black-fungus formulations reached IDDSI level 5 classification [101]; XG and κ-carrageenan in shiitake mushroom provided self-supporting capacity and IDDSI level 5 compliance [102]; and a substrate-adaptive hydrocolloid strategy for fresh vegetables — ranging from no additive (peas) to binary XG–LBG (bok choy) — supported IDDSI-compliant printing across multiple vegetable types [103].

3.5 Composite and Functional Materials

Composite and functional materials co-engineer structural printability with biological functionality, extending 3DFP toward bioactive delivery and by-product valorisation. High-oil systems require careful formulation management: in a canola-oil – corn-starch – WPI system (up to 37 % oil), pre-storage at 4 °C for 24 h increased G' and viscosity through cold-induced network strengthening [104], while beeswax oleogel (20 %) in a potato-starch–protein system reached a favourable softness–accuracy balance at 30 °C and 40 mm/s [96].

By-product valorisation has yielded functional printing substrates. Spirulina platensis residues converted into inks through heat pretreatment and 25 % moisture adjustment showed well-defined shear-thinning and post-print shape

ACCEPTED PAPER

retention [105]. Okara produced a printable ink with well-defined yield stress and storage modulus without additives [107] (Fig. 5(b,d)).

For probiotic delivery, Bifidobacterium animalis BB-12 incorporated into mashed potato remained viable through refrigerated storage, with only minor loss at the narrowest nozzle tested [108]. Encapsulation markedly improved protection: alginate–gelatin-encapsulated B. lactis exceeded 10^9 CFU/g post-printing and showed 8-week room-temperature stability [109], and spray–freeze-drying (SFD)-encapsulated L. plantarum reached 79 % in vitro survival and 96–98 % stability over 35 days [110]. Arthrospira platensis extracts encapsulated in alginate microbeads maintained higher antioxidant activity and colour stability for 30 days in printed cookies [111], suggesting that encapsulation prior to printing offers more consistent bioactive protection than relying on the food matrix alone.

Across the five substrate categories surveyed in this section, printability has been pursued through a recurring set of strategies — network reinforcement (hydrocolloid or enzymatic crosslinking), thermal or mechanical pretreatment of the matrix, particle-size and moisture optimisation, and structural design through coaxial or multi-material extrusion. The choice among these strategies is governed by the specific deficit of each substrate relative to the rheological window discussed in Section 2.3. The following section turns from substrate-specific formulation to the cross-material data-driven and in-situ methods used to optimise and monitor the printing process itself.

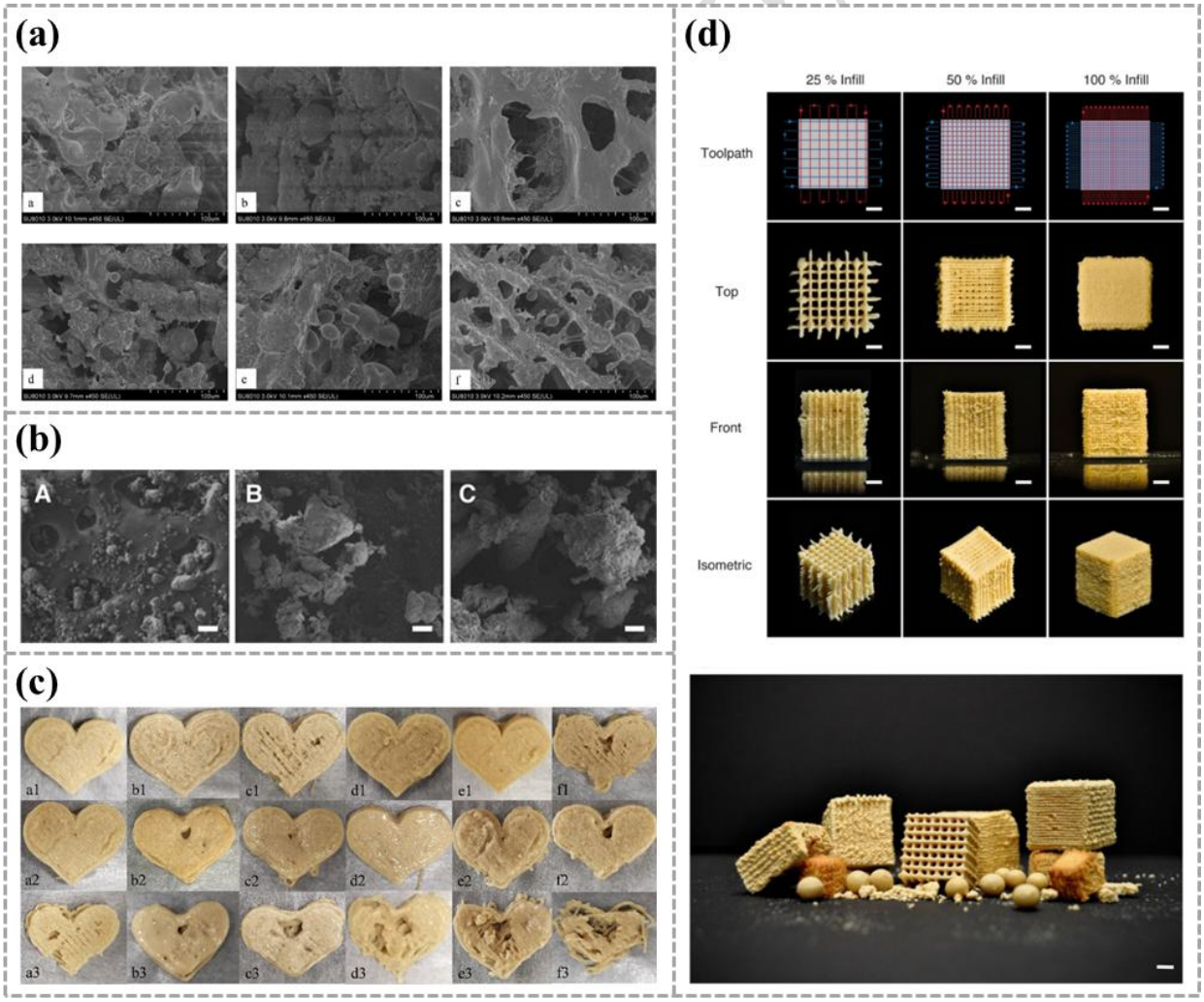


Fig. 5. Printability strategies across food substrate categories in extrusion-based 3D food printing. (a) SEM

micrographs of soy protein–gluten gel showing fibrous microarchitecture. [79] (b) SEM images of okara particles at <100 μm particle size [107]. (c) Printing formability of soy protein–gluten doughs at 45 °C across multiple formulations. [79] (d) Freeze-dried okara snacks fabricated at 25, 50, and 100 % infill density [107]. Panels (a,c) reprinted with permission from Wang et al. [79] Copyright © 2021 American Chemical Society. Panels (b,d) reprinted with permission from Lee et al. [107] Copyright © 2021 American Chemical Society.

ACCEPTED PAPER

4. Intelligent Process Control: Optimisation, AI, and Real-Time Closed-Loop

The four engineering layers reviewed in Section 2 frame what an ink can do, and Section 3 surveys how each substrate category navigates that design space. Building on these design-space and substrate considerations, the next engineering layer — and a recurring framing of recent 3DFP research — is the cross-material framework by which optimisation strategies, AI-based predictive models, and real-time process control are integrated to move printability from a trial-and-error practice toward a more predictable and partially automated operation [7,13,57]. This section organises that integration along four axes. The discussion begins in Section 4.1 with cross-material optimisation, examining both statistical design of experiments and computational simulation as routes to pre-experimental ink screening. Section 4.2 then surveys AI/ML-based printability prediction across the food MEX literature, with input modalities, target functions, and architectural choices benchmarked in Table 3. Section 4.3 subsequently turns to real-time computer-vision feedback, contrasting classical morphological analysis with deep-learning vision systems. Lastly, Section 4.4 reviews the integrated closed-loop architectures in which these three axes operate as components of a coherent intelligent-3DFP system. Fig. 6 summarises the four axes that organise the discussion below.

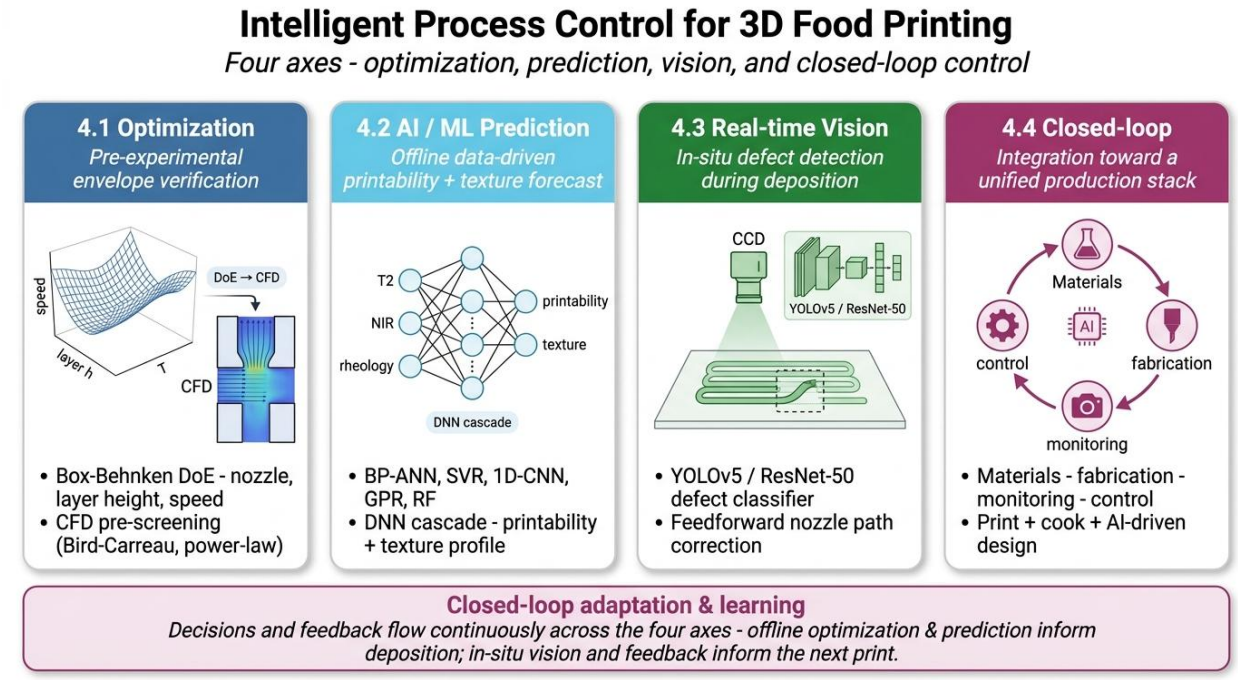


Fig. 6. Four axes of intelligent process control in extrusion-based 3D food printing: pre-experimental optimisation (Section 4.1), offline AI/ML-based printability and texture prediction (Section 4.2), real-time vision-based defect detection (Section 4.3), and integrated closed-loop architecture (Section 4.4).

4.1 Cross-Material Optimisation Strategies

Cross-material optimisation in extrusion-based 3DFP has progressed along two complementary routes: statistical design of experiments (DoE) for systematic process-parameter mapping, and computational fluid dynamics simulation for pre-experimental ink screening. This subsection reviews both routes, examining how methodologies originally developed for individual substrates in Section 3 have been generalised across food matrices.

Statistical DoE provides a formal framework for mapping the response of a printable construct to multiple process parameters within a bounded experimental window, replacing one-factor-at-a-time trials with a structured factorial

design that quantifies both main effects and interactions. Among DoE, Box–Behnken response surface design has emerged as the most widely adopted route in food MEX, valued for its three-level design that captures non-linear responses with fewer experimental runs than a full factorial. Applied to a rice-flour–jaggery system, Box–Behnken optimisation identified 1.5 mm nozzle diameter, 29 % layer height, 0.75 mm path width, and 20 mm/s print speed as the optimal four-parameter combination across an experimentally bounded operating window [39]. The same methodology has been transferred to numerous substrates throughout Section 3, with the optimisation endpoint matched to each material's intrinsic constraint — moisture-driven retrogradation in starch systems, gel-network density in protein systems, and particle-size distribution in fibre-rich systems. Whereas DoE-based parameter mapping anchors optimisation in experimental factorial designs, computational simulation provides a complementary optimisation route that bypasses the experimental cost of factorial designs. CFD using the Bird–Carreau viscosity model has reproduced the relative printability ranking of five cereal-grain pastes (buckwheat, brown rice, mung bean, Job's tear, black rice) ahead of any printing trial [53], while POLYFLOW-based finite-element simulation of rice-starch / peanut-protein-isolate composites resolved both the in-nozzle pressure distribution and the post-extrusion deformation modes [54]. Power-law fluid CFD using POLYFLOW suggested that a low flow-index, strongly shear-thinning envelope is workable for extrusion-based 3D printing of starch-type ink matrices [55]. Furthermore, an additive-layer-manufacturing finite-element simulation of pea-protein–alginate (80:20) blends was used to evaluate residual-stress distribution across the printed sample, comparing a baseline deposit thickness against simulated alternatives to identify the configuration that minimises stress accumulation in complex post-print geometries [46]. More recently, integrated computer-simulation – extrusion-force analysis has been proposed as a rapid pre-screening tool that combines numerical flow simulation with experimentally measured extrusion force, providing a quantitative criterion for ink screening before experimental ink is consumed [112].

Despite these advances, several limitations persist in cross-material optimisation: (1) DoE-based parameter mapping is typically validated within single substrate families, limiting direct transfer of optimal parameter sets across material classes; (2) CFD simulations require accurate constitutive parameters that are not always available for compositionally complex food matrices; and (3) experimental verification of computational predictions remains substrate-specific. Both routes nonetheless share the common objective of verifying a printable operating envelope before experimental ink is consumed, and their cross-material application has matured into a coherent pre-screening discipline in food MEX, providing the natural setup for the data-driven prediction frameworks reviewed in Section 4.2.

4.2 Cross-Material AI/ML Frameworks

Whereas Section 4.1 uses physics-based simulation to verify a printable operating envelope, AI/ML-based prediction circumvents the requirement for known constitutive parameters by learning the composition–rheology–printability mapping directly from multi-substrate datasets [57]. A range of architectural families has been benchmarked across food MEX studies for this purpose, from ensemble decision trees and kernel-based regression to deep neural network cascades [45,56–60,113–118]. The benchmarking objective in each case is to identify which combination of input modality (image, rheology, LF-NMR, near-infrared spectroscopy (NIR)) and architectural class best predicts a target endpoint — binary printability, continuous spreading ratio, or multi-target texture profile. Table 3 consolidates these architectures alongside their input streams, target functions, and reported quantitative performance, providing a side-by-side reference against which the subsequent paragraphs are organised.

Random forest classification trained on image-based features has reached the printability of low-methoxyl pectin / cellulose-nanocrystal / $CaCl_2$ composite hydrogel inks at 82–88 % accuracy (Table 3, Row 1), indicating that ensemble decision-tree models can map composition–rheology–printability relationships without explicit constitutive equations [117]. The same algorithmic family applied to a multi-substrate framework combining measured features with data-driven inference (a "gray-box" approach) — sodium caseinate, cheese slices and sauces, chocolate–coconut-

ACCEPTED PAPER

oil pastes — has extended image-analysis-based prediction to extrudability and extrusion stability with moderate-to-high accuracy across heterogeneous food systems [114]. An Extra Trees Regressor trained on rheological and printing-parameter features of low-methoxyl pectin – porcine-gelatin blends achieved post-extrusion filament-spreading-ratio prediction with $R^2 \approx 0.94–0.98$, with viscoelastic parameters accounting for over 90 % of the prediction importance, providing a regression-based route to dimensional control that complements the binary classification target [60]. Beyond ensemble methods, Gaussian Process Regression applied to pregelatinised corn starch under varying starch concentration and printing temperature reported prediction errors as low as 0.01–0.48 % root-mean-square error (RMSE), offering an alternative kernel-based regression route particularly suited to small-sample, high-dimensional formulation spaces [116].

Beyond ensemble methods, back-propagation artificial neural networks coupled with low-field nuclear magnetic resonance inputs constitute the most extensively reported AI axis in food MEX, as evident from Rows 5–9 of Table 3. Trained on T_2 relaxation-time distributions of free, immobilised, and bound water, BP-ANN models for polysaccharide hydrogel systems (gellan, locust-bean, xanthan, pectin, tara gums) attained discrete printability scoring with $R^2 \approx 0.98$, with free-water T_2 identified as the primary discriminating variable [58]. The same LF-NMR-based predictive framework extended to surimi–starch systems generated polynomial regression models that predicted printing accuracy at $R^2 = 0.88$ and printing stability at $R^2 = 0.93$ [45], and its further application to corn-starch ink under varying gelatinisation temperatures — using a BP-ANN model — delivered $R^2_{adj} = 0.894$ across a representative starch-concentration window [59]. The mashed-potato system [56] and the surimi gel + dielectric-loss-factor *p*airing [57] further support the LF-NMR axis as a frequently used route for non-destructive printability prediction in hydrocolloid-rich substrates.

The most recent advance in this axis is a multi-stage Deep Neural Network cascade [115]. Built on 12 input features extracted from starch-granule multi-structure, gel formulation, and gel rheology, the cascade comprises three specialised models in series — a binary printability classifier, a multi-class printability rating classifier, and a textural property regressor predicting hardness, springiness, gumminess, and cohesiveness simultaneously. Validated on 88 corn-starch / sodium-alginate samples spanning multiple maize-starch types, the cascade reached 88.9 %, 86.7 %, and 90.4 % accuracy on the three respective tasks. The cascade marks a methodological shift in the AI axis: textural attributes that previously required physical printing and instrumented texture analysis are predicted from formulation data alone, broadening pre-print evaluation from a single-target classifier toward a multi-target predictive operation [115]. More recent research has begun to couple these predictive models with physics-based simulation and formulation-search algorithms, moving the axis from prediction toward integrated optimisation. A modified two-dimensional axisymmetric CFD model of surimi extrusion was paired with a partial-least-squares-regression model trained on texture data to predict the required extrusion pressure and hence printability ($R^2 > 0.95$), linking the physics-based route of Section 4.1 with data-driven prediction in a single workflow [119]. On the formulation side, random-forest and Bayesian-tuned multilayer-perceptron models predicted the shear-thinning viscosity of six candidate hydrocolloids for plant-based meat analogues with high fidelity ($R^2 \approx 0.99$), and the predicted viscosities tracked the measured textural attributes of the corresponding analogues [120]. Moving from prediction to closed-loop optimisation, an end-to-end framework coupling a multimodal artificial neural network — processing both 3D-scan-derived geometric deviation and compositional inputs — with a genetic-algorithm search has been demonstrated to recommend optimal ink formulations for direct-ink-writing 3DFP with minimal experimental iteration [121]. Together, these studies mark a shift from single-target printability classifiers toward simulation-integrated, optimisation-oriented ML pipelines.

Comparative ML benchmarking has applied multiple algorithmic families — support-vector regression, BP-ANN, and convolutional neural networks — to LF-NMR / dielectric input streams of polysaccharide gels, supporting indirect rheology and printability prediction across substrate categories [57,60]. Despite this rapid progress, three challenges persist across the food MEX AI/ML landscape: (1) model robustness is constrained by the natural variability of food

ACCEPTED PAPER

substrates — moisture content, molecular structure, particle size, and storage condition; (2) data-ownership restrictions limit cross-institutional sharing of training datasets; and (3) standardised data-collection protocols across substrate families are largely absent [57]. A further constraint follows from the optimisation-oriented frameworks noted above: simulation- and search-coupled pipelines [119,121] still depend on an experimentally validated objective function, so their gains remain tied to the formulation on which each model was trained. This lack of standardisation has a direct downstream effect: the models compiled in Table 3 are largely trained on laboratory-specific datasets and transfer poorly across them. Federated learning, open-access rheological and sensory repositories, and certified external benchmarks have been proposed as operational responses to these constraints [57], although their adoption remains an active rather than completed research direction. Resolving these challenges will determine the pace at which AI/ML moves from a supplementary predictor toward a substrate-agnostic decision layer in intelligent food printing.

Table 3. Cross-material AI/ML architectures applied to extrusion-based 3D food printing: input modality, target function, and reported quantitative performance.

AI Model	Input Features	Target Function	Reported Metric	Ref.
Random Forest	Image-derived geometric features of LMP / cellulose-nanocrystal / $CaCl_2$ hydrogel inks	Binary printability classification	Accuracy 0.74–0.82	[117]
Random Forest	Image features of complex food matrices (sodium caseinate, cheese, chocolate–coconut-oil pastes)	Extrudability and extrusion-stability prediction	Moderate-to-high accuracy	[114]
Extra Trees Regressor	Four rheological + printing-parameter features of LMP–porcine-gelatin blends	Post-extrusion filament spreading-ratio prediction	R^2 = 0.9441–0.9775	[60]
Gaussian Process Regression (GPR)	Pregelatinised corn-starch composition + printing temperature	Continuous printability prediction	RMSE 0.013–0.48 %	[116]
BP-ANN coupled with LF-NMR	T_2 relaxation-time distribution of polysaccharide hydrogel inks	Discrete printability scoring	R^2 = 0.951–0.999	[58]
LF-NMR + polynomial regression	T_2(MP) and A_{22} from surimi–starch matrices	Printing accuracy + stability prediction	R^2 = 0.88; R^2 = 0.93	[45]
BP-ANN	Gelatinisation-temperature × starch-concentration grid	Printability classification	R^2_{adj} = 0.894	[59]
LF-NMR	T_2 distribution of mashed-potato inks	Indirect printability prediction	Strong correlation	[56]
LF-NMR	Coupled T_2 and ε'' of surimi gels	Coupled rheological + dielectric observable; cross-reference to Section 5/Section 6	Strong correlation	[57]

ACCEPTED PAPER

Multi-stage DNN cascade	12 features: starch-granule multi-structure + gel formulation + gel rheology	Binary printability → rating (high/moderate/low) → textural properties (HD, SG, GM, CS)	88.9 % / 86.7 % / 90.4 %	[115]
Comparative ML benchmark	NIR + LF-NMR streams across polysaccharide families	Polysaccharide-gel rheology prediction	R^2 = 0.9796; RPD = 7.07	[118]
PLSR + modified 2D-axisymmetric CFD	Texture-profile data of surimi inks	Required extrusion pressure / printability	*$R^2 > 0.95$*	[119]
Random Forest / Bayesian-tuned MLP	Composition, shear rate, temperature of six hydrocolloids	Shear-thinning viscosity (→ texture correlate)	*$R^2 = 0.994–0.996$; RMSE 0.055–0.071*	[120]
Multimodal ANN + genetic algorithm	3D-scan geometric deviation + compositional data (DIW inks)	Printing-quality optimisation (total-deviation metric)	*Good predicted–measured agreement*	[121]

4.3 Real-Time Computer-Vision Feedback

In contrast to Section 4.1 and Section 4.2, which operate on the ink formulation before printing begins, real-time computer vision provides the in-situ feedback loop that detects defects during deposition and adjusts process parameters within the printing horizon. This subsection begins with classical morphological analysis of deposited filaments for direct dimensional and defect quantification, and then turns to deep-learning vision systems that have enabled high-accuracy defect classification at production-relevant rates.

Camera-based morphological analysis of starch-based deposited filaments has resolved over- and under-extrusion and gluten-induced lateral-pull defects in real time, with the same image stream concurrently quantifying dimensional accuracy at strand and layer scales [86]. Quantitative layer-extrusion accuracy contextualised against human-rater evaluation was formalised in a CRFS framework [122], and image-based feedforward nozzle-motion control demonstrated that print quality can be improved by adjusting the nozzle path during printing on the basis of vision-derived deviation signals rather than after-print inspection alone [123].

Beyond classical morphological analysis, deep-learning vision systems represent the most recent advance in this axis. Convolutional neural networks (CNNs) have been compared across multiple architectures (Faster R-CNN, YOLOv5, ResNet50) for real-time defect classification of 3D-printed food constructs, revealing that deep-learning–based vision pipelines can match the dimensional-accuracy quantification of classical morphological analysis while reducing operator dependence [113]. The same vision-based feedback principle has been integrated with simultaneous post-deposition processing in a recent platform that combines extrusion-based 3D printing with laser-induced graphene (LIG) infrared heating and generative-AI-assisted design [124], indicating that smart additive manufacturing for food can be deployed at production-relevant rates. These vision-based systems share a common architecture — a downward-facing camera mounted on or near the print head, real-time image acquisition synchronised to the deposition stage, and a CNN-class model that maps the acquired image stream to a defect classification or to a feedforward parameter adjustment signal. Together, the classical and deep-learning vision strands provide the in-situ feedback channel required to close the loop between offline prediction (Sections 4.1–4.2) and real-time deposition. These vision-based loops, however, act reactively and on kinematic actuators alone: upon detecting a defect they can adjust print speed or extrusion pressure, re-path the nozzle, or halt the build, but they cannot alter the intrinsic rheology or chemical crosslinking of the ink already within the nozzle. True proactive endpoint control — in-situ modulation

ACCEPTED PAPER

of the ink's material state during deposition — remains a hardware and chemical-engineering bottleneck rather than a demonstrated capability. This closure is examined as an integrated architecture in Section 4.4.

4.4 Integrated Closed-Loop Architectures

The integration of cross-material optimisation (Section 4.1), AI/ML-based prediction (Section 4.2), and real-time computer vision (Section 4.3) into a single closed-loop architecture is the synthesis target of recent intelligent-3DFP research. This subsection reviews the conceptual framework underlying this integration, a recent production-ready three-axis demonstration, and the regulatory landscape that frames the field's transition from academic study toward commercial deployment. Fig. 7 illustrates the four sequential modules of such a closed-loop architecture and contrasts classical PID-based control with deep-learning-based adaptive control.

At the conceptual level, a four-module framework comprising materials, fabrication, monitoring, and control has been proposed as the architectural skeleton on which AI-driven predictive modelling, real-time vision, and feedforward parameter adjustment can be integrated end-to-end [38]. This framework is aligned with the AI-AM (artificial-intelligence-driven additive manufacturing) paradigm, in which AI provides the optimisation, prediction, and adjustment layer that ties the four modules into a single closed-loop system [57]. Distributed implementations of this monitoring layer — in which networked AM platforms broadcast in-line defect-detection results to a remote analytics back-end — have been characterised as a route to reducing material wastage at scale [125], and provide an operational template for remote, real-time quality assurance in distributed 3DFP networks.

Beyond conceptual integration, a production-ready three-axis integration has recently been reported [124]. The platform combines extrusion-based 3D printing, simultaneous laser-induced graphene infrared heating at the deposition site, and generative AI design — a three-axis integration that demonstrates the closed-loop concept in a single hardware-software stack. The implication is that the offline rheological framework of Section 2.3, the material-specific predictive frameworks distributed across Section 3, the cross-material AI/ML layer of Section 4.2, and the real-time vision layer of Section 4.3 are increasingly operating as components of a coherent intelligent-3DFP system rather than as independent research streams. Industrial implementations by Cocuus, Revo Foods, and Steakholder Foods illustrate how automated process control and advanced material structuring translate laboratory-scale principles toward scalable production [57], and patent activity in AI-enabled food printing — covering algorithmic process control, scheduling-based fabrication, and personalised formulation manufacturing — has accelerated in 2022–2025 [57], indicating a broader transition from academic optimisation studies toward commercial deployment. Even so, the closed loop realised in these systems remains a kinematic one: current architectures regulate deposition geometry through process-parameter feedback, whereas closed-loop control over the ink's evolving material state — the level required for fully autonomous, defect-free operation — has not yet been demonstrated.

Across the four axes reviewed in this section — cross-material optimisation, AI/ML-based prediction, real-time computer-vision feedback, and integrated closed-loop architectures — intelligent process control has progressed from a collection of substrate-specific demonstrations toward a more coherent, partly automated framework for food MEX. Addressing the remaining gaps — substrate-agnostic optimisation databases, federated AI/ML training, robust real-time vision under industrial throughput, and harmonised regulatory documentation — will determine the pace at which intelligent food printing moves from laboratory demonstration toward certified industrial deployment. These intelligent-control axes regulate the deposition stage itself; once the deposited construct has been formed, the engineering attention shifts to fixing its geometry, texture, and nutritional profile through the post-processing operations examined next in Section 5.

ACCEPTED PAPER

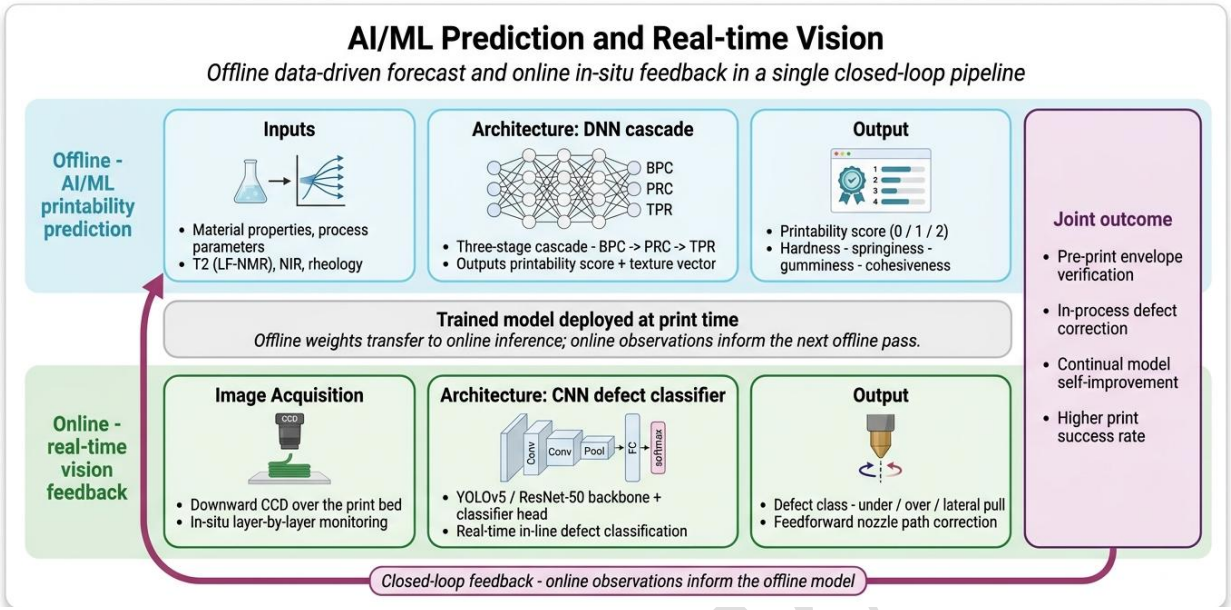


Fig. 7. Closed-loop intelligent process control pipeline. The offline AI/ML printability prediction stage (top) and the online real-time CNN-based vision feedback stage (bottom) form a single architecture in which online observations retrain the offline model at the next print cycle.

5. Post-Processing of Extrusion-Based 3D Printed Foods

In this section, a critical review of post-processing in extrusion-based 3DFP is presented, emphasizing its pivotal role as the engineering stage at which the deposited construct is converted from a metastable state into a finished product with defined geometry, texture, and nutritional profile. This review connects directly to the intelligent process-control framework of Section 4, which acts on the printing stage itself; once deposition is complete, the deposited construct enters the post-processing stage examined here. Immediately after deposition, printed hydrogels and biopolymer matrices exist in a thermodynamically and rheologically metastable state, supported only by their zero-shear viscosity and transient yield stress (τ_y) against gravity-induced collapse [48,49]. Post-processing therefore serves three coupled purposes: (i) fixing dimensional shape stability through physical–chemical phase transitions, (ii) tuning the microstructural texture, and (iii) shaping the nutritional profile of the final construct. The integrated evaluation framework recently proposed by Tan and Ng — coupling printability, rheology, instrumental texture, and quantitative nutritional retention within a single experimental pipeline — illustrates that a method securing shape fidelity at the cost of bioactive degradation or amino-acid loss should not be regarded as a successful design choice [126].

As illustrated in Fig. 8, post-processing modalities can be organised along three thermodynamic axes — surface-driven thermal, volumetric and electromagnetic, and non-thermal and emerging — each of which defines a distinct trade-off between structural fixation, textural development, and nutritional retention. This section organises post-processing modalities along their thermodynamic trajectory: Section 5.1 reviews surface-driven thermal modes — deep-fat frying, air-frying, baking, and steaming — and the texture and nutritional trade-offs each imposes; Section 5.2 turns to volumetric and electromagnetic modes, in particular microwave dielectric heating, which provide component-selective absorption and form the bridge to the stimulus-responsive transformations examined in Section 6; Section 5.3 considers non-thermal and emerging mechanical modalities — freeze-drying, microwave vacuum drying, cold plasma, ultrasound, and high-pressure processing — that aim to bypass thermal stress entirely; and Section 5.4 proposes a unified quality-control framework assembled from established food-science standards (Codex;

ACCEPTED F

Association of Official Analytical Chemists, AOAC; ISO; IDDSI; International network for in vitro digestion harmonisation, INFOGEST), with risk-tiered release specifications and process-analytical-technology recommendations matched to each modality.

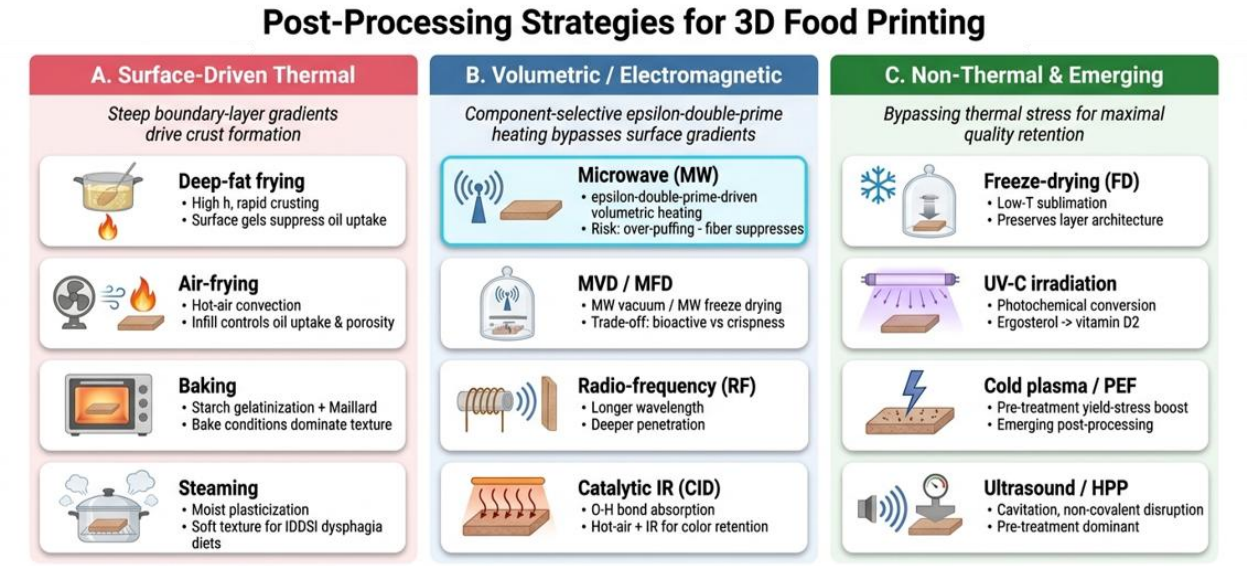


Fig. 8. Post-processing strategies for extrusion-based 3D food printing, organised along three thermodynamic axes: surface-driven thermal modes; volumetric and electromagnetic modes and non-thermal and emerging modes.

5.1 Surface-Driven Thermal Post-Processing

Surface-driven thermal modes fix the structure of the printed matrix through steep thermal gradients established at the boundary layer, with both the textural architecture and the nutritional integrity of the construct determined by the heat- and mass-transfer characteristics of each mode. A comparative reading of deep-fat frying, air-frying, baking, and steaming reveals distinct thermomechanical trade-offs.

Deep-fat frying drives a high convective heat-transfer coefficient at the surface, producing rapid moisture evaporation and the formation of a dehydrated outer crust. The associated crusting confers strong shape retention and a porous, brittle fracture profile (crispness) on starch- and protein-based constructs. Quantitative oil-uptake control has been characterised in plant-based meat analogues where deep-fat frying at 180 °C for 90 s produced dimensional stability of 91.2–98.6 % and cooking loss of 5.7–14.2 %, with xanthan and HPMC forming a surface gel layer that reduced lipid uptake [127]. Sequential post-processing combining hot-air drying with subsequent deep frying has been reported for printed chicken-meat constructs, producing crispy nuggets with a product-level energy value of 166.7 ± 0.1 kcal/100 g — one of the few studies to translate extrusion-printing parameters into a complete nutritional-label specification at the finished-product level [66]. Nutritionally, deep-frying elevates the lipid profile through oil incorporation and accelerates Maillard-derived hazards while degrading thermolabile antioxidants — a trade-off that air-frying reduces substantially.

Air-frying uses high-velocity hot air to approximate the dehydration kinetics of deep-frying without lipid immersion. In 3D-printed potato snacks, lower infill level acts as a texture-engineering lever: it enlarges the internal void fraction, reduces post-fry hardness and fracturability, and limits oil uptake to below 17 %, supporting a single construct with multiple textural zones and a more favourable lipid profile than deep-fried equivalents [50]. Compositional modification offers a complementary route: incorporation of potato processing by-products into yam

ACCEPTED

flour at a 7 : 3 ratio raised G' and water-absorption index in the green construct, while a parallel infill pattern reduced post-fry deformation [94]. In both cases, the geometry transmitted by printing — rather than the post-processing operation itself — provides the primary structural defence against surface-driven shrinkage.

Baking operates on a slower timescale through isotropic structural setting via starch gelatinisation and protein denaturation, producing an aerated dry matrix in which Maillard browning and biopolymer rearrangement together determine final texture. The dominance of post-processing variables over printing variables in this regime has been most directly resolved in carrot-purée-based dough constructs, where a response-surface design varying nozzle diameter, filling rate, baking time and baking temperature showed that baking parameters exert the major influence on crust strength, mean force, and total pore area, while printing parameters exert only secondary influence — supporting the view that post-processing is the primary texture-determination axis once printability has been secured [128]. Compositional modification can further redirect the chemistry of baking toward enzymatic-browning suppression: dough acidity adjustment combined with pre-processed bran moderates the reaction kinetics of polyphenol oxidase without compromising the spatial resolution of the printed layers [83]. The same compositional axis can be used to upgrade nutritional profile within the baking step itself; in cereal-based snacks fortified with ground larvae of Tenebrio molitor up to 20 g/100 g (d.b.), 3D printing followed by baking simultaneously elevated total essential amino-acid content, protein digestibility, and the corrected amino-acid score, indicating that baking can be combined with deliberate nutritional fortification when the ink composition is selected accordingly [129]. In cowpea-sourdough / quinoa-malt biscuits, 3D-printed samples showed greater cell elongation and altered Maillard development relative to traditional biscuits, attributable to in-barrel shearing modifications of biopolymer organisation that affect the bioavailability of Maillard-derived compounds [130]. In pea-protein / pea-starch baked snacks, dry-matter content was the main determinant of Young's modulus across composition variables, indicating that baking conditions outweighed ink-composition adjustments in determining final texture and dry-matter-linked nutrient density [131].

Steaming, a wet-heat mode, plasticises the biopolymer network through moisture infusion. It produces excellent shape fidelity and a softer, easily masticated texture suitable for dysphagia diets — confirmed in omega-3-fortified surimi gels at 485.6 ± 0.6 g hardness (IDDSI Level 5) [132] — but lacks the mechanical rigidity required for complex, self-supporting architectures.

Recent comparative-cooking studies provide a quantitative basis for selecting among the four surface-driven modes on a single substrate. Pan et al. demonstrated on shrimp-surimi prints that oven-baking and microwaving best preserved geometry while steaming and boiling caused water-uptake-driven swelling [133]. A direct baking-versus-steaming comparison of pearl-millet / banana-pulp blends further showed that steamed constructs had higher water activity and softer texture while baked counterparts achieved greater dry-matter content and firmer mouthfeel [134]. Together with Gautam et al. IDDSI-graded omega-3 surimi quantification [132] and Venkatachalam et al. pea-protein / pea-starch comparison [131], these studies provide a quantitative basis on which to select among surface-driven modes for a given printed substrate.

Despite the maturity of these four surface-driven modes, three challenges remain in their application to extrusion-based 3DFP: (1) the trade-off between dimensional stability and bioactive retention has not been systematically quantified across substrate classes, with frying maximising shape retention at the cost of lipid uptake and Maillard hazards while steaming preserves bioactives at the cost of structural rigidity, a trade-off that is moreover rarely accompanied by consumer sensory or palatability evaluation in the printed-food literature; (2) the coupling between printing parameters (infill pattern, layer height) and surface-driven post-processing outcomes remains substrate-specific, limiting the development of generalisable design rules; and (3) the nutritional-label translation of printing-and-cooking parameters into finished-product composition has been reported in only a small subset of studies [66], leaving most published work at the demonstration rather than the deliverable stage. Resolving these challenges would extend surface-driven post-processing from a finishing operation to a primary engineering lever in printed-food design.

ACCEPTED PAPER

5.2 Volumetric and Electromagnetic Post-Processing

In contrast to surface-driven modes, volumetric and electromagnetic post-processing — most notably microwave dielectric heating — delivers energy directly into the bulk of the construct. MW circumvents the geometric thermal resistance inherent to bulky 3D-printed structures by converting high-frequency electromagnetic energy into volumetric heat through the frictional rotation of permanent dipoles, with volumetric power dissipation governed by $P \propto f \cdot \varepsilon'' \cdot E^2$, where f is the operating frequency, ε'' the dielectric loss factor, and E the electric-field amplitude. The operational consequence is component-selective absorption: distinct constituents within the printed matrix (free water, inorganic salts, lipid domains) have markedly different ε'' values, so MW energy is selectively partitioned into moisture- and ion-rich domains, generating a localised internal vapour pressure (ΔP) that drives volumetric puffing. Volumetric puffing in turn supports the formation of a uniform micro-porous scaffold within starch and protein gels, with concomitant effects on sensory texture and digestibility.

MW processing also introduces a characteristic failure mode: over-puffing. When the rate of vapour expansion exceeds the viscoelastic stress-relaxation limit of the polymer network, or when ΔP accumulates before complete starch gelatinisation, interlaminar adhesion fractures and bulk geometric collapse follows. Rheological intervention is consequently required to retain the porous-scaffold benefits of MW while suppressing the collapse risk. Targeted addition of soybean insoluble dietary fibre binds free water and reduces its dielectric mobility while reinforcing the mechanical tensile strength of the gel network; the result is a finely tuned, porous, crispy internal architecture rather than over-puffing collapse [51].

Beyond structural control, the rapid and uniform character of MW heating provides a nutritional advantage that distinguishes it from prolonged surface-driven modes. MW reduces overall thermal-exposure time and supports higher retention of thermolabile proteins, fibres, and vitamins than the prolonged heat exposure characteristic of conventional baking or frying — a trade-off quantified in fibre-rich indigenous-flour 3D-printed snacks, where microwave drying outperformed both hot-air-drying-followed-by-deep-frying and stand-alone deep-frying in nutrient, colour, and textural retention [135]. The dielectric-loss properties of individual ink components have additionally been characterised as design variables: NaCl raises ε'' and shortens drying time but reduces final hardness, while sucrose leaves drying time unchanged but elevates hardness, providing independent levers for texture tuning under microwave vacuum drying [136].

The MW power-density continuum further maps a quantitative texture–nutrition trade-off that should be specified during product development. In microwave freeze-drying (MFD) of chlorogenic-acid – sweet-potato-starch constructs, 0.5 W/g produced honeycomb porosity of 19.63 % with no significant difference in chlorogenic-acid content or ABTS scavenging activity from freeze-dried controls, whereas 4.0 W/g generated maximum hardness and crispness at the cost of 4.30 % greater shape distortion relative to the 0.5 W/g condition; resistant-, slowly-digestible-, and rapidly-digestible-starch fractions remained equivalent to freeze-drying (FD) across most of the operating window [137]. This power-density-dependent mapping illustrates the quantitative specification required to translate MW post-processing from a demonstration mode into a controlled engineering operation.

Beyond MW, radio-frequency **(**RF**)** and infrared (IR) heating provide complementary volumetric routes, although their application as post-processing of extrusion-printed foods remains comparatively underdeveloped. Catalytic infrared drying (CID) of curcumin–whey-protein-isolate-nanoparticle printed inks produced a more uniform colour change and higher curcumin retention than microwave and hot-air drying, while maintaining a dimensional-retention rate above 90 % [138]. This case also illustrates the convergence of volumetric post-processing with stimulus-responsive colour change, positioning dielectric- and radiation-based modes as the bridge to the 4D transformations examined in Section 6.

ACCEPTED PAPER

Despite the dual advantages of MW — bulk energy delivery and component-selective absorption — three challenges constrain its broader deployment as a controllable post-processing modality: (1) over-puffing remains the dominant failure mode under high-power conditions and is currently mitigated reactively (composition adjustment after observed collapse) rather than proactively (composition-aware power-profile design); (2) the dielectric-loss properties of multi-component food matrices are not systematically characterised, limiting the predictive design of MW-targeted compositions; and (3) real-time monitoring of in-construct ΔP and ε'' during MW exposure remains at the demonstration stage, leaving MW post-processing without the closed-loop sensing infrastructure available for surface-driven modes (Section 4.3). ; moreover, the texture gains reported under high-power MW are seldom validated against sensory acceptability, an omission examined further in Section 6. These constraints define the engineering frontier on which MW transitions from a static post-processing mode to a programmable stimulus for the 4D transformations examined in Section 6.

5.3 Non-Thermal and Emerging Mechanical Post-Processing

Because thermal phase transitions inherently risk capillary shrinkage, structural warping, and degradation of bioactive compounds, non-thermal stimuli have been pursued as engineering variables for higher quality retention. Freeze-drying is the canonical non-thermal structural-fixation mode: by freezing the printed matrix below its maximum freeze-concentration glass-transition temperature (T_g') and sublimating ice crystals under high vacuum (< 0.01 atm), FD bypasses the liquid phase entirely. The associated removal of liquid surface-tension and capillary forces preserves the layer-by-layer architecture and the engineered micro-porosity with high dimensional fidelity. Nutritionally, the cryogenic and oxygen-deprived environment limits oxidation and thermal degradation of phytochemicals, a feature that has made FD the most frequently selected mode for fruit- and vegetable-based functional foods. In red-ginseng snacks, 10 % potato-starch supplementation followed by FD produced G' values of ~4–9 kPa, locating their hardness between commercial pastry and dark chocolate while preserving ginsenoside content [99]. To reduce the processing time and energy cost of FD, microwave vacuum drying couples MW volumetric energy delivery with a low-pressure environment, accelerating dehydration while maintaining interconnected porosity; in rose-yam paste, MVD reduced processing time by 84 % relative to FD with comparable sensory outcomes [95]. Trade-offs between dimensional shrinkage, microstructural porosity, and functional-quality retention across these drying modes are summarised in Table 4.

Beyond dehydration, several emerging mechanical and reactive technologies have been examined as future post-processing routes, although their application to extrusion-printed foods has so far been demonstrated primarily at the ink-preparation (pre-treatment) stage rather than as post-processing of finished prints. Atmospheric cold plasma has been shown to raise the rheological yield stress (τ_y) and surface rigidity of gelatin-based inks at room temperature through reactive-oxygen / nitrogen-species etching and chemical crosslinking [139], and ultrasonic acoustic cavitation has been applied to ovalbumin – gellan-gum emulsion gels to disrupt entangled networks and raise water-holding capacity prior to deposition [140] — but their direct application to printed constructs as post-processing modalities remains an open research direction. A distinct photochemical route has, however, been demonstrated: ultraviolet-C (UV-C) irradiation of ergosterol-incorporated purple-sweet-potato pastes and mushroom mixtures converts ergosterol into vitamin D_2 during post-processing, enhancing nutritional value without thermal input. High-pressure processing (HPP, 100–600 MPa), which disrupts non-covalent interactions and supports protein refolding without thermal denaturation, has well-established benefits in conventional plant-based meat-analogue production but, to the best of the authors' knowledge, has received only limited reporting as a direct post-processing operation on extrusion-printed constructs. These three modalities — cold plasma, ultrasound, and HPP — together with pulsed electric fields, pulsed light, and ohmic heating, therefore constitute a current research frontier for non-thermal post-processing of 3D-printed foods, where the texture–nutrition coupling could in principle be tuned without thermal compromise.

ACCEPTED PAPER

Despite the conservation advantages of non-thermal modalities, three challenges presently limit their adoption as primary post-processing routes for extrusion-printed foods: (1) FD and MVD demand long processing times (24–72 h for FD; >4 h for MVD) and high capital cost, limiting throughput in distributed-printing scenarios; (2) cold plasma, ultrasound, and HPP have been reported almost exclusively at the ink-preparation stage rather than on finished printed constructs, leaving the post-deposition application of these stimuli as an open experimental space; and (3) photochemical conversions such as the ergosterol-to-vitamin-D_2 route remain substrate-specific and have not been generalised across the full range of UV-responsive bioactive precursors. The integration of these non-thermal stimuli with the volumetric MW pathway of Section 5.2 — for example, sequential or simultaneous MW + UV-C exposure — represents the most direct route to combining structural fixation with targeted nutritional enhancement.

5.4 Quality-Control Framework for Post-Processed 3D-Printed Foods

The post-processing modalities reviewed above show substantial mechanistic diversity, but the field has not yet converged on a unified quality-control (QC) framework analogous to the European Pharmacopoeia monographs that govern pharmaceutical 3D-printed solid dosage forms. Food is not subject to a single supranational pharmacopoeia, yet a coherent QC specification can be assembled from established food-science standards — Codex Alimentarius general standards, AOAC Official Methods of Analysis, ISO microbiological methods, the International Dysphagia Diet Standardisation Initiative testing framework, and the INFOGEST harmonised in vitro digestion protocol [141]. This convergence is increasingly relevant because extrusion-based 3D-printed foods are migrating from research demonstrators toward medicalised applications (dysphagia diets, personalised nutrition, clinical bioactive delivery), where label-claim accuracy, batch-to-batch consistency, and microbial safety must be assured at clinically relevant tolerance levels.

Table 4 presents a proposed release specification for post-processed 3D-printed foods, organised by QC category with technique-specific relevance. The QC parameters that determine the success of a post-processing operation can be grouped into four risk-tiered categories: (i) safety-critical parameters (microbial load, water activity, Maillard hazards, oil content); (ii) label-claim parameters (nutritional content, bioactive retention, IDDSI level, probiotic viability); (iii) texture-and-appearance parameters (TPA, dimensional fidelity, porosity, colour); and (iv) characterisation parameters (Tg / Tg′, in vitro digestibility profile, moisture content). As shown in Table 4, risk levels are assigned according to each parameter's impact on consumer safety, regulatory compliance, and clinical efficacy, with technique-specific relevance indicated for each modality reviewed in Sections 5.1–5.3.

The risk-level assignment in Table 4 is intended as a baseline that may be tightened or relaxed depending on the regulatory category of the final product. For 3D-printed foods marketed as conventional snacks, the safety-critical tier (microbial load, water activity, Maillard hazards, oil content) is sufficient for compliance with general food-law requirements. For medicalised applications — particularly IDDSI-classified dysphagia diets and clinical functional foods — the label-claim tier (nutritional content, bioactive retention, IDDSI compliance) becomes equally critical, since deviations from declared values can directly affect therapeutic outcomes. For probiotic-containing constructs, viability at end of shelf life should be tested under conditions that simulate the intended storage chain; encapsulation–post-processing combinations such as the spray-freeze-drying / freeze-drying sequence, which has yielded 79 % in vitro survival under simulated digestion and 96–98 % stability over 35 days [110], provide a reference benchmark.

Table 4. Six-category QC specification for post-processed extrusion-based 3D-printed foods, with thresholds, methods, and technique-specific relevance.

Category	Parameter	Threshold / Specification	Standard / Method	Source / Reference	Relevance

ACCEPTED PAPER

Safety-critical	Aerobic Plate Count (APC)	< 10^4 CFU/g	Pour plate, 30 °C	ISO 4833-1:2013	All; critical for non-thermal
	Salmonella spp.	Absent in 25 g	Horizontal detection method	ISO 6579-1:2017	All RTE products
	Listeria monocytogenes	Absent in 25 g or < 100 CFU/g	Detection / enumeration	ISO 11290-1/2; EU 2073/2005	RTE supporting growth
	Water activity (aw)	< 0.6 for shelf-stable	Direct measurement	ISO 21807:2004	All
	Acrylamide	< 750 µg/kg (potato crisps)	HPLC-MS/MS	EU Reg 2017/2158	Frying, baking
	Oil / fat content	Method-dependent oil-uptake limit	AOAC 996.06 (GC) or 920.39 (Soxhlet); TD-NMR	AOAC Compendium	Deep-frying, air-frying
Label-claim	Protein	Per nutrition-label ± 20 %	AOAC 992.15 (combustion) or 968.06 (Kjeldahl)	AOAC; FDA 21 CFR 101.9	All techniques
	Fat (total / saturated / trans)	Per nutrition-label ± 20 %	AOAC 996.06 (GC)	AOAC	All techniques
	Total dietary fiber	Per nutrition-label ± 20 %	AOAC 985.29 (enzymatic-gravimetric)	AOAC	All techniques
	Bioactive retention	Method-dependent retention target	HPLC-DAD/MS; ABTS / ORAC	Validated assays	All thermal
	IDDSI compliance	Compliant with declared level	IDDSI testing methods	IDDSI Framework v2.0 (2019)	Dysphagia, soft-textured
	Probiotic viability	≥ 6 log CFU/g at end of shelf life	Plate count (ISO 7218); flow cytometry	FAO/WHO 2002	FD, MVD, low-T
Texture	Hardness / firmness	Product- or IDDSI-level dependent	TA.XT texture analyser (TPA, two-bite)	ISO 11036 (sensory)	All techniques

ACCEPTED PAPER

	Crispness	Product-specific	TPA + acoustic emission	—	Frying, MW, FD
Microstructure	Porosity	Product-specific	X-ray micro-CT; mercury porosimetry	ASTM E1570	FD, MVD, MFD, MW
	Dimensional fidelity	≥ 85 % match to digital design	Image analysis; X-ray micro-CT	3DP industry benchmark	MW, frying
Appearance	Colour / shape / mass	Visual + objective	CIE Lab colorimeter; calipers	CIE 015:2004	All techniques
	Colour stability	$\Delta E^*ab < 3$ across shelf life	Colorimeter (CIE Lab)	CIE 015:2004 (JND)	Pigmented products
Characterisation	Moisture content	Method/matrix-dependent	AOAC 934.06 (fruit), 950.46 (meat), 925.45 (sugar); Karl Fischer	AOAC	Drying methods
	In vitro digestibility	Per design intent	INFOGEST 2.0 protocol	Brodkorb et al. 2019 [141]	All techniques
	Tg / Tg′	Below intended storage T	DSC	—	FD, MVD, MFD

To support end-product quality without compromising throughput, non-destructive in-line analytical methods are increasingly used as Process Analytical Technology (PAT) tools for post-processed 3D-printed foods, mirroring the trajectory observed in pharmaceutical 3D printing where near-infrared spectroscopy has become a standard non-destructive identity-and-content assay. Five PAT modalities are well-matched to the post-processing operations reviewed above: NIR spectroscopy for moisture / fat / protein quantification during drying-based post-processing; hyperspectral imaging for spatially resolved browning and bioactive-pigment retention measurement during baking, frying, and MW post-processing; machine-vision systems coupled with deep-learning classifiers for real-time monitoring of dimensional fidelity, infill integrity, and over-puffing detection during MW exposure (with recent integration of in-line graphene IR heaters with generative-AI-assisted pattern design demonstrating that simultaneous in-situ printing and cooking is technically feasible within a single integrated print-and-cook system [124]); time-domain NMR / LF-NMR relaxometry for non-destructive water-state quantification (validated as a printability predictor and extendable to post-processing endpoint determination); and acoustic-emission monitoring to capture crispness development in real time during frying and MW puffing.

The relevance of individual QC parameters to specific post-processing techniques merits explicit comment. Microwave post-processing carries the highest risk for dimensional-fidelity failure (over-puffing) and the highest

ACCEPTED PAPER

opportunity for bioactive retention; in-line dielectric monitoring of ε'' during heating, combined with machine-vision over-puffing detection, addresses both. Microwave freeze drying introduces a power-density-dependent texture–nutrition trade-off that should be mapped explicitly during product development: as quantified by Li et al. [137], 0.5 W/g preserves bioactive content at the cost of mechanical strength, while 4.0 W/g maximises hardness and crispness with 4.30 % greater shape distortion than at 0.5 W/g — a trade-off that should be reported in product specifications. Freeze-drying requires stringent water-activity control as the principal safety-critical parameter, since the absence of thermal lethality means microbial load entering the freeze-dryer must be controlled at the printing stage. Deep-fat frying and air-frying require oil-content and Maillard-hazard testing as additional release specifications beyond the baseline QC set. Steaming typically does not require oil-content testing but demands rigorous IDDSI-compliance verification when targeted at dysphagia applications. Baking carries Maillard-hazard risk that scales with bran content and surface-temperature profile; pre-processing of bran (high-intensity ultrasound, HIU; vacuum MW; pulsed light) [83] and dough pH adjustment can reduce acrylamide formation and should be validated in the final QC dataset. Adopting a unified QC framework along the lines of Table 4 would represent a meaningful maturation of the field, and the integrated evaluation paradigm of Tan and Ng [126] — extending printability and texture characterisation to nutritional retention within a single experimental pipeline — illustrates the direction in which the field is moving.

Across the four post-processing modes reviewed in this section — surface-driven thermal, volumetric and electromagnetic, non-thermal, and the unified QC framework that frames all three — post-processing emerges not as a finishing step but as the engineering stage at which the geometric, textural, and nutritional profile of the printed construct is fixed. Among these modes, the volumetric and selective dielectric heating mechanism of microwave processing extends beyond static fixation: by manipulating the asymmetric distribution of ε'' within a printed geometry, MW energy can be configured to drive differential internal swelling and targeted dehydration, generating volumetric stress that acts as the driving force for stimulus-responsive shape morphing. Selective dielectric heating of localised pH-reactive components or specific microcapsules can additionally trigger 4D colour changes and the time-dependent release of encapsulated flavours and nutrients. MW post-processing therefore introduces the time dimension (t) into the printed construct, providing the most direct bridge from the static fidelity of 3DFP to the programmable evolution of 4D smart structures examined in the following section.

ACCEPTED PAPER

6. 4D Food Printing: Stimulus-Responsive Transformations of the Printed Construct

In this section, a critical review of stimulus-responsive 4D transformation in extrusion-based 3DFP is presented, emphasizing its pivotal role in extending the printed construct from a static deliverable into a programmable substrate whose post-deposition trajectory evolves along the time dimension (t). This review connects directly to the post-processing engineering of Section 5, which fixed the deposited construct at a textural and nutritional endpoint; the present section examines what happens when the same construct is intentionally configured to continue evolving after deposition under a defined external or internal stimulus.

The unifying design principle underlying 4D food printing is the asymmetric distribution of dielectric, pH-active, encapsulated, or biologically active components established at the printing stage. Under an applied stimulus — dehydration, microwave dielectric heating, pH change, UV-C irradiation, or embedded biological growth — this asymmetry drives the construct to evolve along one or more programmable axes. This review organises 4D transformation along three primary response axes: shape morphing (Section 6.1), colour and appearance change (Section 6.2), and flavour development and nutritional evolution (Section 6.3); a fourth subsection (Section 6.4) treats the synchronised multi-axis transformations that have emerged as the cutting edge of the field. Table 5 presents stimulus-responsive 4D studies organised along these four response axes, reporting substrate, stimulus, and key quantitative endpoints; the table is the empirical scaffolding against which the discussion below is structured.

6.1 Shape Morphing

Shape morphing of the printed construct emerges when an applied stimulus generates an anisotropic mechanical response within the deposited geometry. This subsection examines three mechanistic regimes through which such anisotropic responses have been engineered in extrusion-based 3D-printed foods: dehydration-driven actuation that exploits compositional asymmetry between layered substrates; groove-engineered morphing that replaces compositional layering with surface-patterned asymmetry; and microwave-induced selective expansion that leverages component-specific dielectric loss to drive localised puffing. A continuum-mechanics framework that has recently been formulated to unify these regimes is discussed at the close of the subsection.

Dehydration-driven anisotropic actuation exploits the differential shrinkage of layered or compositionally heterogeneous matrices. When a printed bilayer composed of an active hydrocolloid layer over a passive food-grade film is subjected to hot-air, infrared, or microwave dehydration, the bending angle of the construct scales with the shrinkage ratio of the active layer; hot-air drying produces the largest accumulated bending owing to a "bending-accumulation effect" that propagates from surface to interior, while microwave dehydration heats too rapidly through the volume to allow the surface gradient to develop [142]. Bilayer studies on pumpkin – edible-paper [18] and cricket-flour [143] systems have extended this mechanism across substrate types, yielding bending angles of 25–110° and 30–120° respectively under controlled shrinkage of 25–55 %. An earlier study had already shown that microwave-induced dehydration of 3D-printed starch-based purple-sweet-potato purées produces a comparable spontaneous shape change, with deformation rate and degree governed by microwave power, infill geometry, and salt content [144].

Whereas dehydration-driven actuation depends on compositional asymmetry between layered substrates, groove-engineered anisotropic morphing replaces compositional asymmetry with surface-patterned asymmetry: when the construct is formed with stamped grooves of varying depth and orientation, the differential drying rate at the grooved surface establishes an in-plane stress gradient that drives bending or twisting upon dehydration. In a pea-protein-isolate construct (60 g PPI : 40 g water + 5 g xanthan gum), 3 mm grooves dried at 65 °C produced a maximum bending angle of 183 ± 3.14° with curvature ~0.19 mm^{-1}, while a 45° groove orientation yielded a maximum twisting angle of 320° at curvature 0.22 mm^{-1} — showing that printed surface geometry alone, without compositional layering, can program complex morphing trajectories [145].

ACCEPTED PAPER

Beyond compositional and surface-patterned asymmetry, microwave-induced selective expansion operates through the same component-selective ε'' contrast that drives over-puffing in Section 5.2, but is intentionally configured as a deformation actuator rather than suppressed as a failure mode. When the construct contains compositional domains of disparate dielectric loss factors, MW exposure deposits energy preferentially in the high-ε'' regions, generating localised hot spots whose internal vapour pressure (ΔP) exceeds that of the surrounding domains. The construct deforms by directional micro-puffing along the hot-spot field rather than through bulk dehydration. This mechanism appears to have been first reported in a purple-sweet-potato-purée (PSPP) / oleogel bilayer construct, in which the high-ε'' PSPP layer heated volumetrically while the MW-transparent oleogel remained inert, producing reproducible directional bending under MW exposure [146]; the time-resolved bending trajectory at applied power densities of 2–8 W/g is shown in Fig. 9B [144]. Subsequent studies have extended this principle along two complementary axes. Niu et al. demonstrated bidirectional concave–convex deformation in coix-seed / PSPP constructs through sequenced sub-domain puffing [147], while Guo et al. showed that increasing soy-protein-isolate content within an oat-flour butterfly construct increased its bending angle by trapping water vapour within a denser microstructure rather than by enhancing water loss [148]. The deformation pathway in these constructs is therefore puffing-dominant rather than dehydration-dominant, which decouples shape change from substantial mass loss and preserves bioactive content within the deformed matrix. Most recently, a continuum-mechanics framework coupling mass transfer with large-deformation FEM has been formulated for this class of system, predicting buckling-driven hyperbolic-paraboloid morphing in compliant-core / stiff-rim disk constructs and providing a generalisable theoretical basis for programmable food-construct morphing [149].

Despite the convergence of these three mechanistic regimes toward a generalisable programmable-morphing framework, three challenges remain in their translation to deliverable 4D food products: (1) the bending- and twisting-angle endpoints reported in the literature (25–320°) are sensitive to substrate composition, ambient humidity, and operator-specific drying profiles, limiting cross-laboratory reproducibility; (2) dehydration-driven regimes inherently couple shape change with mass loss, whereas MW-puffing regimes decouple the two — the trade-off between this decoupling advantage and the over-puffing risk of Section 5.2 has not, to the authors' knowledge, been systematically quantified across substrate classes; and (3) the continuum-mechanics framework of van der Sman [149] has been formulated for a single disk geometry and remains to be generalised to the multi-layer and gradient-composition constructs that dominate experimental practice. Resolving these challenges would extend shape morphing from demonstration-grade phenomena to predictable design endpoints.

6.2 Colour and Appearance Change

Colour evolution of the printed construct, unlike shape morphing, can be triggered without any mechanical change to the matrix and therefore offers an independent design axis. Three mechanistic pathways dominate the food-printing literature on programmable colour change: pH-driven tautomerisation of anthocyanin pigments distributed within the matrix; analogous pH-driven keto–enol tautomerisation of curcumin under alkaline stimulation; and microwave-triggered rupture of dispersed microcapsules that release encapsulated pigment payloads into the surrounding matrix. The three pathways are reviewed in turn, with particular attention to how each has been adapted from a passive colour transition into an active diagnostic or dysphagia-compatible signalling system.

pH-driven anthocyanin tautomerisation exploits the pH-sensitivity of cyanidin- and pelargonidin-class pigments distributed within the printed matrix or its adjacent compartment. Foundational dual-extruded constructs established the principle on which subsequent microcapsule-based variants were built. In a dual-extruded composite construct of mashed potato (containing anthocyanin-rich purple sweet potato) layered against an acidified compartment (lemon-juice-starch gel), proton diffusion across the interface drives a continuous spontaneous colour transition that proceeds without external intervention [150]. A more comprehensive demonstration was obtained when the printed matrix incorporated red-cabbage juice and vanillin powder distributed through a potato-starch carrier: external pH stimulation

ACCEPTED PAPER

across the pH 2–10 range produced a controllable spectrum of colour states — red, purple, violet, blue, blue-green, and green-yellow — with E-nose and E-tongue measurements confirming that the same pH gradient simultaneously modulated volatile and taste profiles, and dried samples retained anthocyanin stability over three weeks of ambient storage [151]. A more recent demonstration combined pH-triggered colour change with IDDSI compliance in a purple-sweet-potato / pea-protein / HPMC system, simultaneously satisfying dysphagia-diet criteria and embedded colour reporting [152].

Curcumin keto–enol tautomerisation parallels the anthocyanin route through an alternative pigment with a complementary pH range and higher thermal stability, broadening the operating envelope of pH-driven colour-change food printing. In sago-starch constructs blended with turmeric, alkaline stimuli triggered the keto-to-enol transition in curcumin and produced a clean yellow-to-red colour shift mapped quantitatively across the operating pH window [153] (Fig. 9A). In a thermally-decoupled variant, citrus-pectin / β-cyclodextrin Pickering-emulsion constructs produced an analogous curcumin-mediated colour shift through sodium-bicarbonate-driven matrix alkalinisation following thermal decomposition, additionally indicating temperature as a viable trigger for pH-mediated colour change [154].

Whereas the two pH-based pathways operate through diffusion-mediated chemistry, MW-triggered microcapsule rupture appears among the most actively developed colour-change pathways in current food-printing literature. Dielectric heating disrupts the wall of dispersed microcapsules within the printed matrix and releases their pigment payload into the surrounding gel. In 3D-printed apple / potato-starch gels containing freeze-dried red-cabbage-juice-loaded WPI / gum-arabic microparticles, MW exposure produced a rapid yellow / brown → red transition with significant ΔE while the construct retained dimensional fidelity [155]. Extending this principle to dual-payload systems, yam-gel constructs containing soybean-protein-isolate / chitosan / maltodextrin complex-coacervate microcapsules carrying water-soluble betacyanin and rose essence (W/O/W double emulsion) released both payloads under MW disruption, producing pigment release into the matrix (yellow-to-red colour shift) coupled with directional construct deformation and aroma evolution within 45 s [156]. The same coacervate / microcapsule rupture mechanism has been adapted as a non-destructive freshness-indicator system, transforming the printed construct from a passive food product into an embedded sensor of its own state. In an anthocyanin-encapsulated carrageenan / xanthan shell surrounding a surimi inner core, the printed construct showed a quantitative ΔE response to volatile amines released during spoilage [157]; a parallel anthocyanin / Ca^{2+}-nano-starch-lutein surimi system established quantitative spoilage thresholds, with $\Delta E < 4$ corresponding to fresh (3–5 d), $\Delta E > 6$ to early spoilage (7 d), and $\Delta E > 16$ to spoiled (9 d) states — making the printed construct itself the diagnostic instrument [158]. A complementary betanin / gelatin / nano-chitin surimi system demonstrated reversible pH-triggered colour change with first-order kinetics, extending the indicator concept to dysphagia-compatible surimi [159]. The same MW dielectric pulse that drives a colour response in a pigment-loaded construct can also drive a flavour response in an aroma-loaded construct, and the transition between Sections 6.2 and 6.3 is therefore mechanistic rather than categorical.

Despite the diversity of programmable colour-change pathways, three challenges presently limit their integration into deliverable functional foods: (1) the colour endpoints reported in the literature (ΔE 4 – >16) are characterised under controlled laboratory conditions, and the colour-stability windows of anthocyanin and betalain pigments under typical consumer storage conditions appear to remain insufficiently characterised; (2) reversibility of the colour transition has been demonstrated in only a small subset of betanin- and curcumin-based systems [159], whereas anthocyanin-based transitions are predominantly unidirectional, constraining the design of multi-use indicator constructs; and (3) the sensory acceptability of stimulus-induced colour transitions has rarely been validated through consumer panels, leaving the translation from diagnostic novelty to consumer-facing product as an open research direction.

ACCEPTED PAPER

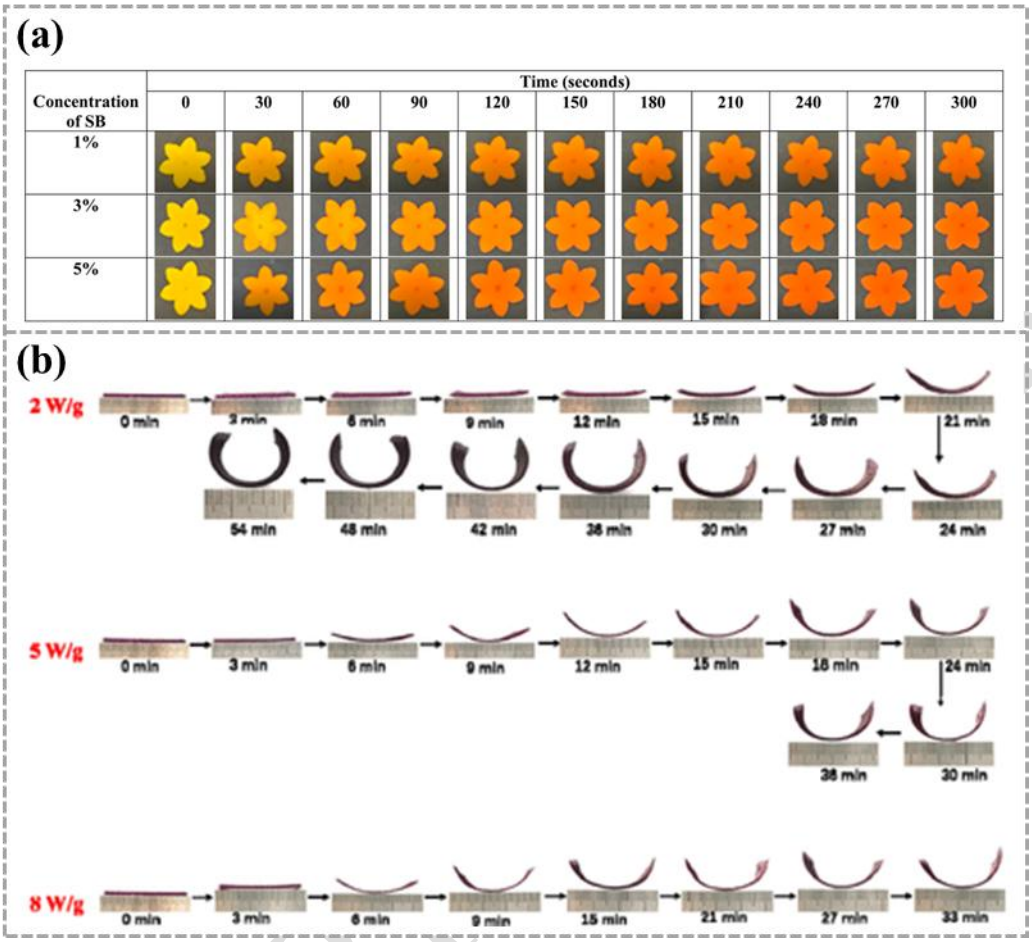


Fig. 9. Stimulus-responsive transformations of extrusion-based 3D-printed food constructs. (a) pH-triggered spontaneous colour change of sago starch–turmeric constructs upon immersion in sodium bicarbonate solution [153]. (b) Microwave-induced shape morphing of purple sweet potato purée bilayer constructs at applied power densities of 2, 5, and 8 W/g [144]. Panel (a) reprinted with permission from Shanthamma et al. [153] Copyright © 2021 American Chemical Society. Panel (b) reprinted with permission from He et al. [144] Copyright © 2020 American Chemical Society.

6.3 Flavour Development and Nutritional Evolution

Flavour evolution and nutritional evolution share a feature that distinguishes them from the previous two axes: the response is chemical rather than mechanical, and the engineering challenge is consequently one of programmable molecular release from the printed matrix. Three mechanistic pathways are reviewed below: thermal generation of flavour compounds through Maillard and lipid-oxidation chemistry within microwave-activated subregions; controlled release of pre-encapsulated aroma payloads through microcapsule rupture; and photochemical conversion of resident precursors into target nutrients under non-thermal UV-C irradiation. A fourth mechanistic class — biological 4D / 5D evolution — replaces external stimuli with embedded biological growth as the time driver, and is treated at the close of the subsection.

MW-induced flavour-compound generation exploits Maillard and lipid-oxidation chemistry within thermally activated subregions of the printed matrix. In SPI / κ-carrageenan / vanillin constructs, exposure to 50–80 W microwave specifically generated four new flavour compounds — 1-octen-3-ol, maltol, ethyl maltol, and eugenol — that were absent in identical unprinted controls, indicating that the spatial distribution of components established at the printing stage influences the chemistry of the resulting flavour profile [16]. Adopting an analogous spatial-asymmetry approach with a different stimulus, surface-pH treatment of an SPI / pumpkin / beetroot composite construct produced a co-evolution of colour, texture, and flavour through betalain rearrangement and protein-matrix modification [75].

Encapsulated aroma release parallels the microcapsule-rupture mechanism of Section 6.2 but targets volatile aroma compounds rather than pigments, exploiting the same dielectric-disruption mechanism to release headspace-active payloads. Gelatin – gum-arabic complex coacervates loaded with cinnamaldehyde and pepper red pigment in buckwheat – peach-dough constructs, when stimulated by 4 min MW exposure, more than doubled (E)-cinnamaldehyde concentration in the construct headspace and shifted the a*-colour value upward — a co-axial colour / aroma response within a single MW pulse [160]. Building on this, white-mushroom-gel constructs containing gelatin / β-cyclodextrin microcapsules released ~272 μg/kg γ-dodecalactone into the construct headspace under 3 min MW exposure, providing quantitative control over headspace aroma intensity [161].

Photochemical nutritional conversion replaces MW heating with non-thermal UV-C irradiation as the stimulus and exploits photochemical rather than thermal chemistry, opening a route to bioactive enhancement without thermal degradation of co-existing nutrients. In a 3D-printed mushroom – purple-sweet-potato construct, UV-C exposure converted matrix-resident ergosterol to vitamin D_2 in situ, transforming the construct from a passive food product into an active nutritional-enhancement device that delivers a bioactive payload it did not contain at the time of deposition [162]. The mechanism was subsequently extended into a hybrid MW + ultrasound + UV-C pipeline that further raised the ergosterol-to-vitamin-D_2 conversion efficiency, indicating that multi-stimulus stacking can amplify single-stimulus responses [163].

Beyond external stimuli, a distinct mechanistic class — biological 4D / 5D printing — replaces engineered triggers with embedded biological growth as the time driver of construct evolution. In a starch–protein construct co-deposited with *Lactobacillus* probiotics, fermentative pH descent over the storage period drove a spontaneous anthocyanin tautomerisation that simultaneously served as a sensory colour signal and a record of cumulative live probiotic activity [164]. In a more recent demonstration of biological texture engineering, soy-protein / cassava-starch constructs co-deposited with *Pleurotus eryngii* mycelia underwent 10 days of post-deposition mycelial growth that produced an 18.2 % biomass gain and a 6.11-fold increase in finished hardness, accompanied by direct synthesis of β-glucan and ergothioneine within the construct — an early demonstration of biological post-processing for meat-analogue texture and nutritional engineering [165].

Despite the breadth of flavour and nutritional evolution pathways reviewed above, three challenges remain in their translation to clinically and commercially meaningful products: (1) the dose precision of released flavour and bioactive payloads (currently reported at the μg/kg level for headspace volatiles) remains substrate-specific and operator-dependent, limiting label-claim verification under the QC framework of Table 4; (2) the bioavailability of *in situ* generated nutrients — most notably the UV-C-derived vitamin D_2 — has been demonstrated *in vitro* but, to the authors' knowledge, has not yet been validated in human intervention studies; and (3) biological 4D / 5D constructs introduce a microbiological safety dimension that conventional food regulation does not address, with edible mycelia and live probiotics requiring extended viability and safety monitoring across the intended storage chain. Resolving these challenges would extend flavour and nutritional evolution from proof-of-concept demonstrations toward regulatory-grade functional foods.

ACCEPTED PAPER

6.4 Synchronised Multi-Axis Transformations

This subsection examines the synchronised multi-axis transformations that have emerged as the cutting edge of 4D food printing, in which two or more of the response axes treated in Sections 6.1–6.3 are engineered to evolve concurrently within a single construct under a single stimulus. The studies reviewed here represent the operational consolidation of the asymmetric-distribution design principle introduced in the chapter opening: when shape-, colour-, and flavour-active components are co-deposited with deliberately differentiated ε'', pH-active, or microcapsule profiles, a single MW or pH pulse can drive simultaneous evolution along all three axes. The discussion proceeds from single-stimulus multi-axis systems to dual-stimulus and higher-dimensional design paradigms, closing with the unifying engineering principle that underlies all four subsections of this chapter.

Single-stimulus multi-axis transformations represent the most directly developed of these consolidation strategies. The yellow-flesh-peach – buckwheat-paste system [166] showed that a 200 W localised MW pulse induces directional micro-puffing within 90 s, and that adding pigment- and flavour-loaded microcapsules to the same construct extends the response to a synchronous deformation + colour + aroma transformation within 15 s under a 700 W household microwave. Building on this single-stimulus tri-modal demonstration, the yam-gel double-emulsion system [156] achieved a fully synchronised three-response (colour + shape + flavour) "spreading-of-wings" transformation in bird-shaped constructs within 45 s. In a parallel direction, hybrid microwave-infrared post-processing of white radish / potato gel constructs with embedded microcapsules elevated hardness and springiness while preserving the encoded multi-response pattern [167].

Beyond single-stimulus systems, dual-stimulus designs extend the response space along orthogonal stimulus axes. Mixed-vegetable gel constructs subjected to combined acidification and dehydration produced shape and colour evolution along the two stimulus axes simultaneously [168], extending the design space beyond what either stimulus alone could deliver. The trajectory of these advances appears to point toward what the recent multi-dimensional-printing literature [169] refers to as 5D and 6D food printing — the integration of higher-dimensional design freedom (curved-layer deposition, addressable composition gradients) with stimulus-responsive transformation along an arbitrary number of evolution axes. Within this framework, the printed construct is no longer a discrete deliverable but a programmable substrate whose post-deposition trajectory is partly specified at the ink-design and printing stage.

The unifying engineering principle across Sections 6.1–6.4 — that the asymmetric distribution of ε'', pH-active groups, encapsulated payloads, or biological growth elements within the printed geometry shapes the evolution trajectory of the construct under a given stimulus — applies equally to all axes treated in this section, and provides a single conceptual basis for the design of next-generation 4D food printing systems. Across all four axes, however, the literature reviewed here characterises 4D transformations predominantly through physical endpoints — bending angle, ΔE, headspace concentration — while consumer sensory acceptability, palatability, and the textural consequences of the transformation for chewing and swallowing remain only sporadically evaluated; closing this sensory gap is a prerequisite for translating 4D constructs from demonstrations into clinical and consumer-facing foods.

Despite the consolidation of single-stimulus multi-axis transformations as a distinct design paradigm, three challenges constrain the scale-up of synchronised multi-axis 4D food printing: (1) the temporal coupling between the response axes (e.g., colour-shape-flavour onset within 15–45 s) is reported with substrate-specific stimulus parameters that have not, to the authors' knowledge, been systematically standardised; (2) the predictive modelling of multi-axis trajectories combines mechanical (Section 6.1), pH-chemical (Section 6.2), and release-kinetic (Section 6.3) sub-models that are currently treated independently, leaving multi-axis prediction at an empirical rather than mechanistic stage; and (3) the 5D / 6D paradigm anticipated by Zhao et al. [169] presupposes hardware platforms (curved-layer deposition, addressable composition gradients) that remain to be commoditised across the extrusion-based 3DFP equipment landscape. Addressing these challenges would translate synchronised multi-axis evolution from demonstration constructs to scalable design rules.

ACCEPTED PAPER

Table 5. 4D food printing by response axis: shape morphing, colour change, flavour/nutritional evolution, and synchronised multi-axis transformation.

Response axis	Reference	Stimulus	Key result
Shape morphing	[142]	Air / MW dehydration	Bending scales with active-layer shrinkage and inversely with ε'', with air drying outperforming microwave.
	[144]	MW	Microwave dehydration drives spontaneous shape change tuned by power, infill, and salt content.
	[18]	Hot-air drying	Bending increases with drying time toward a near-cylindrical form, controlled by drying time, printing path, and layer thickness.
	[143]	Hot-air drying (80 °C)	Higher infill density produces progressively larger bending under thermal dehydration.
	[146]	MW (power-tuned)	Dielectric-loss asymmetry between layers drives directional bending under microwave.
	[147]	MW	Sequenced sub-domain puffing yields bidirectional concave–convex deformation.
	[148]	MW	Higher SPI content enlarges bending by trapping vapour in a denser microstructure.
	[145]	Drying 65 °C; frying 210 °C	Printed surface grooves alone program bending (~183°) and twisting (~320°).
	[149]	Differential drying	A continuum-mechanics FEM model predicts buckling-driven hyperbolic-paraboloid morphing.
Colour change	[150]	Internal pH gradient	An internal pH gradient drives spontaneous colour change without any external trigger.
	[154]	Temperature → $NaHCO_3$	Thermal decomposition raises matrix pH, turning curcumin yellow-to-red.
	[153]	pH ($NaHCO_3$)	Alkaline stimulus maps a quantitative pH-to-colour shift from yellow to orange-red.
	[155]	MW	Microwave rupture of microparticles turns the gel yellow/brown-to-red with significant ΔE.
	[152]	pH	pH-triggered colour change is achieved within an IDDSI-compliant dysphagia matrix.
	[159]	pH	Betanin enables a reversible colour change following first-order kinetics, IDDSI-compatible.
	[157]	Spoilage volatiles	An anthocyanin shell reports spoilage-driven pH change as a colour shift.
	[158]	Time / spoilage	Colour tracks freshness, shifting from $\Delta E < 4$ (fresh) to > 16 (spoiled).
Flavour & nutrition	[16]	MW (50–80 W)	Microwave heating generates four new flavour compounds absent in controls.
	[75]	Surface-pH spray	Surface-pH treatment co-evolves colour, texture, and flavour together.
	[160]	MW (4 min)	A 4-min microwave pulse more than doubles headspace (E)-cinnamaldehyde.

ACCEPTED PAPER

	[161]	MW (3 min)	Microwave rupture releases ~272 μg/kg γ-dodecalactone into the headspace.
	[162]	UV-C	UV-C irradiation converts resident ergosterol into vitamin D_2 in situ.
	[163]	MW + US pretreatment → UV-C	MW + ultrasound pretreatment raises the UV-C-driven vitamin-D_2 yield several-fold.
	[164]	Probiotic fermentation	Fermentative pH descent drives an anthocyanin colour change recording live activity.
	[165]	Mycelial growth (10 d)	Mycelial growth raises hardness 6.11-fold while synthesising β-glucan and ergothioneine.
Multi-response	[166]	MW (200 → 700 W)	A localised microwave pulse triggers shape, colour, and aroma change within 15 s.
	[156]	MW	A single microwave pulse bends, colours, and flavours a bird construct within 45 s.
	[151]	pH (external / internal)	A pH 2–10 sweep produces a six-state colour spectrum with coupled aroma and taste shifts.
	[168]	Acidification + dehydration	Combined acidification and dehydration drive shape and colour change together.
	[167]	MW + IR hybrid	Hybrid microwave–infrared raises hardness and springiness while preserving the multi-response pattern.
	[170]	MW + IR	Sequential infrared-then-microwave heating balances form stability against 4D activation.

7. Applications of Extrusion-Based 3D Food Printing

Sections 2 through 6 reviewed the engineering foundations of extrusion-based 3DFP, from process fundamentals to stimulus-responsive transformations; this section turns to the application contexts in which these capabilities have advanced beyond proof-of-concept toward functional product development. The capacity of extrusion-based 3DFP to fabricate geometrically complex, compositionally precise, and structurally customised food constructs has supported its adoption across three converging application domains: personalised nutrition and texture-modified food for specific dietary needs, bioactive-enriched food for therapeutic and clinical nutrition, and plant-based and alternative-protein food development. The discussion begins in Section 7.1 with personalised and functional food, focusing on dysphagia diets and on-demand customised products. Section 7.2 then consolidates bioactive-enriched applications — probiotic, vitamin, and antioxidant payloads carried within the printed construct. Section 7.3 then examines plant-based and alternative-protein applications, where 3D printing offers a route to fibrous meat-analogue microstructure that conventional processing does not readily provide.

7.1 Personalised and Functional Food

The capacity to fabricate food with controlled texture, shape, and composition makes extrusion-based 3D printing well suited to populations with special nutritional or physiological needs. Two converging directions of personalised application are reviewed below: dysphagia management, where IDDSI-graded texture compliance has driven the most concentrated research effort; and on-demand food manufacturing for special-purpose populations, where preference-matched fabrication has begun to be evaluated outside laboratory settings.

The IDDSI framework has served as the primary formulation endpoint in dysphagia-focused 3D printing research, providing standardised texture levels against which printed constructs can be objectively validated. Cooked beef paste

ACCEPTED PAPER

formulated with hydrocolloids (XG, guar gum, carrageenan, LBG) at 0.5–1 % reached IDDSI levels 5, 6, and 7 with good dimensional stability, indicating that texture-modified meat products can be fabricated to meet clinical swallowing-safety requirements [65]. Cooked pork paste with XG and guar gum (0.36 %) satisfied the IDDSI transitional-food classification while producing a softer texture than unmodified controls, with hydrocolloid-assisted moisture retention identified as the key mechanism [44]. For mushroom-based dysphagia diets — addressing the need to make nutritionally dense but inherently fibrous foods accessible to dysphagic patients — black fungus formulated with XG (0.9 %) reached IDDSI level 5 compliance [101], and shiitake mushroom with XG and κ-carrageenan satisfied the same classification while retaining the visual identity of the original ingredient [102]. A substrate-adaptive approach to fresh-vegetable printing supported IDDSI compliance across peas, carrots, and bok choy by selecting hydrocolloid systems matched to each substrate's starch content [103]. Together, these studies indicate a practical design framework for 3D-printed dysphagia diets: hydrocolloid type and dosage should be tailored to both the substrate composition and the target IDDSI level, and dimensional accuracy under shear should be co-validated with textural compliance.

Beyond clinical dysphagia management, 3DFP has been examined for on-demand food manufacturing for special-purpose populations. A real-life consumer study conducted in a military setting provided soldiers with progressively customised 3D-printed snack bars over four weeks, identifying repeated exposure and customisation options as key drivers of acceptance and attitudinal shift toward the technology [10]. The study is one of the few investigations of 3DFP acceptance in a non-laboratory setting, and its findings suggest that on-demand, preference-matched food fabrication is a feasible direction for deployment in contexts that require individualised nutrition at scale.

Despite the rapid maturation of dysphagia-focused 3D printing and the early signals from on-demand consumer studies, two challenges remain in the deployment of personalised and functional printed foods: (1) the IDDSI compliance demonstrated across substrate classes has been characterised primarily in laboratory settings, and the batch-to-batch consistency of compliance under distributed point-of-care printing has not, to the authors' knowledge, been systematically reported; in particular, distributed point-of-care fabrication raises regulatory and traceability questions — batch documentation, allergen control, and responsibility for label-claim verification — that centralised manufacturing does not, and that current food-safety frameworks have yet to address for on-site printed foods; (2) the sensory acceptability of texture-modified dysphagia products relative to conventional purée alternatives appears insufficiently characterised in clinically relevant patient cohorts.

7.2 Bioactive-Enriched Food

Beyond texture compliance, extrusion-based 3DFP has been used to embed clinically relevant bioactive payloads within the printed construct, positioning it as a delivery platform for therapeutic and special-purpose nutrition. Two payload classes have been demonstrated.

Probiotic enrichment. Bifidobacterium animalis subsp. lactis BB-12 incorporated into mashed potato remained viable through refrigerated storage, with the printing process itself contributing minimal loss except at the narrowest nozzle tested [108]. Encapsulation markedly improved protection: alginate–gelatin-encapsulated B. lactis exceeded 10^9 CFU/g after printing with multi-week room-temperature stability [109], and spray–freeze-dried L. plantarum retained high in-vitro survival and storage stability over several weeks [110]. These results indicate that printed texture-modified foods can carry clinically meaningful probiotic doses, with the QC framework of Section 5.4 providing the corresponding release specification.

Vitamin and antioxidant enrichment. Post-processing can generate or preserve micronutrients in situ: UV-C irradiation of ergosterol-incorporated purple-sweet-potato and mushroom matrices converts ergosterol into vitamin D_2 without thermal input [162,163] (Section 5.3), and alginate-microbead encapsulation of Arthrospira platensis

ACCEPTED PAPER

extracts preserved antioxidant activity and colour stability in printed cookies [111]. These routes connect the post-processing and 4D mechanisms of Sections 5 and 6 to a nutritional endpoint.

Two challenges constrain clinical translation of bioactive-enriched printed foods: (1) payload viability and potency must be monitored across the full storage chain, yet this has been demonstrated only for a limited set of probiotic strains, micronutrients, and substrate combinations; and (2) the same distributed point-of-care fabrication that makes on-demand enrichment attractive raises the regulatory and traceability questions noted in Section 7.1 — dose verification, batch documentation, and responsibility for therapeutic-claim substantiation — which current food-safety frameworks have yet to address for on-site printed foods.

7.3 Plant-Based and Alternative-Protein Foods

The transition toward sustainable protein sources has motivated the development of plant-based foods that approximate the sensory properties of animal-derived products. Extrusion-based 3DFP offers a route toward this goal, supporting the fabrication of complex textures and structures from plant proteins that are difficult to obtain through conventional processing. Three strands of progress are reviewed below: the structural reproduction of anisotropic fibrous microstructure that defines meat-analogue texture; the use of pea protein as a versatile and rheologically tractable plant-protein substrate; and the demonstration of by-product-derived protein sources as functional printing materials.

The principal structural challenge in plant-based meat-analogue development is reproducing the anisotropic, fibrous microstructure of animal muscle tissue. Soy protein combined with wheat gluten and thermosensitive cocoa butter (2.5–5.0 g) printed at 45–60 °C produced a continuous fibrous microstructure upon cooling, with hydrogen bonding between soy protein and gluten networks identified as the primary driver of fibre formation [79]. The result indicates that the material properties and thermal management of 3D printing can generate meat-like structural anisotropy from purely plant-derived ingredients, distinguishing additive manufacturing from conventional texturisation methods.

Among the plant proteins examined for 3D printing, pea protein has shown particular versatility across structural, mechanical, and rheological roles. Pea-protein–alginate blends produced printable constructs with deposit thickness of 0.68 mm identified by additive-layer-manufacturing simulation as the optimum among tested values [46], while a systematic macronutrient-composition study showed that protein content is the primary driver of extrusion force, supporting rational formulation design based on water-holding-capacity normalisation — a methodology with broad applicability across legume-based systems [47]. In a parallel direction, PPI addition (15 %) to banana paste suppressed tailing printing defects by reducing structural recovery rate and elongation at break, indicating that plant proteins can simultaneously provide nutritional fortification and rheological correction in fruit-based composite systems [81].

Beyond conventional plant-protein extraction, by-product-derived alternative-protein sources have also been demonstrated as 3D printing substrates. *Spirulina platensis* residues — the biomass remaining after extraction of phycocyanin and bioactive polysaccharides — were converted into printable inks with well-defined shear-thinning behaviour, supporting microalgae processing by-products as functional printing materials [105]. The convergence of plant-protein research toward both structural meat-analogue fabrication and sustainable raw-material utilisation positions extrusion-based 3D printing as a dual-function technology in the alternative-protein sector.

Despite the breadth of plant-protein systems demonstrated as printing substrates, three challenges remain in the translation of plant-based 3D-printed foods to commercial deployment: (1) the fibrous microstructure achieved through hydrogen bonding between soy protein and gluten networks remains substrate-specific, and a generalisable cross-protein design rule for anisotropic plant-based meat analogues is lacking; (2) the rheological characterisation of

ACCEPTED PAPER

plant-protein composites is dominated by single-protein systems, leaving multi-protein blends — likely to dominate commercial plant-based products — underexplored as printing substrates; and (3) the sensory and consumer-acceptance dimensions of 3D-printed plant-based meat analogues have rarely been characterised against extruded or moulded equivalents, limiting the demonstration of value-added differentiation. Addressing these challenges would extend plant-based 3D-printed foods from structural-feasibility demonstrations toward consumer-deliverable alternatives.

Across the two application domains reviewed in this section — personalised and functional food, and plant-based and alternative-protein products — extrusion-based 3DFP has progressed beyond proof-of-concept toward functional-product development, with the engineering choices identified in Sections 2 through 6 (driving mechanism, substrate formulation, intelligent process control, post-processing, stimulus-responsive design) acting as the upstream determinants of application-stage performance. The unifying physical observables that organised the preceding sections — yield stress τ_y, dielectric loss factor ε'', and water-state observable T_2 — re-emerge here as the rheological-quality control variables of dysphagia-graded constructs and the structural-anisotropy control variables of plant-based meat analogues. The following section consolidates the overall trajectory of the field and identifies the principal research gaps that will determine the pace at which extrusion-based 3DFP moves from laboratory demonstration toward broad commercial deployment.

8. Summary and Future Perspectives

8.1 Summary

This review has traced the engineering trajectory of extrusion-based 3DFP within the material-extrusion category of ISO/ASTM 52900. Four differentiation axes organised the present treatment. First, a strict scope limitation to MEX excluded phase-change FDM, powder bed fusion, binder jetting, and material jetting from the analysis, yielding cross-domain depth at the cost of breadth. Second, a four-axis stimulus–response 4D matrix organised the post-deposition trajectory by mechanism rather than by phenomenon, with shape morphing, colour change, flavour and nutritional evolution, and synchronised multi-axis transformation treated as outputs of a common asymmetric-distribution design principle. Third, a three-axis intelligent process control framework integrated offline computational modelling, data-driven printability prediction, and real-time computer-vision feedback as components of a single closed-loop paradigm rather than as independent research streams. Fourth, a set of recurring physical observables — yield stress τ_y, dielectric loss factor ε'', NMR transverse relaxation time T_2, free-water mobility, and layer-image accuracy — was tracked across the ink-design, processing, and 4D-evolution domains, providing a unifying analytical thread across the review that prior treatments did not articulate. Table 1 (Section 1.3) provided the comparative analysis against prior reviews, demonstrating that no prior treatment, to the authors' knowledge, has integrated these four axes within a single narrative restricted to MEX. The integrated tables of the present review — Table 4 for post-processing release specifications and Table 5 for stimulus-responsive 4D studies — supplied the empirical scaffolding against which the four differentiation axes were operationalised.

8.2 Research Gaps and Future Perspectives

Despite the maturation documented above, several research gaps continue to limit the industrial deployment and clinical translation of extrusion-based 3DFP. Three integrated gap clusters are formulated below, each combining the gap identification with the corresponding addressing strategy within a single subsection. Table 6 consolidates the three clusters alongside their addressing strategies and cross-references to the relevant review sections.

8.2.1 Cross-material standardisation and composition-aware predictive frameworks

Cross-material standardisation is the foundational gap that limits both the reproducibility of extrusion-based 3DFP and the generalisation of its predictive frameworks. Unlike polymer and metal additive manufacturing, where

ACCEPTED PAPER

ISO/ASTM 52900 and parallel ASTM standards have established uniform terminology and process-parameter conventions, the food-printing literature lacks a comparable consensus across three interlocking layers: rheological benchmark specifications, process-parameter reference ranges, and printability assessment methods. Reported yield-stress, shear-thinning-index, and recovery-kinetics windows vary widely — τ_y = 200–1500 Pa, n = 0.15–0.7, and G'-recovery time τ_{rec} = 0.5–60 s have all been reported as "printable" depending on substrate and operator — and a single ink prepared by different laboratories yields different printability scores when assessed by different methods. The Herschel–Bulkley constitutive framework formalised by Outrequin et al. ($G' \geq 300$ Pa AND $\tan\delta \leq 0.268$ as the printable-zone criterion) offers a candidate baseline, but its biopolymer-specific validation has not been extended across the full range of food substrates [60].

Compounding this standardisation gap, composition-specific predictive frameworks currently treat the rheological, dielectric, and water-state observables one at a time, whereas food inks are inherently multi-component composites in which protein, starch, lipid, hydrocolloid, salt, water, and bioactive payload are co-formulated within a single deposited construct. CFD simulations vary nozzle geometry with fixed ink rheology, LF-NMR + BP-ANN models vary water-state distribution with fixed compositional families, and dielectric-loss models vary single-component ε'' with fixed matrix composition. The deep neural network of Cui et al., applied to starch-based gels to predict printability, texture, and extrusion force from compositional inputs [115], and the AI-AM benchmarking of Ma et al. across seven ML architectures on polysaccharide systems represent the early state of cross-axis prediction [171].

Addressing this combined gap requires a coordinated effort along three lines. First, a pharmacopoeia-style monograph for extrusion-based 3DFP should specify the rheological assay protocol, substrate-class parameter ranges, and the printability assessment battery with quantitative pass/fail criteria. Second, the next-generation predictive framework should integrate the compositional axes simultaneously, producing a single model that maps the full (rheology, ε'', T_2, oil affinity, bioactive payload) input vector to the full (printability, texture, post-processing trajectory, 4D response) output vector. Third, transfer-learning protocols and benchmark datasets spanning all major food-ink classes — analogous to the cross-material defect-prediction protocols emerging in laser additive manufacturing — would support the cross-material generalisation that single-substrate models cannot deliver. A further dimension that current predictive frameworks rarely incorporate is sensory validation: printability, texture, and 4D endpoints are characterised through physical observables, whereas consumer-facing sensory acceptability — palatability, mouthfeel, and, for dysphagia constructs, swallowing safety — is seldom embedded in the same predictive pipeline, and its inclusion would close the gap between physically optimised and consumer-deliverable constructs. The convergence of these three lines would resolve the standardisation–prediction gap as a single coordinated research effort.

8.2.2 Multi-sensor process analytical technology and proactive closed-loop control

The three-axis intelligent process control framework of Section 4 — offline modelling, data-driven prediction, real-time computer-vision feedback — operates today through largely independent sensor channels. CFD and FEM predictions provide pre-print rheological verification, LF-NMR + ML provides at-line printability classification within ~60 s, and machine-vision systems provide in-process geometric and defect feedback during deposition. The integration of these channels into a single multi-sensor process-analytical-technology framework, analogous to the multisensor-fusion paradigm that has emerged in laser additive manufacturing, remains an open research direction.

Compounding this fragmentation, most existing process-control strategies in extrusion-based 3DFP remain reactive: a defect is detected and the print is terminated or the relevant parameter is adjusted, but the post-deposition trajectory of the construct is not anticipated at the printing stage. The proactive paradigm, by contrast, would predict the full post-deposition trajectory — post-fry oil uptake, post-FD porosity, MW puffing direction and intensity, 4D shape-morphing trajectory under a specified stimulus — and adjust the ink composition, infill geometry, and printing-stage parameters to program a desired endpoint. Several studies reviewed in Sections 5 and 6 represent the early state

ACCEPTED PAPER

of this paradigm: bilayer drying-shrinkage anisotropy mapped to bending-angle endpoints [142]; surface-groove geometry mapped to twisting-angle endpoints [145]; a continuum-mechanics framework coupling mass transfer with large-deformation FEM for buckling-driven morphing prediction [149]; and synchronous colour + shape + flavour transformation within 45 s [156].

Addressing this combined gap requires the convergence of multi-sensor PAT integration and proactive endpoint prediction within a single architecture. The five PAT modalities matched to post-processing operations in Section 5.4 — NIR spectroscopy, hyperspectral imaging, machine vision, time-domain NMR, and acoustic-emission monitoring — should be integrated with offline-fitted endpoint-prediction models so that sensor-derived deviations trigger model retraining rather than reactive print termination. The recent demonstration by Lee et al. [124] of in-line graphene-IR heating coupled with feedforward AI control marks the first published convergence of the three intelligent-control axes within a single integrated print-and-cook system, and provides an operational template for the broader transition from reactive defect mitigation to proactive endpoint programming. Extension of this template across the full range of post-processing modalities reviewed in Section 5 would close the loop between the offline rheological framework, the cross-material AI/ML layer, and the real-time vision feedback layer.

8.2.3 Hierarchical multi-scale quality control and distributed regulatory translation

Quality control in extrusion-based 3DFP operates at multiple scales because different defect categories arise at different scales and time-points along the print-and-post chain. A four-level hierarchy adapted from the multi-scale defect-identification framework of laser additive manufacturing comprises molecular-scale quality (in vitro digestibility, bioactive retention, Maillard hazard formation, in situ photochemical conversion), micro-scale quality (porosity distribution, capillary structure, water-state distribution, interlaminar bonding microstructure), layer-wise quality (dimensional accuracy of each deposited layer, infill integrity, over- and under-extrusion defects), and construct-scale quality (total dimensional fidelity, IDDSI level compliance, colour stability across shelf life). Existing quality-control practice typically operates at one or two of these levels: dimensional accuracy is assessed at the construct scale, INFOGEST 2.0 in vitro digestion is assessed at the molecular scale, and layer-wise QC by image analysis is occasionally reported.

Outside the four-level QC hierarchy lies a regulatory and deployment gap that is essential for industrial translation. Extrusion-based 3D-printed foods are not yet covered by a unified regulatory category, and the safety, label-claim, and traceability requirements that apply to conventional manufactured foods must be reinterpreted for distributed, on-demand printing. The decentralised production model — printing at point-of-care for clinical nutrition, at point-of-sale for personalised consumer products, at point-of-mission for space and military applications — introduces quality-assurance challenges (batch-to-batch consistency, microbial contamination control, label-claim verification) that conventional centralised food regulation does not address. Sustainability, equipment and ingredient cost, scale, consumer acceptance, and digital-recipe intellectual property add further deployment-level constraints whose resolution falls outside the engineering scaffolding of this review.

Addressing this combined gap requires the integration of the four-level QC hierarchy with a deployment-level regulatory framework. The Codex / AOAC / ISO / IDDSI / INFOGEST-aligned release specification proposed in Table 4 (Section 5.4) provides the engineering scaffolding for such a framework; its extension along the four-level hierarchy and its formalisation as a regulatory monograph analogous to the European Pharmacopoeia treatment of 3D-printed solid dosage forms would translate Table 4 from a research baseline into a compliance specification. Coordinated action by regulatory bodies (Codex Alimentarius, FDA, EFSA), industry stakeholders, and the research community will be required to bring this framework into practice, with the present review able to provide only the engineering scaffolding on which such coordination can be built.

ACCEPTED PAPER

Table 6. Research gaps in extrusion-based 3D food printing, mapped to addressing strategy, related review section, and representative anchor references.

Research gap	Addressing strategy
8.2.1 Cross-material standardisation and composition-aware prediction	Pharmacopoeia-style monograph (assay protocol, substrate-class parameter ranges, pass/fail criteria); integrated (rheology + ε'' + T_2 + oil affinity + bioactive) → (printability + texture + post-processing + 4D) predictive vector model; transfer-learning protocols and benchmark datasets across major food-ink classes
8.2.2 Multi-sensor PAT and proactive closed-loop control	Five-modality PAT integration (NIR, hyperspectral, vision, LF-NMR, acoustic emission) with offline-fitted endpoint models; sensor-derived deviations trigger model retraining rather than reactive termination; extension from in-line print-and-cook demonstration [124] to full proactive endpoint programming
8.2.3 Hierarchical multi-scale QC and distributed regulatory translation	Four-level QC framework integration (molecular / micro / layer-wise / construct); Codex / AOAC / ISO / IDDSI / INFOGEST-aligned monograph formalisation; coordinated regulatory–industry–research action for distributed-printing deployment

ACCEPTED PAPER

Acknowledgments

None.

Funding

Following are results of study on the "Gyeongsangsam-do Regional Innovation System & Education (RISE)" Project, supported by the Ministry of Education and Gyeongsangnam-do. (1-1-1-1-7-9).

Conflict of interest

The authors declare that they have no known competing financial interests or personal relationships that could have appeared to influence the work reported in this paper.

Author contributions

Conceptualization: Sangjun Jeon, Ara Go, Seong Je Park

Funding acquisition: Seong Je Park

Investigation: Sangjun Jeon, Ara Go, Donghui Kim

Methodology: Donghui Kim, Seung Kim Moon

Supervision: Seung Kim Moon, Seong Je Park

Visualization: Sangjun Jeon, Ara Go

Writing – original draft: Sangjun Jeon, Ara Go

Writing – review & editing: Seung Kim Moon, Seong Je Park

Ethics approval and consent to participate

Not applicable.

ACCEPTED PAPER

Consent for publication

Not applicable.

Availability of data

Not applicable.

Further disclosure

During the preparation of this work the authors used Claude (Anthropic) to assist with language editing and to improve the readability of the manuscript. The schematic figures presented in this review were generated with the assistance of the in-house "paperbanana" generative-AI code developed by the authors.

ACCEPTED PAPER

References

[1] Thorakkattu P, Awasti N, Sajith Babu K, Khanashyam AC, Deliephan A, Shah K, et al. 3D printing: trends and approaches toward achieving long-term sustainability in the food industry. Critical Reviews in Biotechnology 2025;45:48–68. https://doi.org/10.1080/07388551.2024.2344577.

[2] ISO/ASTM 52900:2021(en), Additive manufacturing — General principles — Fundamentals and vocabulary n.d. https://www.iso.org/obp/ui/#iso:std:iso-astm:52900:ed-2:v1:en (accessed June 8, 2026).

[3] Lille M, Nurmela A, Nordlund E, Metsä-Kortelainen S, Sozer N. Applicability of protein and fiber-rich food materials in extrusion-based 3D printing. Journal of Food Engineering 2018;220:20–7. https://doi.org/10.1016/j.jfoodeng.2017.04.034.

[4] Pallottino F, Hakola L, Costa C, Antonucci F, Figorilli S, Seisto A, et al. Printing on Food or Food Printing: a Review. Food Bioprocess Technol 2016;9:725–33. https://doi.org/10.1007/s11947-016-1692-3.

[5] Vadodaria S, Mills T. Jetting-based 3D printing of edible materials. Food Hydrocolloids 2020;106:105857. https://doi.org/10.1016/j.foodhyd.2020.105857.

[6] Sun J, Zhou W, Huang D, Fuh JYH, Hong GS. An Overview of 3D Printing Technologies for Food Fabrication. Food Bioprocess Technol 2015;8:1605–15. https://doi.org/10.1007/s11947-015-1528-6.

[7] Sun J, Zhou W, Yan L, Huang D, Lin L. Extrusion-based food printing for digitalized food design and nutrition control. Journal of Food Engineering 2018;220:1–11. https://doi.org/10.1016/j.jfoodeng.2017.02.028.

[8] Godoi FC, Prakash S, Bhandari BR. 3d printing technologies applied for food design: Status and prospects. Journal of Food Engineering 2016;179:44–54. https://doi.org/10.1016/j.jfoodeng.2016.01.025.

[9] Shen D, Zhang M, Mujumdar AS, Li J. Advances and application of efficient physical fields in extrusion based 3D food printing technology. Trends in Food Science & Technology 2023;131:104–17. https://doi.org/10.1016/j.tifs.2022.11.017.

[10] Caulier S, Doets E, Noort M. An exploratory consumer study of 3D printed food perception in a real-life military setting. Food Quality and Preference 2020;86:104001. https://doi.org/10.1016/j.foodqual.2020.104001.

[11] Tang T, Zhang M, Bhandari B, Li C. Personalized transformation of 3D printing for traditional multi-material food with stuffing：A review. Food Bioscience 2024;59:104112. https://doi.org/10.1016/j.fbio.2024.104112.
[12] Teng X, Li C, Mujumdar AS, Zhang M. Progress in Extrusion-Based Food Printing Technology for Enhanced Printability and Printing Efficiency of Typical Personalized Foods: A Review. Foods 2022;11:4111. https://doi.org/10.3390/foods11244111.
[13] Zhang JY, Pandya JK, McClements DJ, Lu J, Kinchla AJ. Advancements in 3D food printing: a comprehensive overview of properties and opportunities. Critical Reviews in Food Science and Nutrition 2022;62:4752–68. https://doi.org/10.1080/10408398.2021.1878103.
[14] Wang M, Li D, Zang Z, Sun X, Tan H, Si X, et al. 3D food printing: Applications of plant-based materials in extrusion-based food printing. Critical Reviews in Food Science and Nutrition 2022;62:7184–98. https://doi.org/10.1080/10408398.2021.1911929.
[15] Lee SH, Kim HW, Park HJ. Integrated design of micro-fibrous food with multi-materials fabricated by uniaxial 3D printing. Food Research International 2023;165:112529. https://doi.org/10.1016/j.foodres.2023.112529.
[16] Phuhongsung P, Zhang M, Bhandari B. 4D printing of products based on soy protein isolate via microwave heating for flavor development. Food Research International 2020;137:109605. https://doi.org/10.1016/j.foodres.2020.109605.
[17] Raja V, Nimbkar S, Moses JA, Ramachandran Nair SV, Anandharamakrishnan C. Modeling and Simulation of 3D Food Printing Systems—Scope, Advances, and Challenges. Foods 2023;12:3412. https://doi.org/10.3390/foods12183412.
[18] Chen F, Zhang M, Liu Z, Bhandari B. 4D deformation based on double-layer structure of the pumpkin/paper. Food Structure 2021;27:100168. https://doi.org/10.1016/j.foostr.2020.100168.
[19] Jeon S, Park SJ, Moon SK, Yang D. End-to-end processing of recycled carbon fiber composites: From waste hydrogen tanks to mechanically enhanced additive-manufactured components. Chemical Engineering Journal 2025;525:169661. https://doi.org/10.1016/j.cej.2025.169661.
[20] Jeon S, Kim J, Go A, Choi JP, Yang D, Moon SK. AI-Based Mechanical Properties Prediction of Sintering-Aging Combined Effect in Metal-Material Extrusion. Int J of Precis Eng and Manuf-Green Tech 2026. https://doi.org/10.1007/s40684-025-00826-w.
[21] Jeon S, Park ,Seong Je, Moon ,Seung Ki, and Yang D. Enhanced mechanical properties and reduced anisotropy of material extrusion-manufactured short carbon fibre-reinforced plastic via cold isostatic pressing. Virtual and Physical Prototyping 2025;20:e2499934. https://doi.org/10.1080/17452759.2025.2499934.
[22] Hao L, Mellor S, Seaman O, Henderson J, Sewell N, Sloan M. Material characterisation and process development for chocolate additive layer manufacturing. Virtual and Physical Prototyping 2010;5:57–64. https://doi.org/10.1080/17452751003753212.
[23] Lanaro M, Forrestal DP, Scheurer S, Slinger DJ, Liao S, Powell SK, et al. 3D printing complex chocolate objects: Platform design, optimization and evaluation. Journal of Food Engineering 2017;215:13–22. https://doi.org/10.1016/j.jfoodeng.2017.06.029.
[24] Mantihal S, Prakash S, Godoi FC, Bhandari B. Optimization of chocolate 3D printing by correlating thermal and flow properties with 3D structure modeling. Innovative Food Science & Emerging Technologies 2017;44:21–9. https://doi.org/10.1016/j.ifset.2017.09.012.
[25] Mantihal S, Prakash S, Godoi FC, Bhandari B. Effect of additives on thermal, rheological and tribological properties of 3D printed dark chocolate. Food Research International 2019;119:161–9. https://doi.org/10.1016/j.foodres.2019.01.056.
[26] Karyappa R, Hashimoto M. Chocolate-based Ink Three-dimensional Printing (Ci3DP). Sci Rep 2019;9:14178. https://doi.org/10.1038/s41598-019-50583-5.

ACCEPTED PAPER

[27] Liu Z, Zhang M, Bhandari B, Yang C. Impact of rheological properties of mashed potatoes on 3D printing. Journal of Food Engineering 2018;220:76–82. https://doi.org/10.1016/j.jfoodeng.2017.04.017.
[28] Zhu S, Stieger MA, Van Der Goot AJ, Schutyser MAI. Extrusion-based 3D printing of food pastes: Correlating rheological properties with printing behaviour. Innovative Food Science & Emerging Technologies 2019;58:102214. https://doi.org/10.1016/j.ifset.2019.102214.
[29] Guo Z, Arslan M, Li Z, Cen S, Shi J, Huang X, et al. Application of Protein in Extrusion-Based 3D Food Printing: Current Status and Prospectus. Foods 2022;11:1902. https://doi.org/10.3390/foods11131902.
[30] Hussain S, Malakar S, Arora VK. Extrusion-Based 3D Food Printing: Technological Approaches, Material Characteristics, Printing Stability, and Post-processing. Food Eng Rev 2022;14:100–19. https://doi.org/10.1007/s12393-021-09293-w.
[31] Kadival A, Kour M, Meena D, Mitra J. Extrusion-Based 3D Food Printing: Printability Assessment and Improvement Techniques. Food Bioprocess Technol 2023;16:987–1008. https://doi.org/10.1007/s11947-022-02931-z.
[32] Lazou AE. Food extrusion: An advanced process for innovation and novel product development. Critical Reviews in Food Science and Nutrition 2024;64:4532–60. https://doi.org/10.1080/10408398.2022.2143474.
[33] Voon SL, An J, Wong G, Zhang Y, Chua CK. 3D food printing: a categorised review of inks and their development. Virtual and Physical Prototyping 2019;14:203–18. https://doi.org/10.1080/17452759.2019.1603508.
[34] Tejada-Ortigoza V, Cuan-Urquizo E. Towards the Development of 3D-Printed Food: A Rheological and Mechanical Approach. Foods 2022;11:1191. https://doi.org/10.3390/foods11091191.
[35] Outrequin TCR, Gamonpilas C, Siriwatwechakul W, Sreearunothai P. Extrusion-based 3D printing of food biopolymers: A highlight on the important rheological parameters to reach printability. Journal of Food Engineering 2023;342:111371. https://doi.org/10.1016/j.jfoodeng.2022.111371.
[36] Raut S, Pawase PA, Khalid S, Shingote AB, Pathare AM, Rout S, et al. Recent advances in 3D food printing: A critical review of emerging technologies, material innovations, and novel applications. Applied Food Research 2026;6:101773. https://doi.org/10.1016/j.afres.2026.101773.
[37] Chauhan P, Kaushal M, Vaidya D, Gupta A, Kashyap S, Suthar P. Personalized nutrition to intelligent foods with 3D and 4D printing. Applied Food Research 2025;5:100863. https://doi.org/10.1016/j.afres.2025.100863.
[38] Seol J, Kim J, Hong Y, Cha M, Park S, Jang K-J, et al. Toward intelligent 3D food printing: a review on the perspective of materials, fabrication, monitoring, and control. Critical Reviews in Food Science and Nutrition 2026;66:1012–43. https://doi.org/10.1080/10408398.2025.2538546.
[39] S T, Arora VK, Prithviraj V. Printability Assessment and Optimization of Process Parameters for 3D Printing of Rice Flour and Jaggery Paste. J Biosyst Eng 2022;47:248–62. https://doi.org/10.1007/s42853-022-00143-z.
[40] Thangalakshmi S, Arora VK, Kaur BP, Malakar S. Investigation on rice flour and jaggery paste as food material for extrusion-based 3D printing. J Food Process Preserv 2021;45. https://doi.org/10.1111/jfpp.15375.
[41] Wang L, Zhang M, Bhandari B, Yang C. Investigation on fish surimi gel as promising food material for 3D printing. Journal of Food Engineering 2018;220:101–8. https://doi.org/10.1016/j.jfoodeng.2017.02.029.
[42] Derossi A, Paolillo M, Caporizzi R, Severini C. Extending the 3D food printing tests at high speed. Material deposition and effect of non-printing movements on the final quality of printed structures. Journal of Food Engineering 2020;275:109865. https://doi.org/10.1016/j.jfoodeng.2019.109865.

ACCEPTED PAPER

[43] In J, Jeong H, Song S, Min SC. Determination of Material Requirements for 3D Gel Food Printing Using a Fused Deposition Modeling 3D Printer. Foods 2021;10:2272. https://doi.org/10.3390/foods10102272.
[44] Dick A, Bhandari B, Dong X, Prakash S. Feasibility study of hydrocolloid incorporated 3D printed pork as dysphagia food. Food Hydrocolloids 2020;107:105940. https://doi.org/10.1016/j.foodhyd.2020.105940.
[45] Liu Y, Sun Q, Wei S, Xia Q, Pan Y, Liu S, et al. LF-NMR as a tool for predicting the 3D printability of surimi-starch systems. Food Chemistry 2022;374:131727. https://doi.org/10.1016/j.foodchem.2021.131727.
[46] Oyinloye TM, Yoon WB. Stability of 3D printing using a mixture of pea protein and alginate: Precision and application of additive layer manufacturing simulation approach for stress distribution. Journal of Food Engineering 2021;288:110127. https://doi.org/10.1016/j.jfoodeng.2020.110127.
[47] Venkatachalam A, Balasubramaniam A, Wilms PFC, Zhang L, Schutyser MAI. Impact of varying macronutrient composition on the printability of pea-based inks in extrusion-based 3D food printing. Food Hydrocolloids 2023;142:108760. https://doi.org/10.1016/j.foodhyd.2023.108760.
[48] Dong X, Pan Y, Zhao W, Huang Y, Qu W, Pan J, et al. Impact of microbial transglutaminase on 3D printing quality of Scomberomorus niphonius surimi. LWT 2020;124:109123. https://doi.org/10.1016/j.lwt.2020.109123.
[49] Chen H, Zhang M, Rao Z. Effect of ultrasound-assisted thawing on gelling and 3D printing properties of silver carp surimi. Food Research International 2021;145:110405. https://doi.org/10.1016/j.foodres.2021.110405.
[50] Liu Z, Dick A, Prakash S, Bhandari B, Zhang M. Texture Modification of 3D Printed Air-Fried Potato Snack by Varying Its Internal Structure with the Potential to Reduce Oil Content. Food Bioprocess Technol 2020;13:564–76. https://doi.org/10.1007/s11947-020-02408-x.
[51] Teng X, Zhang M, Mujumdar AS. Strategies for controlling over-puffing of 3D-printed potato gel during microwave processing. LWT 2022;153:112508. https://doi.org/10.1016/j.lwt.2021.112508.
[52] Liu Z, Bhandari B, Prakash S, Mantihal S, Zhang M. Linking rheology and printability of a multicomponent gel system of carrageenan-xanthan-starch in extrusion based additive manufacturing. Food Hydrocolloids 2019;87:413–24. https://doi.org/10.1016/j.foodhyd.2018.08.026.
[53] Guo C, Zhang M, Devahastin S. 3D extrusion-based printability evaluation of selected cereal grains by computational fluid dynamic simulation. Journal of Food Engineering 2020;286:110113. https://doi.org/10.1016/j.jfoodeng.2020.110113.
[54] Kadival A, Mitra J, Machavaram R, Kaushal M. 3D printing of rice starch incorporated peanut protein isolate paste: Rheological characterization and simulation of flow properties. Innovative Food Science & Emerging Technologies 2024;94:103669. https://doi.org/10.1016/j.ifset.2024.103669.
[55] Liu Q, Zhang N, Wei W, Hu X, Tan Y, Yu Y, et al. Assessing the dynamic extrusion-based 3D printing process for power-law fluid using numerical simulation. Journal of Food Engineering 2020;275:109861. https://doi.org/10.1016/j.jfoodeng.2019.109861.
[56] Liu Z, Zhang M, Ye Y. Indirect prediction of 3D printability of mashed potatoes based on LF-NMR measurements. Journal of Food Engineering 2020;287:110137. https://doi.org/10.1016/j.jfoodeng.2020.110137.
[57] Chen H, Zhang M, Yang C. Comparative analysis of 3D printability and rheological properties of surimi gels via LF-NMR and dielectric characteristics. Journal of Food Engineering 2021;292:110278. https://doi.org/10.1016/j.jfoodeng.2020.110278.
[58] Guo C, Zhang M, Chen H. Suitability of low-field nuclear magnetic resonance (LF-NMR) combining with back propagation artificial neural network (BP-ANN) to predict printability of

ACCEPTED PAPER

polysaccharide hydrogels 3D printing. Int J of Food Sci Tech 2021;56:2264–72. https://doi.org/10.1111/ijfs.14844.
[59] Jiao X, Ren G, Law CL, Li L, Cao W, Luo Z, et al. Novel strategy for optimizing of corn starch-based ink food 3D printing process: Printability prediction based on BP-ANN model. International Journal of Biological Macromolecules 2024;276:133921. https://doi.org/10.1016/j.ijbiomac.2024.133921.
[60] Outrequin TCR, Gamonpilas C, Sreearunothai P, Deepaisarn S, Siriwatwechakul W. Machine learning assisted evaluation of the filament spreading during extrusion-based 3D food printing: Impact of the rheological and printing parameters. Journal of Food Engineering 2024;381:112166. https://doi.org/10.1016/j.jfoodeng.2024.112166.
[61] Pan Y, Sun Q, Liu Y, Wei S, Xia Q, Zheng O, et al. The relationship between rheological and textural properties of shrimp surimi adding starch and 3D printability based on principal component analysis. Food Science & Nutrition 2021;9:2985–99. https://doi.org/10.1002/fsn3.2257.
[62] Kim SM, Wen Y, Kim HW, Park HJ. Textural and sensory qualities of low-calorie surimi with carrageenan inserted as a protein substitute using coaxial extrusion 3D food printing. Journal of Food Engineering 2022;333:111141. https://doi.org/10.1016/j.jfoodeng.2022.111141.
[63] Xie Y, Yu X, Wang Y, Yu C, Prakash S, Zhu B, et al. Role of dietary fiber and flaxseed oil in altering the physicochemical properties and 3D printability of cod protein composite gel. Journal of Food Engineering 2022;327:111053. https://doi.org/10.1016/j.jfoodeng.2022.111053.
[64] Kim SM, Kim HW, Park HJ. Preparation and characterization of surimi-based imitation crab meat using coaxial extrusion three-dimensional food printing. Innovative Food Science & Emerging Technologies 2021;71:102711. https://doi.org/10.1016/j.ifset.2021.102711.
[65] Dick A, Bhandari B, Prakash S. Printability and textural assessment of modified-texture cooked beef pastes for dysphagia patients. Future Foods 2021;3:100006. https://doi.org/10.1016/j.fufo.2020.100006.
[66] Wilson A, Anukiruthika T, Moses JA, Anandharamakrishnan C. Customized Shapes for Chicken Meat–Based Products: Feasibility Study on 3D-Printed Nuggets. Food Bioprocess Technol 2020;13:1968–83. https://doi.org/10.1007/s11947-020-02537-3.
[67] Park JW, Lee SH, Kim HW, Park HJ. Application of extrusion-based 3D food printing to regulate marbling patterns of restructured beef steak. Meat Science 2023;202:109203. https://doi.org/10.1016/j.meatsci.2023.109203.
[68] Hussain S, Arora VK, Malakar S. Formulation of protein-enriched 3D printable food matrix and evaluation of textural, rheological characteristics, and printing stability. J Food Process Preserv 2021;45. https://doi.org/10.1111/jfpp.15182.
[69] Ma Y, Schutyser MAI, Boom RM, Zhang L. Thermographic and rheological characterization of viscoelastic materials for hot-extrusion 3D food printing. Innovative Food Science & Emerging Technologies 2022;81:103135. https://doi.org/10.1016/j.ifset.2022.103135.
[70] Xu L, Gu L, Su Y, Chang C, Wang J, Dong S, et al. Impact of thermal treatment on the rheological, microstructural, protein structures and extrusion 3D printing characteristics of egg yolk. Food Hydrocolloids 2020;100:105399. https://doi.org/10.1016/j.foodhyd.2019.105399.
[71] Bareen MA, Joshi S, Sahu JK, Prakash S, Bhandari B. Assessment of 3D printability of heat acid coagulated milk semi-solids 'soft cheese' by correlating rheological, microstructural, and textural properties. Journal of Food Engineering 2021;300:110506. https://doi.org/10.1016/j.jfoodeng.2021.110506.
[72] Joshi S, Sahu JK, Bareen MA, Prakash S, Bhandari B, Sharma N, et al. Assessment of 3D printability of composite dairy matrix by correlating with its rheological properties. Food Research International 2021;141:110111. https://doi.org/10.1016/j.foodres.2021.110111.

ACCEPTED PAPER

[73] Anukiruthika T, Moses JA, Anandharamakrishnan C. 3D printing of egg yolk and white with rice flour blends. Journal of Food Engineering 2020;265:109691. https://doi.org/10.1016/j.jfoodeng.2019.109691.
[74] Phuhongsung P, Zhang M, Devahastin S. Investigation on 3D printing ability of soybean protein isolate gels and correlations with their rheological and textural properties via LF-NMR spectroscopic characteristics. LWT 2020;122:109019. https://doi.org/10.1016/j.lwt.2020.109019.
[75] Phuhongsung P, Zhang M, Devahastin S. Influence of Surface pH on Color, Texture and Flavor of 3D Printed Composite Mixture of Soy Protein Isolate, Pumpkin, and Beetroot. Food Bioprocess Technol 2020;13:1600–10. https://doi.org/10.1007/s11947-020-02497-8.
[76] Chen J, Sun H, Mu T, Blecker C, Richel A, Richard G, et al. Effect of temperature on rheological, structural, and textural properties of soy protein isolate pastes for 3D food printing. Journal of Food Engineering 2022;323:110917. https://doi.org/10.1016/j.jfoodeng.2021.110917.
[77] Fan H, Zhang M, Liu Z, Ye Y. Effect of microwave-salt synergetic pre-treatment on the 3D printing performance of SPI-strawberry ink system. LWT 2020;122:109004. https://doi.org/10.1016/j.lwt.2019.109004.
[78] Yu J, Wang X, Li D, Wang L, Wang Y. Development of soy protein isolate emulsion gels as extrusion-based 3D food printing inks: Effect of polysaccharides incorporation. Food Hydrocolloids 2022;131:107824. https://doi.org/10.1016/j.foodhyd.2022.107824.
[79] Wang S, Liu S. 3D Printing of Soy Protein- and Gluten-Based Gels Facilitated by Thermosensitive Cocoa Butter in a Model Study. ACS Food Sci Technol 2021;1:1990–6. https://doi.org/10.1021/acsfoodscitech.1c00311.
[80] Feng T, Fan C, Wang X, Wang X, Xia S, Huang Q. Food-grade Pickering emulsions and high internal phase Pickering emulsions encapsulating cinnamaldehyde based on pea protein-pectin-EGCG complexes for extrusion 3D printing. Food Hydrocolloids 2022;124:107265. https://doi.org/10.1016/j.foodhyd.2021.107265.
[81] Kim Y, Kim HW, Park HJ. Effect of pea protein isolate incorporation on 3D printing performance and tailing effect of banana paste. LWT 2021;150:111916. https://doi.org/10.1016/j.lwt.2021.111916.
[82] Sun Y, Zhang M, Chen H. LF-NMR intelligent evaluation of rheology and printability for 3D printing of cookie dough pretreated by microwave. LWT 2020;132:109752. https://doi.org/10.1016/j.lwt.2020.109752.
[83] Habuš M, Golubić P, Vukušić Pavičić T, Čukelj Mustač N, Voučko B, Herceg Z, et al. Influence of Flour Type, Dough Acidity, Printing Temperature and Bran Pre-processing on Browning and 3D Printing Performance of Snacks. Food Bioprocess Technol 2021;14:2365–79. https://doi.org/10.1007/s11947-021-02732-w.
[84] Liu Y, Tang T, Duan S, Qin Z, Li C, Zhang Z, et al. Effects of sodium alginate and rice variety on the physicochemical characteristics and 3D printing feasibility of rice paste. LWT 2020;127:109360. https://doi.org/10.1016/j.lwt.2020.109360.
[85] Liu Y, Tang T, Duan S, Qin Z, Zhao H, Wang M, et al. Applicability of Rice Doughs as Promising Food Materials in Extrusion-Based 3D Printing. Food Bioprocess Technol 2020;13:548–63. https://doi.org/10.1007/s11947-020-02415-y.
[86] Fahmy AR, Becker T, Jekle M. 3D printing and additive manufacturing of cereal-based materials: Quality analysis of starch-based systems using a camera-based morphological approach. Innovative Food Science & Emerging Technologies 2020;63:102384. https://doi.org/10.1016/j.ifset.2020.102384.
[87] Huang M, Zhang M, Guo C. 3D printability of brown rice gel modified by some food hydrocolloids. J Food Process Preserv 2020;44. https://doi.org/10.1111/jfpp.14502.

ACCEPTED PAPER

[88] Guo C, Zhang M, Devahastin S. Improvement of 3D printability of buckwheat starch-pectin system via synergistic Ca2+-microwave pretreatment. Food Hydrocolloids 2021;113:106483. https://doi.org/10.1016/j.foodhyd.2020.106483.
[89] Xu K, Zhang M, Bhandari B. Effect of Novel Ultrasonic- Microwave Combined Pretreatment on the Quality of 3D Printed Wheat Starch-Papaya System. Food Biophysics 2020;15:249–60. https://doi.org/10.1007/s11483-019-09615-w.
[90] Liu Z, Chen H, Zheng B, Xie F, Chen L. Understanding the structure and rheological properties of potato starch induced by hot-extrusion 3D printing. Food Hydrocolloids 2020;105:105812. https://doi.org/10.1016/j.foodhyd.2020.105812.
[91] Maniglia BC, Pataro G, Ferrari G, Augusto PED, Le-Bail P, Le-Bail A. Pulsed electric fields (PEF) treatment to enhance starch 3D printing application: Effect on structure, properties, and functionality of wheat and cassava starches. Innovative Food Science & Emerging Technologies 2021;68:102602. https://doi.org/10.1016/j.ifset.2021.102602.
[92] Maniglia BC, Lima DC, Matta Junior MD, Le-Bail P, Le-Bail A, Augusto PED. Preparation of cassava starch hydrogels for application in 3D printing using dry heating treatment (DHT): A prospective study on the effects of DHT and gelatinization conditions. Food Research International 2020;128:108803. https://doi.org/10.1016/j.foodres.2019.108803.
[93] Ma S, Liu J, Zhang Q, Lin Q, Liu R, Xing Y, et al. 3D printing performance using radio frequency electromagnetic wave modified potato starch. Innovative Food Science & Emerging Technologies 2022;80:103064. https://doi.org/10.1016/j.ifset.2022.103064.
[94] Feng C, Zhang M, Bhandari B, Ye Y. Use of potato processing by-product: Effects on the 3D printing characteristics of the yam and the texture of air-fried yam snacks. LWT 2020;125:109265. https://doi.org/10.1016/j.lwt.2020.109265.
[95] Feng C, Zhang M, Liu Z, Mujumdar A, Wang Y, Chang L. Effect of drying method on post-processing stability and quality of 3D printed rose-yam paste. Drying Technology 2021;39:1196–204. https://doi.org/10.1080/07373937.2020.1851708.
[96] Shi Y, Zhang M, Bhandari B. Effect of addition of beeswax based oleogel on 3D printing of potato starch-protein system. Food Structure 2021;27:100176. https://doi.org/10.1016/j.foostr.2021.100176.
[97] Feng L, Wu J, Song J, Li D, Zhang Z, Xu Y, et al. Effect of particle size distribution on the carotenoids release, physicochemical properties and 3D printing characteristics of carrot pulp. LWT 2021;139:110576. https://doi.org/10.1016/j.lwt.2020.110576.
[98] Park SM, Kim HW, Park HJ. Callus-based 3D printing for food exemplified with carrot tissues and its potential for innovative food production. Journal of Food Engineering 2020;271:109781. https://doi.org/10.1016/j.jfoodeng.2019.109781.
[99] Jo GH, Lim WS, Kim HW, Park HJ. Post-processing and printability evaluation of red ginseng snacks for three-dimensional (3D) printing. Food Bioscience 2021;42:101094. https://doi.org/10.1016/j.fbio.2021.101094.
[100] Keerthana K, Anukiruthika T, Moses JA, Anandharamakrishnan C. Development of fiber-enriched 3D printed snacks from alternative foods: A study on button mushroom. Journal of Food Engineering 2020;287:110116. https://doi.org/10.1016/j.jfoodeng.2020.110116.
[101] Xing X, Chitrakar B, Hati S, Xie S, Li H, Li C, et al. Development of black fungus-based 3D printed foods as dysphagia diet: Effect of gums incorporation. Food Hydrocolloids 2022;123:107173. https://doi.org/10.1016/j.foodhyd.2021.107173.
[102] Liu Z, Bhandari B, Guo C, Zheng W, Cao S, Lu H, et al. 3D Printing of Shiitake Mushroom Incorporated with Gums as Dysphagia Diet. Foods 2021;10:2189. https://doi.org/10.3390/foods10092189.

ACCEPTED PAPER

[103] Pant A, Lee AY, Karyappa R, Lee CP, An J, Hashimoto M, et al. 3D food printing of fresh vegetables using food hydrocolloids for dysphagic patients. Food Hydrocolloids 2021;114:106546. https://doi.org/10.1016/j.foodhyd.2020.106546.
[104] Liu L, Ciftci ON. Effects of high oil compositions and printing parameters on food paste properties and printability in a 3D printing food processing model. Journal of Food Engineering 2021;288:110135. https://doi.org/10.1016/j.jfoodeng.2020.110135.
[105] Wang M, Lu X, Zheng X, Li W, Wang L, Qian Y, et al. Rheological and physicochemical properties of Spirulina platensis residues-based inks for extrusion 3D food printing. Food Research International 2023;169:112823. https://doi.org/10.1016/j.foodres.2023.112823.
[106] Liu Y, Yi S, Ye T, Leng Y, Alomgir Hossen M, Sameen DE, et al. Effects of ultrasonic treatment and homogenization on physicochemical properties of okara dietary fibers for 3D printing cookies. Ultrasonics Sonochemistry 2021;77:105693. https://doi.org/10.1016/j.ultsonch.2021.105693.
[107] Lee CP, Takahashi M, Arai S, Lee C-LK, Hashimoto M. 3D Printing of *Okara* Ink: The Effect of Particle Size on the Printability. ACS Food Sci Technol 2021;1:2053–61. https://doi.org/10.1021/acsfoodscitech.1c00236.
[108] Liu Z, Bhandari B, Zhang M. Incorporation of probiotics (Bifidobacterium animalis subsp. Lactis) into 3D printed mashed potatoes: Effects of variables on the viability. Food Research International 2020;128:108795. https://doi.org/10.1016/j.foodres.2019.108795.
[109] Kuo C-C, Clark S, Qin H, Shi X. Development of a shelf-stable, gel-based delivery system for probiotics by encapsulation, 3D printing, and freeze-drying. LWT 2022;157:113075. https://doi.org/10.1016/j.lwt.2022.113075.
[110] Yoha KS, Anukiruthika T, Anila W, Moses JA, Anandharamakrishnan C. 3D printing of encapsulated probiotics: Effect of different post-processing methods on the stability of Lactiplantibacillus plantarum (NCIM 2083) under static in vitro digestion conditions and during storage. LWT 2021;146:111461. https://doi.org/10.1016/j.lwt.2021.111461.
[111] Vieira MV, Oliveira SM, Amado IR, Fasolin LH, Vicente AA, Pastrana LM, et al. 3D printed functional cookies fortified with Arthrospira platensis: Evaluation of its antioxidant potential and physical-chemical characterization. Food Hydrocolloids 2020;107:105893. https://doi.org/10.1016/j.foodhyd.2020.105893.
[112] Ning X, Devahastin S, Wang X, Wu N, Liu Z, Gong Y, et al. Understanding 3D food printing through computer simulation and extrusion force analysis. Journal of Food Engineering 2024;370:111972. https://doi.org/10.1016/j.jfoodeng.2024.111972.
[113] Ju E, Seol J, Kim S, Kim S, Kim S-J, Son HI. Comparison of deep learning models for 3D food printing monitoring system. Journal of Food Engineering 2026;409:112903. https://doi.org/10.1016/j.jfoodeng.2025.112903.
[114] Ma Y, Schutyser MAI, Boom RM, Zhang L. Predicting the extrudability of complex food materials during 3D printing based on image analysis and gray-box data-driven modelling. Innovative Food Science & Emerging Technologies 2021;73:102764. https://doi.org/10.1016/j.ifset.2021.102764.
[115] Cui S, Cui Y, Blennow A, Zhong Y, Liu X. Artificial intelligence-driven pre-estimation of printability and textural properties of starch-based gels in 3D food printing. Food Hydrocolloids 2026;175:112422. https://doi.org/10.1016/j.foodhyd.2026.112422.
[116] Maldonado-Rosas R, Alfaro-Ponce M, Cuan-Urquizo E, Tejada-Ortigoza V. Printability prediction of food formulations for 3D printing using a Gaussian process regression model. Journal of Food Engineering 2025;395:112534. https://doi.org/10.1016/j.jfoodeng.2025.112534.
[117] Lu Y, Rai R, Nitin N. Image-based assessment and machine learning-enabled prediction of printability of polysaccharides-based food ink for 3D printing. Food Research International 2023;173:113384. https://doi.org/10.1016/j.foodres.2023.113384.

ACCEPTED PAPER

[118] Tang T, Zhang M, Adhikari B, Li C, Lin J. Indirect prediction of the 3D printability of polysaccharide gels using multiple machine learning (ML) models. International Journal of Biological Macromolecules 2024;280:135769. https://doi.org/10.1016/j.ijbiomac.2024.135769.
[119] Chen J, Kong Y, Huang Q. Analysis of surimi extrusion behavior during 3D printing by modified Computational Fluid Dynamics (CFD) and quick prediction of printability using machine learning based on texture data. Innovative Food Science & Emerging Technologies 2024;94:103698. https://doi.org/10.1016/j.ifset.2024.103698.
[120] Lee D, Jeong S, Yun S, Lee S. Artificial intelligence-based prediction of the rheological properties of hydrocolloids for plant-based meat analogues. J Sci Food Agric 2024;104:5114–23. https://doi.org/10.1002/jsfa.13334.
[121] Zhang Q, Chen Y, Zhou A, Ma M, Zhou L, Shi H, et al. An end-to-end AI framework for data-driven evaluation and optimisation of direct ink writing-based 3D printing. Virtual and Physical Prototyping 2025;20:e2584948. https://doi.org/10.1080/17452759.2025.2584948.
[122] Ma Y, Potappel J, Schutyser MAI, Boom RM, Zhang L. Quantitative analysis of 3D food printing layer extrusion accuracy: Contextualizing automated image analysis with human evaluations: Quantifying 3D food printing accuracy. Current Research in Food Science 2023;6:100511. https://doi.org/10.1016/j.crfs.2023.100511.
[123] Ma Y, Potappel J, Chauhan A, Schutyser MAI, Boom RM, Zhang L. Improving 3D food printing performance using computer vision and feedforward nozzle motion control. Journal of Food Engineering 2023;339:111277. https://doi.org/10.1016/j.jfoodeng.2022.111277.
[124] Lee CKW, Xu Y, Yuan Q, Chan YH, Poon WY, Zhong H, et al. Advanced 3D Food Printing with Simultaneous Cooking and Generative AI Design. Advanced Materials 2025;37:2408282. https://doi.org/10.1002/adma.202408282.
[125] Bhandarkar VV, Das B, Tandon P. Real-time remote monitoring and defect detection in smart additive manufacturing for reduced material wastage. Measurement 2025;252:117362. https://doi.org/10.1016/j.measurement.2025.117362.
[126] Tan JS, Ng WL. 3D Printing of Salmon Sashimi Analogues Using Fish-Derived Food Inks: Printability, Texture, and Nutritional Evaluation. Food Bioprocess Technol 2025;18:8539–53. https://doi.org/10.1007/s11947-025-03943-1.
[127] Bhuiyan MdHR, Yeasmen N, Ngadi M. Effect of food hydrocolloids on 3D meat-analog printing and deep-fat-frying. Food Hydrocolloids 2025;159:110716. https://doi.org/10.1016/j.foodhyd.2024.110716.
[128] Guénard-Lampron V, Masson M, Leichtnam O, Blumenthal D. Impact of 3D printing and post-processing parameters on shape, texture and microstructure of carrot appetizer cake. Innovative Food Science & Emerging Technologies 2021;72:102738. https://doi.org/10.1016/j.ifset.2021.102738.
[129] Severini C, Azzollini D, Albenzio M, Derossi A. On printability, quality and nutritional properties of 3D printed cereal based snacks enriched with edible insects. Food Research International 2018;106:666–76. https://doi.org/10.1016/j.foodres.2018.01.034.
[130] Kewuyemi YO, Kesa H, Meijboom R, Alimi OA, Adebo OA. 3D food printing improves color profile and structural properties of the derived novel whole-grain sourdough and malt biscuits. Sci Rep 2022;12:12347. https://doi.org/10.1038/s41598-022-16659-5.
[131] Venkatachalam A, Wilms PFC, Patón Baeza J, Schutyser MAI, Zhang L. Formulation of pea-based inks with different starches to produce customized 3D printed and baked snacks. Current Research in Food Science 2026;12:101320. https://doi.org/10.1016/j.crfs.2026.101320.
[132] Gautam AR, Benjakul S, Surasani VKR, Singh A. 3D Food Printing of Surimi Gels: Optimization of Printing Parameters and Textural Properties for Dysphagia-Friendly Applications. Journal of Food Science 2026;91:e71049. https://doi.org/10.1111/1750-3841.71049.

ACCEPTED PAPER

[133] Pan Y, Sun Q, Liu Y, Wei S, Han Z, Zheng O, et al. Investigation on 3D printing of shrimp surimi under different printing parameters and thermal processing conditions. Current Research in Food Science 2024;8:100745. https://doi.org/10.1016/j.crfs.2024.100745.
[134] Santhoshkumar P, Raja V, Priyadarshini SR, Moses JA. Impact of Baking and Steaming of 3D printed Pearl millet - Banana pulp blends on physicochemical and sensory attributes. International Journal of Gastronomy and Food Science 2024;37:100962. https://doi.org/10.1016/j.ijgfs.2024.100962.
[135] Krishnaraj P, Anukiruthika T, Choudhary P, Moses JA, Anandharamakrishnan C. 3D Extrusion Printing and Post-Processing of Fibre-Rich Snack from Indigenous Composite Flour. Food Bioprocess Technol 2019;12:1776–86. https://doi.org/10.1007/s11947-019-02336-5.
[136] Liu Z, Zhang M. Texture properties of microwave post-processed 3D printed potato snack with different ingredients and infill structure. Future Foods 2021;3:100017. https://doi.org/10.1016/j.fufo.2021.100017.
[137] Li X, Cao W, Liu W, Li L, Chen J, Ren G, et al. Effects of microwave freeze drying on the shape fidelity, anti-digestion and physicochemical properties of 3D-printed chlorogenic acid-sweet potato starch. International Journal of Biological Macromolecules 2026;360:151851. https://doi.org/10.1016/j.ijbiomac.2026.151851.
[138] Shen C, Chen W, Li C, Chen X, Cui H, Lin L. 4D printing system stimulated by curcumin/whey protein isolate nanoparticles: A comparative study of sensitive color change and post-processing. Journal of Food Engineering 2023;342:111357. https://doi.org/10.1016/j.jfoodeng.2022.111357.
[139] In J, Im S, Min SC. Cold plasma treatment to improve jelly production using a fused deposition modeling 3D printer. Food Sci Biotechnol 2023;32:39–46. https://doi.org/10.1007/s10068-022-01170-4.
[140] Li R, Wang N, Ma C, Wang J, Wang J, Yang X. Effect and mechanism of ultrasound time and storage time on physicochemical properties, 3D printing accuracy, and microstructure of ovalbumin–gellan gum emulsion gels. Food Chemistry 2025;477:143518. https://doi.org/10.1016/j.foodchem.2025.143518.
[141] Brodkorb A, Egger L, Alminger M, Alvito P, Assunção R, Ballance S, et al. INFOGEST static in vitro simulation of gastrointestinal food digestion. Nat Protoc 2019;14:991–1014. https://doi.org/10.1038/s41596-018-0119-1.
[142] Liu Z, He C, Guo C, Chen F, Bhandari B, Zhang M. Dehydration-triggered shape transformation of 4D printed edible gel structure affected by material property and heating mechanism. Food Hydrocolloids 2021;115:106608. https://doi.org/10.1016/j.foodhyd.2021.106608.
[143] Noree S, Pinyakit Y, Tungkijanansin N, Kulsing C, Hoven VP. Shape transformation of 4D printed edible insects triggered by thermal dehydration. Journal of Food Engineering 2023;358:111666. https://doi.org/10.1016/j.jfoodeng.2023.111666.
[144] He C, Zhang M, Devahastin S. Investigation on Spontaneous Shape Change of 4D Printed Starch-Based Purees from Purple Sweet Potatoes As Induced by Microwave Dehydration. ACS Appl Mater Interfaces 2020;12:37896–905. https://doi.org/10.1021/acsami.0c10899.
[145] Koirala S, Prakash S, Karim A, Bhandari B. 4D shape morphing in 3D-printed pea protein structures through designed surface grooves under drying and frying conditions. Innovative Food Science & Emerging Technologies 2025;100:103924. https://doi.org/10.1016/j.ifset.2025.103924.
[146] Shi Y, Zhang M, Phuhongsung P. Microwave-induced spontaneous deformation of purple potato puree and oleogel in 4D printing. Journal of Food Engineering 2022;313:110757. https://doi.org/10.1016/j.jfoodeng.2021.110757.
[147] Niu D, Zhang M, Mujumdar AS, Li J. Research on Microwave-Induced Bidirectional Deformation of Coix Seed Compound Materials in 4D Printing. Food Bioprocess Technol 2023;16:2400–15. https://doi.org/10.1007/s11947-023-03078-1.

ACCEPTED PAPER

[148] Guo J, Zhang M, Li J, Fang Z. Using Soy Protein Isolate to Improve the Deformation Properties of 4D-Printed Oat Flour Butterfly. Food Bioprocess Technol 2023;16:1165–76. https://doi.org/10.1007/s11947-023-02994-6.
[149] Van Der Sman RGM, Curatolo M, Teresi L. Programmable shape morphing of drying foods via symmetry breaking. Current Research in Food Science 2025;11:101238. https://doi.org/10.1016/j.crfs.2025.101238.
[150] He C, Zhang M, Guo C. 4D printing of mashed potato/purple sweet potato puree with spontaneous color change. Innovative Food Science & Emerging Technologies 2020;59:102250. https://doi.org/10.1016/j.ifset.2019.102250.
[151] Ghazal AF, Zhang M, Bhandari B, Chen H. Investigation on spontaneous 4D changes in color and flavor of healthy 3D printed food materials over time in response to external or internal pH stimulus. Food Research International 2021;142:110215. https://doi.org/10.1016/j.foodres.2021.110215.
[152] Su C, Wu Y, Vardhanabhuti B, Lin M. 4D printing of dysphagia foods using pea protein and purple sweet potato flour. Food Bioscience 2025;64:105887. https://doi.org/10.1016/j.fbio.2025.105887.
[153] Shanthamma S, Preethi R, Moses JA, Anandharamakrishnan C. 4D Printing of Sago Starch with Turmeric Blends: A Study on pH-Triggered Spontaneous Color Transformation. ACS Food Sci Technol 2021;1:669–79. https://doi.org/10.1021/acsfoodscitech.0c00151.
[154] Cen S, Li Z, Guo Z, Li H, Shi J, Huang X, et al. 4D printing of a citrus pectin/β-CD Pickering emulsion: A study on temperature induced color transformation. Additive Manufacturing 2022;56:102925. https://doi.org/10.1016/j.addma.2022.102925.
[155] Ghazal AF, Zhang M, Guo Z. Microwave-induced rapid 4D change in color of 3D printed apple/potato starch gel with red cabbage juice-loaded WPI/GA mixture. Food Research International 2023;172:113138. https://doi.org/10.1016/j.foodres.2023.113138.
[156] Chen X, Zhang M, Tang T, Yu D. The color/shape/flavor of yam gel with double emulsified microcapsules changed synchronously in 4D printing induced by microwave. International Journal of Biological Macromolecules 2024;260:129631. https://doi.org/10.1016/j.ijbiomac.2024.129631.
[157] Zhan J, Fu J, Jin D, Yuan Y, Shen S, Li G, et al. Surimi freshness monitoring of 4D printing material with anthocyanin. Journal of Food Engineering 2023;358:111678. https://doi.org/10.1016/j.jfoodeng.2023.111678.
[158] Li G, Zhan J, Huang J, Xu E, Yuan C, Chen J, et al. Enhanced fresh-keeping capacity of printed surimi by Ca2+-nano starch-lutein and its nondestructive freshness monitoring based on 4D printed anthocyanin. International Journal of Biological Macromolecules 2023;252:126543. https://doi.org/10.1016/j.ijbiomac.2023.126543.
[159] Zhu J, Yang Y, Qiao S, Dai H, Chen H, Fu Y, et al. 4D printing of betanin/gelatin/nano-chitin complexes-functionalized surimi via disulfide bonds, and its applicability in dysphagia diets. Food Hydrocolloids 2024;152:109891. https://doi.org/10.1016/j.foodhyd.2024.109891.
[160] Guo C, Zhang M, Devahastin S. Color/aroma changes of 3D-Printed buckwheat dough with yellow flesh peach as triggered by microwave heating of gelatin-gum Arabic complex coacervates. Food Hydrocolloids 2021;112:106358. https://doi.org/10.1016/j.foodhyd.2020.106358.
[161] Xiao K, Zhang Y, Pan L, Tu K. Study on color and flavor changes of 4D printed white mushroom gel with microcapsules containing gelatin / β-cyclodextrin induced by microwave heating. International Journal of Biological Macromolecules 2024;279:135365. https://doi.org/10.1016/j.ijbiomac.2024.135365.
[162] Chen J, Zhang M, Devahastin S. UV-C irradiation-triggered nutritional change of 4D printed ergosterol-incorporated purple sweet potato pastes: Conversion of ergosterol into vitamin D2. LWT 2021;150:111944. https://doi.org/10.1016/j.lwt.2021.111944.

ACCEPTED PAPER

[163] Chen J, Zhang M, Mujumdar AS, Phuhongsunge P. 4D printing induced by microwave and ultrasound for mushroom mixtures: Efficient conversion of ergosterol into vitamin D2. Food Chemistry 2022;387:132840. https://doi.org/10.1016/j.foodchem.2022.132840.
[164] Chen J, Teng X, Zhang M, Bhandari B, Adhikari B, Yu D. 5D Food Printing with Color Change Induced by Probiotic Growth in a Starch-Protein-Based Gel System. Food Bioprocess Technol 2023;16:2304–14. https://doi.org/10.1007/s11947-023-03064-7.
[165] Hu X, Tang H, Wang J, Zou L, Su X, Xu B. Mycelial growth stimulus-responsive 4D printing: A novel approach for mycelium-based meat analogs fabrication. Innovative Food Science & Emerging Technologies 2026;108:104405. https://doi.org/10.1016/j.ifset.2025.104405.
[166] Guo C, Zhang M, Bhandari B, Devahastin S. Investigation on simultaneous change of deformation, color and aroma of 4D printed starch-based pastes from fruit and vegetable as induced by microwave. Food Research International 2022;157:111214. https://doi.org/10.1016/j.foodres.2022.111214.
[167] Tang T, Zhang M, Mujumdar AS, Teng X. 3D printed white radish/potato gel with microcapsules: Color/flavor change induced by microwave-infrared heating. Food Research International 2022;158:111496. https://doi.org/10.1016/j.foodres.2022.111496.
[168] Huang Y, Zhang M, Pattarapon P, Mujumdar AS. 4D printing of mixed vegetable gel based on deformation and discoloration induced by acidification and dehydration. J Food Process Engineering 2022;45:e14172. https://doi.org/10.1111/jfpe.14172.
[169] Zhao Y, Xiong G, Yang Z, Pan B, Xiao X. Multi-Dimensional Food Printing Technology: Evolution, Applications, and Challenges From 3D to Higher Dimensions. Journal of Food Science 2026;91:e70826. https://doi.org/10.1111/1750-3841.70826.
[170] Lv Y, Wang B, Cheng Y, Lv W, Zeng S, Xiao H. Printing characteristics and microwave infrared-induced 4D printing of chestnut powder composite paste. Journal of Food Engineering 2024;382:112197. https://doi.org/10.1016/j.jfoodeng.2024.112197.
[171] Ma Y, Fu L, He F, Wu D, Lin J, Huang D, et al. Application of AI-Driven Multi-Dimensional Food Printing Technology for Valorization of Food By-Products. J Agric Food Chem 2026;74:4131–50. https://doi.org/10.1021/acs.jafc.5c11224.

ACCEPTED PAPER

Appendix

Nomenclature

Latin symbols	Description
D	Nozzle inner diameter (mm)
h	Layer height (mm)
v_p	Piston velocity (mm s^{-1})
v_{print}	Print speed (mm s^{-1})
Q	Volumetric flow rate (mm^3 s^{-1})
P_{air}	Pneumatic air pressure (MPa)
A_{barrel}	Barrel cross-sectional area (mm^2)
P	Microwave power absorption per unit volume (W m^{-3})
f	Electromagnetic frequency (Hz or GHz)
E	Electric-field strength (V m^{-1})
T_2	LF-NMR transverse relaxation time (ms)
R^2	Coefficient of determination (—)
K	Consistency index ($Pa \cdot s^n$)
n	Power-law flow-behaviour index (—)
G'	Storage modulus (Pa)
G''	Loss modulus (Pa)

Greek symbols	Description
σ	Shear stress (Pa)
τ_y	Yield stress (Pa)
τ_{rec}	Stress-recovery time after nozzle exit (ms–s)
$\dot{\gamma}$	Shear rate (s^{-1})
$\dot{\gamma}_{screw}$	In-barrel screw shear rate (s^{-1})
η	Apparent viscosity (Pa·s)
ε''	Dielectric loss factor (—)
ΔE	Total colour difference (—)
ΔP	Internal vapour-pressure differential (Pa)

Abbreviations	Description
3DFP	Three-Dimensional Food Printing
ABTS	2,2′-azino-bis(3-ethylbenzothiazoline-6-sulfonic acid) radical-scavenging assay
AI/ML	Artificial Intelligence / Machine Learning
ALM	Additive-Layer Manufacturing
AOAC	Association of Official Analytical Chemists
BJ	Binder Jetting

ACCEPTED PAPER

BP-ANN	Back-Propagation Artificial Neural Network
CFD	Computational Fluid Dynamics
CID	Catalytic Infrared Drying
CLS	Cross-Linked Starch
CNN	Convolutional Neural Network
Codex	Codex Alimentarius
DED	Directed Energy Deposition
DHT	Dry Heat Treatment
DNN	Deep Neural Network
DoE	Design of Experiments
EGCG	Epigallocatechin Gallate
FD	Freeze-Drying
FDM	Fused Deposition Modelling
FEA	Finite Element Analysis
FEM	Finite Element Method
GG	Guar Gum
GRAS	Generally Recognized As Safe
HDMP	Heat-Desiccated Milk Powder
HIPPEs	High-Internal-Phase Pickering Emulsions
HIU	High-Intensity Ultrasound
HPMC	Hydroxypropyl Methylcellulose
HPP	High-Pressure Processing
IDDSI	International Dysphagia Diet Standardisation Initiative
IN	Inulin
INFOGEST	International network for in vitro digestion harmonisation
ISO/ASTM	International Organization for Standardization / American Society for Testing and Materials
LBG	Locust Bean Gum
LF-NMR	Low-Field Nuclear Magnetic Resonance
MEX	Material Extrusion
MFD	Microwave Freeze-Drying
MJT	Material Jetting
MTGase	Microbial Transglutaminase
MVD	Microwave Vacuum Drying
MW	Microwave
NIR	Near-Infrared (spectroscopy)
PAT	Process Analytical Technology
PBF	Powder Bed Fusion
PEF	Pulsed Electric Field
PEs	Pickering Emulsions
PLSR	Partial Least-Squares Regression
PPI	Pea Protein Isolate
QC	Quality Control
RF	Radio Frequency
RMSE	Root-Mean-Square Error
SDF	Soybean Dietary Fibre

ACCEPTED PAPER

SDI	Shape-Deviation Index
SFD	Spray–Freeze Drying
SIDF	Soybean Insoluble Dietary Fibre
SPI	Soy Protein Isolate
SSMP	Semi-Skimmed Milk Powder
SVR	Support Vector Regression
TPA	Texture Profile Analysis
UMCH	Ultrasound-assisted Microwave Heating
US	Ultrasound
UV-C	Short-wave Ultraviolet
VPP	Vat Photopolymerisation
WHC	Water-Holding Capacity
WPI	Whey Protein Isolate
XG	Xanthan Gum

ACCEPTED PAPER